

**Topology optimization for dynamic and controlled systems
With application to motion system design**

Delissen, A.A.T.M.

DOI

[10.4233/uuid:c9ed8f61-efe1-4dc8-bb56-e353546cf247](https://doi.org/10.4233/uuid:c9ed8f61-efe1-4dc8-bb56-e353546cf247)

Publication date

2022

Document Version

Final published version

Citation (APA)

Delissen, A. A. T. M. (2022). *Topology optimization for dynamic and controlled systems: With application to motion system design*. [Dissertation (TU Delft), Delft University of Technology]. Delft University of Technology. <https://doi.org/10.4233/uuid:c9ed8f61-efe1-4dc8-bb56-e353546cf247>

Important note

To cite this publication, please use the final published version (if applicable).
Please check the document version above.

Copyright

Other than for strictly personal use, it is not permitted to download, forward or distribute the text or part of it, without the consent of the author(s) and/or copyright holder(s), unless the work is under an open content license such as Creative Commons.

Takedown policy

Please contact us and provide details if you believe this document breaches copyrights.
We will remove access to the work immediately and investigate your claim.

Topology optimization for dynamic and controlled systems

With application to motion system design

Topology optimization for dynamic and controlled systems

With application to motion system design

Proefschrift

ter verkrijging van de graad van doctor
aan de Technische Universiteit Delft,
op gezag van de Rector Magnificus prof. dr. ir. T.H.J.J. van der Hagen,
voorzitter van het College voor Promoties,
in het openbaar te verdedigen
op donderdag 13 oktober 2022 om 15.00 uur

door

Arnoud DELISSEN

Werktuigkundig ingenieur,
Technische Universiteit Delft, Nederland
geboren te Gemert, Nederland.

Dit proefschrift is goedgekeurd door de promotoren.

Samenstelling promotiecommissie bestaat uit:

Rector Magnificus,	voorzitter
Dr. ir. M. Langelaar,	Technische Universiteit Delft, promotor
Prof. dr. ir. A. van Keulen,	Technische Universiteit Delft, promotor

Onafhankelijke leden:

Prof. dr. E.C.N. Silva,	University of São Paulo, Brasil
Prof. dr. G. Schitter,	Technical University Wien, Austria
Prof. dr. ir. T.A.E. Oomen,	Technische Universiteit Eindhoven
Prof. dr. ir. J.W. van Wingerden,	Technische Universiteit Delft
Prof. dr. ir. J.L. Herder,	Technische Universiteit Delft, reservelid

Overig lid:

Prof. dr. ir. M.B. van Gijzen,	Technische Universiteit Delft
--------------------------------	-------------------------------



Keywords: Topology optimization, Structural dynamics, Motion control

Printed by: Gildeprint

Cover: Arnoud Delissen

Copyright © 2022 by A.A.T.M. Delissen

ISBN 978-94-6384-367-6

An electronic version of this dissertation is available at
<http://repository.tudelft.nl/>

Contents

Summary	vii
Samenvatting	ix
1 Introduction	1
1.1 Motion control	1
1.2 Dynamics	2
1.3 Topology optimization	3
1.4 Challenges	5
1.5 Scope	6
1.6 Outline.	6
2 Large-scale eigenfrequency optimization	9
2.1 Introduction	10
2.2 Case description and methods	12
2.3 Demonstrator and experimental validation.	26
2.4 Discussion	31
2.5 Conclusion.	32
3 Limitation of resonances	35
3.1 Introduction	36
3.2 Methods	39
3.3 Results	47
3.4 Conclusions	60
4 Integrated optimization in the Nyquist domain	61
4.1 Introduction	62
4.2 Local approximation of the Nyquist curve	67
4.3 Application to controller-structure optimization	72
4.4 Modeling.	75
4.5 Results	79
4.6 Discussion	88
4.7 Conclusion.	88
5 Large-scale integrated optimization for MIMO	91
5.1 Introduction	92
5.2 Approximation of the H_∞ -norm	96
5.3 Modeling.	100
5.4 Approximation of eigenmode design sensitivities	104
5.5 Numerical examples	108
5.6 Discussion	121

5.7	Conclusion	122
6	Conclusions	125
6.1	Manufacturing considerations	125
6.2	Computational effort	126
6.3	Integrated controller-structure optimization	127
6.4	Recommendations	128
A	Appendix	129
A.1	Robust formulation for eigenfrequencies	129
A.2	Circle in the complex domain	130
	Bibliography	131
	Acknowledgments	141
	Curriculum Vitæ	143
	List of Publications	145

Summary

High-precision motion systems are crucial for many applications, such as in semiconductor equipment, microscopy, robotics, and medical devices. Next to high operating speeds, high accuracy and precision are required, which makes the design of these systems a challenging task. Dynamics, feedback control, and their interaction all play an important role in the design and its final performance.

This dissertation shows that topology optimization in combination with additive manufacturing offers new opportunities for the automated design of motion systems with unprecedented performance. The main challenges addressed are the manufacturability of the designs, the computational time required for full-scale topology optimization, and the effective formulation of integrated controller-structure optimization problems for improvement of the closed-loop system performance.

First of all, a systematic optimization setup is presented in Chapter 2 to obtain directly producible optimized designs, while initially focusing on structural eigenfrequency maximization. It includes all subsequent manufacturing steps, such as additive manufacturing, milling, and assembly of components. A full-scale optimized design has been produced and its performance has been validated experimentally.

Although significant eigenfrequency gains can be obtained through optimization, this does not directly mean that the integrated system performance is good, as the resonance amplitudes are also very important to consider. Therefore, a new method for topology optimization is proposed in Chapter 3, which enables limitation of resonance amplitudes in the frequency domain. Additionally, design sensitivities are calculated efficiently by approximation with reduced-order models.

Next, a PID controller is included for a truly integrated SISO controller-structure optimization in Chapter 4. The Nyquist curve includes both phase and amplitude information. By its local approximation using circles, topology optimization can be performed in an efficient and stable manner. Only using a limited number of constraints have to be used to influence the global shape of the Nyquist curve in the complex domain. This allows topology optimization to maximize bandwidth while ensuring closed-loop stability and robustness against disturbances, based on the modulus margin.

Finally, the method is extended to MIMO systems in Chapter 5. The local approximations are used to approximate the complex closed-loop sensitivity function, which quantify the disturbance rejection of the system. To ensure robustness against simultaneous disturbances on multiple channels, the \mathcal{H}_∞ norm is approximated and limited during optimization. This ensures differentiability and prevents the need for additional constraints for the different inputs and outputs. Furthermore, significant computational gain is achieved by approximation of the computationally expensive design sensitivities for the eigenmodes, enabling optimization of full-scale 3D systems. Combining all these techniques, this dissertation demonstrates that it is possible to perform integrated controller-structure topology optimization of motion systems of industry-relevant complexity.

Samenvatting

Positioneringssystemen met hoge precisie zijn cruciaal voor veel toepassingen, zoals in halfgeleiderapparatuur, microscopie, robotica en medische apparaten. Naast hoge werksnelheden zijn een hoge nauwkeurigheid en precisie vereist, wat het ontwerp van deze systemen uitdagend maakt. Dynamica, terugkoppelingsregeling en hun interactie spelen een belangrijke rol in het ontwerp en de uiteindelijke prestaties ervan.

Dit proefschrift laat zien dat topologie optimalisatie in combinatie met additieve fabricage nieuwe mogelijkheden biedt voor het automatisch ontwerpen van positioneringssystemen met ongekende prestaties. Hier zijn de belangrijkste uitdagingen de maakbaarheid van de ontwerpen, de rekentijd die benodigd is voor de topologie optimalisatie en het formuleren van geïntegreerde optimalisatieproblemen met zowel regelaar als structuur.

Allereerst wordt in Hoofdstuk 2 een systematische optimalisatie-opzet gepresenteerd om geoptimaliseerde ontwerpen te verkrijgen die direct maakbaar zijn. Hierbij wordt in eerste instantie gefocust op maximalisatie van structurele eigenfrequenties. De opzet omvat alle opeenvolgende productiestappen, zoals 3D printen, frezen en assemblage van componenten. Een geoptimaliseerd ontwerp is geproduceerd op volledige schaal en de prestaties hiervan zijn experimenteel gevalideerd.

Hoewel door optimalisatie aanzienlijk hogere eigenfrequenties kunnen worden bereikt, betekent dit niet direct dat ook de geïntegreerde systeemprestaties goed zijn, omdat de resonantie-amplitudes ook erg belangrijk zijn om te beschouwen. Daarom wordt in Hoofdstuk 3 een nieuwe methode voorgesteld die beperking van resonantie-amplitudes in het frequentiedomein mogelijk maakt. Daarnaast worden de ontwerpgevoeligheden efficiënt berekend door benadering met gereduceerde-orde modellen.

Vervolgens wordt een PID-regelaar toegevoegd voor een geïntegreerde SISO optimalisatie met regelaar en structuur in Hoofdstuk 4. Door de Nyquist curve lokaal te benaderen met behulp van cirkels kan de topologie optimalisatie op een efficiënte en stabiele manier worden uitgevoerd. Een beperkt aantal restrictie-functies kan worden gebruikt om de globale vorm van de Nyquist curve te beïnvloeden in het complexe domein. Op basis van de modulus marge maakt dit het mogelijk om de bandbreedte te maximaliseren waarbij de gesloten-lus stabiliteit en de robuustheid tegen verstoringen worden gewaarborgd.

Tenslotte wordt de methode uitgebreid naar MIMO systemen in Hoofdstuk 5. De lokale cirkel benaderingen worden gebruikt om de complexe gesloten-lus gevoeligheidsfunctie te benaderen, die de verstoringsonderdrukking van het systeem kwantificeert. Om de robuustheid tegen gelijktijdige verstoringen op meerdere kanalen te garanderen, wordt de \mathcal{H}_∞ -norm benaderd en gelimiteerd tijdens optimalisatie. Dit zorgt voor differentieërbaarheid en voorkomt extra restrictie-functies voor de verschillende in- en uitgangen. Verder wordt een aanzienlijke rekenwinst behaald door de ontwerpgevoeligheden van de eigenmodi te benaderen. Door al deze technieken te combineren demonstreert dit proefschrift dat het mogelijk is om geïntegreerde topologie optimalisatie met structuur en regelaar uit te voeren voor positioneringssystemen met industrie-relevante complexiteit.

1

Introduction

Modern society heavily depends on electronic chips, which can be found in virtually any device. These chips contain billions of transistors, made out of tiny structures on a nanometer scale. Their production is a complex process involving many steps, where multiple layers containing patterns are overlaid on top of each other. Using lithography, the desired pattern for each layer is transferred to the chip using a source of light and a mask partially blocking the light. For a fully functioning chip, each new layer needs to be positioned at exactly the correct position with respect to the previous. Additionally, this needs to happen at extreme speeds and accelerations to achieve a high throughput and keep production costs low. The precise positioning is done using a *motion stage*, on top of which the chips are placed (Martinez and Edgar, 2006). Next to semiconductor equipment, other applications also require high-performance motion stages for precise positioning. For instance, samples under a (scanning probe) microscope require precise positioning for accurate measurements and fast scanning for a quick analysis (Abramovitch *et al.*, 2007). The main challenge is to increase the speed at which the motion stage operates, without sacrificing accuracy.

1.1 Motion control

High precision in a motion system is achieved by feedback control, as is illustrated in Fig. 1.1. Motions of the stage are detected by sensors, *e.g.*, using laser interferometry. The difference between the measurement and the desired reference position is then fed into the controller, *e.g.*, a proportional-integral-derivative (PID) controller. Based on the error, the controller determines a correction action, which is applied as a force on the stage, *e.g.*, using electro-magnetic actuators. This loop is continuously repeated at real-time during operation to ensure accurate positioning (Åström and Murray, 2008).

In reality, the motion stage does not move like a rigid body. Especially when high speeds and accelerations are involved, dynamic loads will deform the stage, as illustrated in Fig. 1.2. The sensor thus not only measures the position of a stage, but also its dynamic deformations. The nature of the system dynamics limits the maximum *bandwidth* of the motion stage: this is the frequency up to which errors can effectively be corrected by the feedback loop. A system with a higher bandwidth is able to move faster. However, if

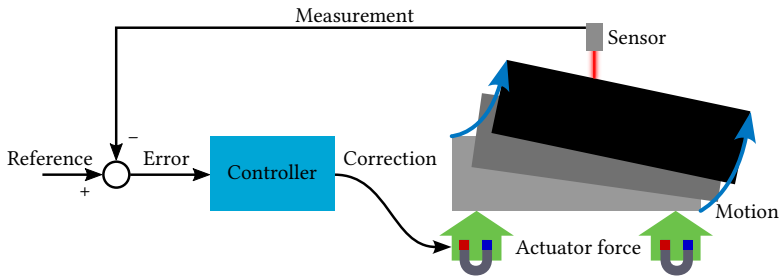


Figure 1.1: Schematic overview of a simple feedback loop for motion control.

the controller bandwidth is tuned too high with respect to the system dynamics, it becomes increasingly sensitive to *disturbances*. Disturbances can be caused by, for instance, measurement noise, vibrations from the environment, or imperfections in the system. In extreme cases, bad controller tuning may even lead to *instability*, where measurement and reference signal amplify each other, resulting in a positive feedback loop. This makes both the dynamics of the stage and the controller integral parts of the design of a motion system, as studied in the discipline of *mechatronics* (Munnig Schmidt *et al.*, 2011). Their interaction makes the design of a motion system difficult, especially for multi-input multi-output (MIMO) systems, where different control loops interact together (Skogestad and Postlethwaite, 2001).

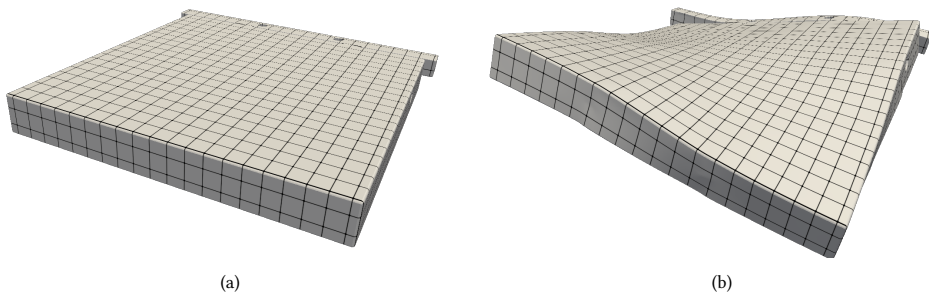


Figure 1.2: a) An undeformed motion stage for which accuracy is required on the top. b) A stage which is deformed due to dynamic excitation (deformation amplified for illustration).

1.2 Dynamics

The dynamics of a motion system can be analyzed in the frequency domain. This is favored over analysis in the time domain, as it allows for straight-forward quantification of performance and disturbance rejection characteristics in a motion system. The dynamic behavior is described using *eigenmodes* (Fig. 1.3) and corresponding *eigenfrequencies* at which they occur (Rayleigh, 1945). For a force exciting the structure at a certain frequency, the dynamic deformation is a combination of all eigenmodes of the system. However, calculating all eigenmodes requires a prohibitive amount of computational time. Therefore, usually

a limited number of eigenmodes is used to model the system dynamics (e.g., Geradin and Rixen, 2015).

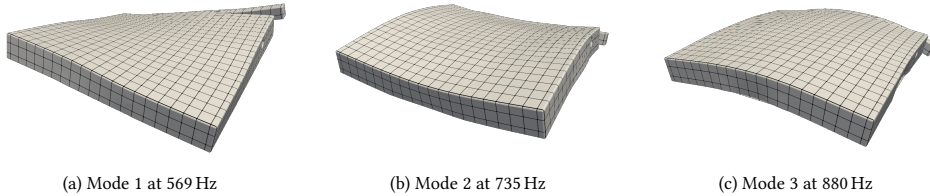


Figure 1.3: The first three flexible eigenmodes of a motion stage.

A frequency response diagram shows the ratio between the amplitude of input force and measured displacement as a function of frequency, as is illustrated in Fig. 1.4. Around the eigenfrequencies, resonance occurs due to the flexible eigenmodes of the structure. The interaction with a controller depends on the eigenmodes associated with these resonances and their corresponding frequencies. By altering the design, the eigenmodes and eigenfrequencies change, which may lead to better system performance (Munnig Schmidt *et al.*, 2011). The main challenge here is *how* to change them. For instance, increasing the eigenfrequencies may lead to a higher bandwidth, as the flexible dynamics only start at a higher frequency. However, increasing eigenfrequencies may also affect the eigenmodes, which may counteract the anticipated effect. Next to this, it is very difficult to predict by intuition how the dynamics will change when designing a structure. This is where (topology) optimization techniques can aid the engineer responsible for the design of a controlled structure.

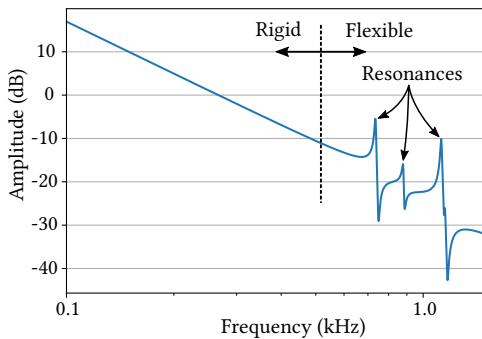


Figure 1.4: The frequency response function shows the measured amplitude for an harmonic unit load on the actuators. As the frequency increases, it generally becomes more difficult to move the mass. Resonances occur around the eigenfrequencies, which are caused by flexible deformations of the structure.

1.3 Topology optimization

Optimization techniques are used to systematically find an optimized structure with improved performance, for instance, optimized for maximum stiffness with a given amount of material. This can be done by changing dimensions in a structure, by changing its shape, or in addition by also changing its topology (Christensen and Klarbring, 2009), as seen in Fig. 1.5. *Topology optimization* provides the ultimate freedom in terms of geometry, with

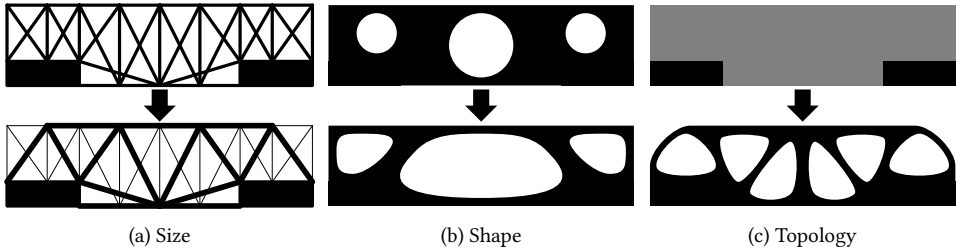


Figure 1.5: The three different types of structural optimization. a) In size optimization, only the dimensions of the members can be changed. b) For shape optimization the shape of the structure can be changed but not the amount of holes. c) Topology optimization offers maximum design freedom by allowing new structures to form.

the potential of achieving better performance (Bendsøe and Sigmund, 2003). Here, we focus on density-based topology optimization, which is the most developed method and provides a wide array of manufacturability filters (e.g. overhang filter for additive manufacturing). The entire design domain is divided into small elements and by continuously scaling their material fractions between 0 and 1, elements can become solid (1) or void (0). An *optimization algorithm* is then used to gradually change all the material fractions step by step, until a final design with optimal performance is obtained (Papalambros and Wilde, 2000).

An important ingredient for efficient topology optimization is the calculation of *design sensitivities*. These provide information on how changing the material fractions affects the performance of the design. The optimization algorithm uses design sensitivities to determine which design changes are most effective. Therefore, the number of design iterations can be small, reducing the total computational time required.

Many different metrics can be used to characterize performance, which leads to a large selection of possibilities for optimization. As mentioned, the stiffness can be improved (Bendsøe and Kikuchi, 1988), but also dynamic measures, such as eigenfrequencies can be maximized (Ma et al., 1995), or the dynamic response over a range of frequencies (Ma et al., 1993). An example of a 3D motion stage optimized for maximum eigenfrequencies can be seen in Fig. 1.6.

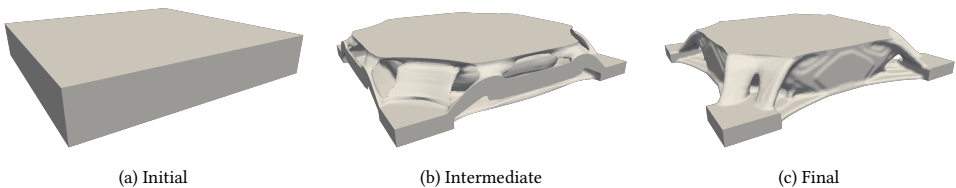


Figure 1.6: Example of a 3D topology optimization for maximum eigenfrequencies, showing the design evolution.

Specifically for motion control, the controller can be designed such that it accommodates the dynamics of the system, or *vice versa* the dynamics of the system can be adapted such that it shows favorable characteristics for control. In this dissertation, an approach is explored in which the controller and the structure are optimized *simultaneously*, using

topology optimization.

A good starting point is provided by the work of [Van der Veen et al. \(2015, 2017\)](#), who optimized for maximum bandwidth of a motion stage, subject to constraints on disturbance rejection properties and closed-loop stability. However, significant challenges remain before these methods can be applied to the practical design of a motion stage.

1.4 Challenges

For the current dissertation, three main challenges can be identified that prevent application of topology optimization to the design of realistic motion systems.

I. Manufacturing considerations and validation

Already since the mid 90's, topology optimization has been applied to improve dynamic properties, such as the maximization of eigenfrequencies ([Ma et al., 1995](#)). With the emergence of additive manufacturing during the same period, it has become possible to also produce the intricate designs obtained from topology optimization. As with any manufacturing method, additive manufacturing comes with its own set of constraints on the design, some of which have been successfully incorporated in topology optimization ([Gaynor and Guest, 2014](#); [Langelaar, 2016](#); [Van de Ven et al., 2020b](#)). However, for a realistic design, multiple additional manufacturing steps need to be incorporated, such as milling and assembly of different components (for instance, magnetic actuators). The integration of the full manufacturing sequence into the optimization presents new challenges that have not been researched extensively in the context of motion systems. Also, topology optimized designs for dynamics have been analyzed numerically, but their experimental validation has not yet been reported in literature, especially for systems of industry-relevant complexity.

II. Computational effort

A fine design resolution enables a large geometric freedom, but comes at the price of a high computational effort. Large scale 3D topology optimization has been demonstrated for maximization of stiffness, by exploiting parallelization and cluster computing ([Aage et al., 2017](#)). However, optimization of dynamic systems is significantly more challenging in terms of computational time. During optimization, many eigenmodes are required to describe the dynamics of a motion system, which can easily cost over an order of magnitude more computation time than a static analysis (e.g., [Geradin and Rixen, 2015](#)). Next to this, design sensitivities of the eigenmodes have to be calculated, which adds another significant amount of computation time ([Lee, 1999](#); [Van der Veen et al., 2017](#)). This presently prevents efficient topology optimization of motion systems in 3D with a fine resolution.

III. Application to 3D and MIMO

Besides significant computation time, 3D structures are characterized with more eigenmodes in the same frequency range compared to 2D structures. This increases the complexity of integrated controller-structure optimization, preventing successful optimization in 3D according to preliminary studies following the work of [Van der Veen et al. \(2017\)](#). Additionally, a magnetically levitated stage is considered as a central carrier problem in

this dissertation, which needs to be controlled in six degrees of freedom. For this MIMO system, additional attention is required to prevent disturbances of one control loop affecting the other control loops (Skogestad and Postlethwaite, 2001).

Given the challenges outlined above, the ultimate aim of this dissertation is therefore:

Enabling the large-scale 3D and MIMO integrated controller and structure topology optimization for motion system design.

1.5 Scope

The topology optimization methods used in this dissertation are based on the density method (Bendsøe and Sigmund, 2003), which is the most developed and offers many different manufacturability filters. The topology methods used are ideally kept as standard as possible. The structural dynamics are assumed to be linear, with only weak damping (e.g. hysteretic, Rayleigh, or modal damping), as the intended systems are made out of metal with only few other metal parts rigidly connected.

The focus of this dissertation is on the combination of topology optimization, manufacturability, and controller tuning, and not on the synthesis of state-of-the-art controllers. Therefore, only basic PID controllers are used. Furthermore, no time delay is included and the systems are assumed to be linear time-invariant (LTI). The controllers are used for the control of one or more rigid body modes, as is the case for a magnetically levitated stage.

The intended production process for the designs is additive manufacturing by laser powder-bed fusion. In the optimization, only geometric design rules are incorporated (e.g., feature size, overhang) without considering other (thermo)mechanical phenomena related to the printing process .

1.6 Outline

This dissertation content is based on multiple papers. Therefore, each chapter can mostly be read independently of each other, with exception of Chapter 5, which is in many aspects an extension on Chapter 4. Due to the paper-based content, the mathematical notations in each chapter might differ slightly, and some repetition is inevitable. The papers are incorporated as-is, with only changes in layout, mathematical notation, and omission of several appendices. The main contents of each chapter are as follows:

Chapter 2 The focus of this chapter is on Challenge I: the optimization process of a motion stage with emphasis to the entire manufacturing sequence, including additive manufacturing, milling, and the assembly of actuators. For the additive manufacturing limitations, an improved overhang filter is presented with enhanced flexibility in tuning the maximum overhang angle and print direction. Further considerations for large-scale 3D maximization of eigenfrequencies are presented and an efficient method of ensuring a minimum length-scale is introduced. Finally, a demonstrator is realized based on the optimized design, which is also experimentally verified.

Chapter 3 Next, the topology optimization of frequency response functions is explored. A method is presented that enables frequency-dependent constraints on maximum

resonance amplitudes. With regard to Challenge II, in order to keep the computation time low, different kinds of reduced-order models are compared with the explicit solution of the full model. An additional gain in computational effort may be attained by approximation of the design sensitivities. It is found that depending on the choice of reduced-order model, the approximated design sensitivities improve in accuracy.

Chapter 4 Moving towards the integrated controller-structure optimization of a single-input single-output (SISO) motion system, this chapter explores optimization using the Nyquist curve. In the Nyquist curve of the open-loop system, mechanical resonances result in characteristic circles. Using local analytical descriptions of these circles, geometrical constraints can be imposed in the complex domain. These constraints can be used to influence and restrict the global shape of the Nyquist curve, for instance, to simultaneously enforce closed-loop stability and ensure sufficient modulus margin. Additionally, an efficient robust formulation is presented for topology optimization of dynamic problems. This enables control on minimum length-scale in the design without additional computational effort.

Chapter 5 Finally, to address Challenge III, the method is extended to MIMO systems by local approximation of the \mathcal{H}_∞ norm corresponding to the sensitivity function. Based on local circle approximations of the sensitivity function in the complex domain, upper bounds can be imposed on the peak values of its singular values. By using an adaptive correction scheme and imposing constraints on each local approximation, a maximum limit can effectively be imposed on the \mathcal{H}_∞ norm. This enables efficient optimization including the disturbance rejection properties for MIMO systems, involving the effect of combined disturbances on the multiple control loops. Furthermore, design sensitivities of the eigenmodes are approximated with a new method that significantly reduces computation time, while keeping sufficiently accurate sensitivities. This corresponding computational gain enables the integrated controller-structure topology optimization of 3D and MIMO structures, which is demonstrated using numerical examples.

Chapter 6 concludes this dissertation with the main findings, as well as several suggestions for future research.

2

Large-scale eigenfrequency optimization

The design of high-precision motion stages, which must exhibit high dynamic performance, is a challenging task. Manual design is difficult, time-consuming, and leads to sub-optimal designs that fail to fully exploit the extended geometric freedom that additive manufacturing offers. By using topology optimization and incorporating all manufacturing steps (printing, milling, and assembly) into the optimization formulation, high-quality optimized and manufacturable designs can be obtained in an automated manner. With a special focus on overhang control, minimum feature size, and computational effort, the proposed methodology is demonstrated using a case study of an industrial motion stage, optimized for maximum eigenfrequencies. For this case study, an optimized design can be obtained in a single day, showing a substantial performance increase of around 15% as compared to a conventional design. The generated design is manufactured using laser powder-bed fusion in aluminium and experimentally validated within 1% of the simulated performance. This shows that the combination of additive manufacturing and topology optimization can enable significant gains in the high-tech industry.

2.1 Introduction

The combination of additive manufacturing (AM) and topology optimization has long been promised as a perfect marriage. However, the step from theory to practice has been mostly limited to components intended for use as static structures (see, e.g., Yoder *et al.*, 2018; Lynch *et al.*, 2018). In more demanding applications, such as semiconductor equipment, robotics, microscopy, medical devices, and micro-electromechanical devices, extreme dynamic performance is usually required (Munnig Schmidt *et al.*, 2011; Oomen, 2018). Studies on the combination of AM and topology optimization with realistic complexity for these high-tech applications are scarce, which is surprising, since especially in such applications the potential of this combination is expected to be significant.

The high-tech industry relies on motion systems, e.g. for high-precision positioning of samples in microscopy and of wafers and components in the semiconductor industry (Munnig Schmidt *et al.*, 2011). Better and better performance is demanded for future targets, and the time-to-market is crucial in this field (Oomen, 2018). Manual design of motion systems is a time-intensive process, where a design is iterated between mechanical designers, dynamics engineers, manufacturing experts, and control specialists. The eigenfrequencies of the system are often limiting the performance (*i.e.* bandwidth) and a higher bandwidth can generally be obtained by increasing the eigenfrequencies (Van der Veen *et al.*, 2017).

With metal AM technology maturing, a vastly increased range of geometries can be manufactured as compared to traditional machining processes, enabling potential for enhanced performance. However, it also further complicates the design process for engineers aiming to fully exploit this potential in terms of performance.

The potential of AM can be systematically exploited by using topology optimization, where an optimized design is generated in an automated manner (Bendsøe and Sigmund, 2003). Much literature is already available on how to incorporate the remaining limitations of AM into the optimization (see, e.g., Gaynor and Guest, 2014; Langelaar, 2016; Hoffarth *et al.*, 2017; Qian, 2017; Liu *et al.*, 2018; Van de Ven *et al.*, 2020b). However, little experimental data and industrial applications can be found beyond simple monolithic brackets based on the maximization of stiffness (see, e.g., Yoder *et al.*, 2018; Lynch *et al.*, 2018). For complex applications in the high-tech industry, the usage of topology optimization is not straightforward. The performance of dynamic systems also depends on the mass distribution next to its stiffness. Despite many theoretical examples of dynamical (*i.e.* eigenfrequency) optimizations (Ma *et al.*, 1995; Pedersen, 2000; Zargham *et al.*, 2016), the gap towards practical implementation is still significant, particularly in the context of high-precision motion systems produced with metal additive manufacturing. Here, three main challenges are identified, which apply to many complex design applications in the high-tech domain and beyond. The challenges include various aspects of manufacturability, design resolution (*i.e.* computational cost), and assessment of performance by experimental validation.

Manufacturing A manufacturing process usually requires a multi-step sequence, which does not only involve AM (laser powder-bed fusion), but also milling to obtain the necessary surface finish and accuracy. Additionally, different components are assembled together to form a system. As each component affects the stiffness and mass distribution, it is critical to evaluate the performance of the entire assembled system. While only the

performance of the complete system is evaluated, all preceding manufacturing steps must be represented in the optimization process in order to arrive at a realizable design. First of all, the AM process imposes an overhang angle restriction everywhere in the structure. Secondly, small and fragile features need to be prevented to avoid local overheating and/or warping during manufacturing. Thirdly, the support structures required for the AM process can be removed by milling after printing, but the amount of support structures needs to be minimized as well in order to limit build time and material use. Next to that, sufficient material is required to attach components at interface locations, for instance with bolts. It is essential to incorporate these practical considerations in the optimization, otherwise accounting for them through modifications afterward will inevitably degrade the performance of the obtained design. Additionally, these modifications may be tedious to apply and would needlessly require additional design time.

Design resolution A higher design resolution in topology optimization corresponds to more freedom in representing geometric features. AM provides a very high spatial resolution, which ideally should correspond to the design resolution of topology optimization. However, having a fine design resolution inflicts a large computational burden, especially since eigenfrequency computations are involved, which easily takes up to an order of magnitude more computation time compared to calculations required for static structures. Additionally, minimum feature size control in topology optimization (through the robust formulation (Wang *et al.*, 2011)) requires the solution to three different eigenvalue problems in each design iteration, further increasing the computational cost by a factor of three. Ideally, a design with fine resolution can be obtained in a matter of hours.

Validation Lastly, by actually building and testing a demonstrator, the performance of the optimized structure is assessed in reality. This is the ultimate test to see if all practical issues are correctly accounted for and if the optimized performance is as expected.

In this work, we aim to incorporate all aforementioned steps using an industrial case of relevant complexity, from optimization to experimental validation. The main novel contribution is the combination of different aspects required to arrive at a physical industry-relevant product using topology optimization and AM and demonstration of its promised potential. Sub-contributions include 1) the representation of the entire (multi-step) manufacturing process into the optimization in a structured manner, 2) a simple extension of an existing overhang filter (Langelaar, 2016), significantly improving its geometric accuracy and enabling the use of overhang angles and print directions not aligned with the finite element grid, 3) a novel efficient approach to the robust formulation for eigenfrequency maximization problems (Wang *et al.*, 2011), reducing the computational cost by a factor three, and 4) experimental validation of an optimized design for a high-tech case study.

This chapter is organized as follows. First, in Section 2.2, the industrial design case is introduced, which is used as a demonstration for the challenges and optimization process. All aspects of the multi-step manufacturing process are captured into the optimization formulation, and each manufacturing step is explained in detail. In Section 2.3, an optimized design is obtained for the case study using the proposed methodology. Its performance is numerically compared with several reference designs and also experimentally validated. Section 2.4 provides a discussion on the possibilities and limitations of the current work. Finally, concluding remarks can be found in Section 2.5.

2.2 Case description and methods

2.2.1 Chuck optimization case

To help illustrate the challenges and methodology, the design case of a high-precision motion stage is introduced (Fig. 2.1a). This concept can be used, for instance, for the precise positioning of microchips during their production or for their inspection under a microscope. For this application, a high level of precision and repeatability is required as chips consist of many stacked layers with nanometer-sized features and their correct functioning critically depends on connections between the layers. Additionally, this setup is suited for operation in a vacuum environment (Laro *et al.*, 2013). A long-stroke stage first provides an extended range of motion with coarse precision. On top of the long-stroke stage, a short-stroke chuck (Fig. 2.1b) is magnetically levitated and its position is actively controlled by a feedback system to provide the required accuracy. This makes the short-stroke chuck the most important component from a system point of view. By designing a chuck with high eigenfrequencies, a high bandwidth can be achieved, which results in higher operating speeds and better accuracy (Van der Veen *et al.*, 2017). The goal is therefore to maximize the eigenfrequencies of the short-stroke chuck using topology optimization.

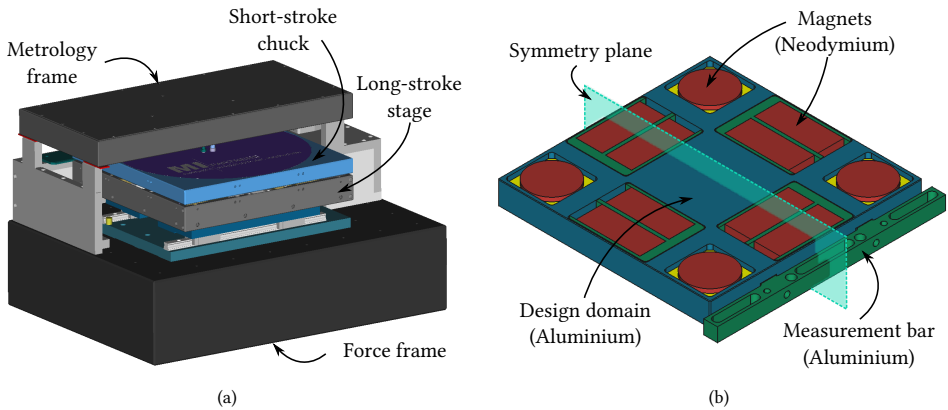


Figure 2.1: CAD geometry of the motion stage. a) Model of the entire stage setup, with the chuck indicated in blue. b) Bottom view of the chuck showing the design domain for the topology optimization (blue) and required components. The blue and green components are made of aluminium, the yellow of stainless steel, and the red parts are neodymium magnets.

Eight sets of permanent magnets are mounted on the chuck (Fig. 2.1b) and are used for position control in 6 degrees of freedom. The positions of all components are given *a priori* and therefore cannot be changed during the optimization. Two pairs of rectangular magnets are used for in-plane actuation and the four circular magnets are used for out-of-plane actuation and gravity compensation (Laro *et al.*, 2013). These are specifically tuned to support a total chuck mass of 18.5 kg. Since 11 kg is used for the magnets (neodymium) and their mounts (stainless steel and aluminium), the remaining 7.5 kg is available for an optimized aluminium frame (AlSi10Mg) produced by the AM process of laser powder-bed fusion.

The outer dimensions of the design domain (excluding components) are $400 \times 400 \times 48$ mm. This both fits in the build-chamber of the MetalFAB1 system of Additive Industries (Additive Industries, 2021) which is used for fabrication, and meets the mass requirement when using 50% of the maximum available volume (*i.e.* volume fraction). To provide sufficient geometric freedom for the optimization, $1 \times 1 \times 1$ mm cubes are used for the parametrization of the design as well as its analysis. The entire chuck including the external components is meshed into a grid of $427 \times 430 \times 49$ elements. Each of these elements has a continuous design-density between 0 (void) and 1 (solid), defined in the design field \mathbf{x} . Although the printing process provides a higher resolution than 1 mm, this resolution already results in a formidable computational challenge, as will be discussed in Section 2.2.2.

Optimization problem For the goal of maximizing a number of eigenfrequencies, effective optimization formulations exist (see, *e.g.* Ma *et al.*, 1995; Zargham *et al.*, 2016). Following the formulation of Ma *et al.* (1995), objective and constraints are adapted to the problem at hand as

$$\begin{aligned} \min_{\mathbf{x}} \quad & \sum_{i=1}^3 \frac{1}{\Omega_i^2} + g_{\text{supp}}, \\ \text{s.t.} \quad & V \leq V_{\text{lim}}, \\ & g_{\text{sol}} \leq 0, \\ & 0 \leq \mathbf{x} \leq 1. \end{aligned} \tag{2.1}$$

By minimizing the reciprocals of the lowest three eigenfrequencies Ω_i , the individual eigenfrequencies are maximized, with focus on the lowest one. An additional penalty g_{supp} is added to minimize the use of support structures that are removed by milling (Section 2.2.2). This ensures that support material is only added when it is beneficial for higher eigenfrequencies. The design volume V is limited to a maximum of V_{lim} , in order to satisfy the mass requirement. Another constraint g_{sol} is added to enforce sufficient solid material at component interfaces (Section 2.2.2). During optimization, the challenge is to find those design parameters \mathbf{x} which result in a minimal objective, while satisfying all constraints.

Optimization process The objective and constraint values need to be evaluated for each design iteration. These depend on the design field \mathbf{x} , but to ensure a manufacturable design, the design field is passed through a sequence of filters before the calculation of the eigenfrequencies. Each filter accounts for a different aspect towards manufacturability by transforming the design variables, such as enforcing a minimum feature size, removing overhanging features, removing material in milling, or adding the components. A graphical overview of the full filtering and analysis structure can be found in Fig. 2.2. The series of filters can be seen as a composition of mathematical operators, which transform the initial design field \mathbf{x} and eventually results in the quantities required for the optimization problem in Eq. 2.1. All operations in the graph are evaluated from start to end during each design iteration. The individual operations are explained in more detail in Section 2.2.2.

The design sensitivities (*i.e.* gradients) of the objective and constraints are also calculated during each design iteration, which is required for an effective optimization. The derivations of sensitivities are not discussed in this manuscript, as for all operations they can either trivially be derived, or they can be found in corresponding literature (Brunns and Tortorelli, 2001; Wang *et al.*, 2011; Langelaar, 2016; Ma *et al.*, 1995). Once the design

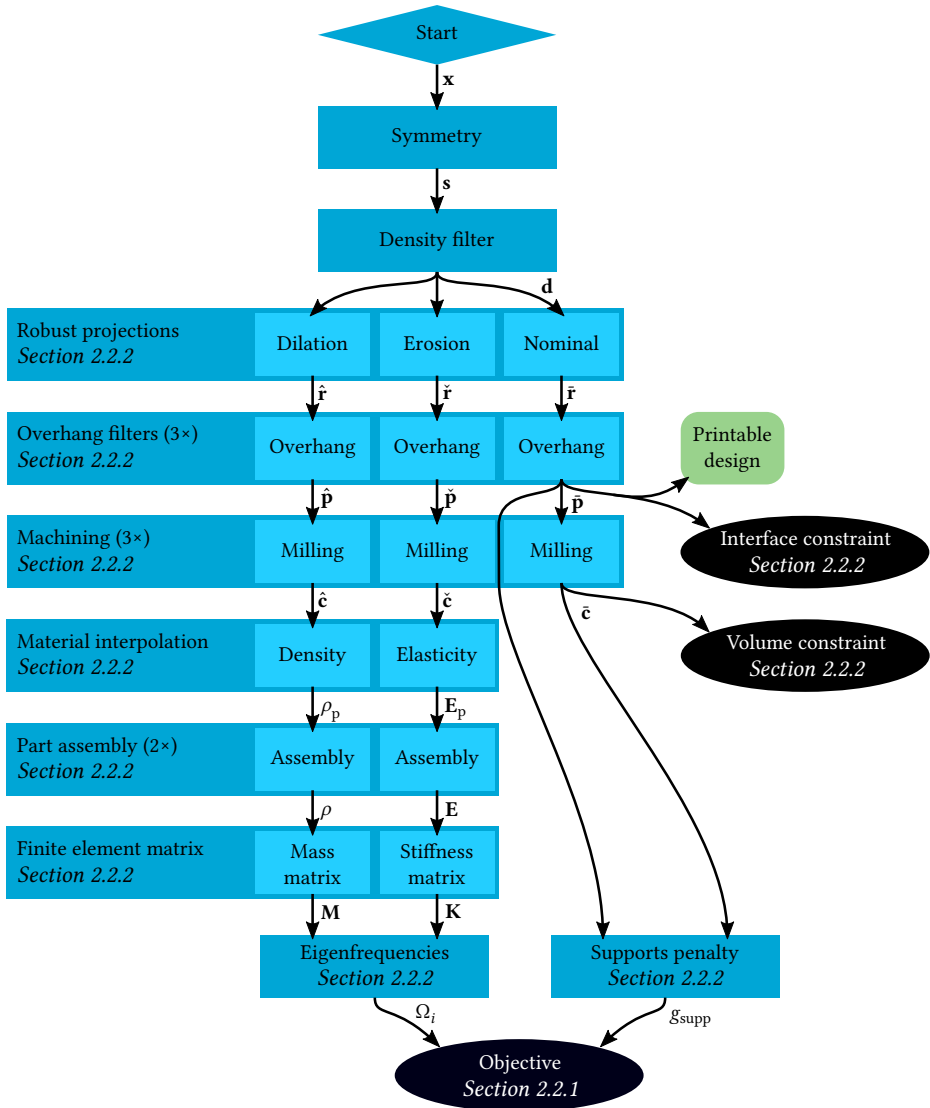


Figure 2.2: Graphical overview of the optimization formulation (Eq. 2.1). The design variable x are passed through a sequence of filters and mathematical operations (the blue blocks) in order to obtain the objective and constraint values (in black) corresponding to a manufacturable design. The entire sequence of operations is executed in each design iteration, where the optimizer repeatedly determines the new design x . The design used for actual printing in green. The individual operations are explained in detail in corresponding sections.

sensitivities are available, the design parameters \mathbf{x} are updated towards an optimal design, using the method of moving asymptotes (MMA) (Svanberg, 1987), and the process is repeated until the design stabilizes. Typically 50-150 design iterations are required for an eigenfrequency optimization, depending on the complexity of the optimization formulation.

2.2.2 Methods

This subsection describes the specific methods involved in the chuck topology optimization scheme outlined in Fig. 2.2. The large-scale computational process to evaluate the eigenfrequencies is also discussed.

Symmetry Starting with the first step in the scheme of Fig. 2.2, which is to convert the design field \mathbf{x} into a symmetric design \mathbf{s} . Although a symmetric design is not strictly required, it is preferred to keep the center of gravity close to the midpoint of the chuck, which in this case gives reason to enforce symmetry. Symmetry can be achieved by reflecting the design over the chosen plane of symmetry and calculating the average of the original and the mirrored design as

$$\mathbf{s} = \frac{\mathbf{x} + \mathbf{x}_{\text{mir}}}{2}. \quad (2.2)$$

This essentially takes the density of an element and that of another element at the location mirrored from the first, and sets both element densities to the average of the two. In this way, the density field \mathbf{s} will become symmetric.

Additive manufacturing

In order to ensure that the optimized geometry is producible by AM, we apply methods to control the minimum feature size and the maximum overhang angle. Furthermore, assuring the presence of enough material at component interface locations requires a specific constraint. These three measures are discussed in more detail below.

Minimum feature size The minimum feature size is controlled by applying a projection-based robust formulation in combination with a density filter (Bruns and Tortorelli, 2001; Wang et al., 2011). Next to ensuring a minimum feature size, this method causes the design to become more robust against shape deviations that might occur during printing.

First, as shown in Fig. 2.2, a length scale is introduced into the design by applying a density filter (Bruns and Tortorelli, 2001), which is standard practice in topology optimization. This converts the symmetrized design \mathbf{s} into a smoothed design \mathbf{d} . Next, by using a projection operator, three designs are produced: a nominal ($\bar{\mathbf{r}}$), an eroded ($\hat{\mathbf{r}}$, *i.e.* shrunk), and a dilated ($\hat{\mathbf{r}}$, *i.e.* grown) design, as is shown in Fig. 2.3. The projection operator is defined as

$$r(d) = \frac{\tanh(\beta\eta) + \tanh(\beta(d - \eta))}{\tanh(\beta\eta) + \tanh(\beta(1 - \eta))}, \quad (2.3)$$

where β is an intensity factor, and η is the cut-off threshold, which takes different values for the three designs. Together with the density filter, the effective minimum feature size is controlled by the density filter radius r_{filt} , the erosion threshold η_{er} , and the dilation threshold η_{di} (Wang et al., 2011).

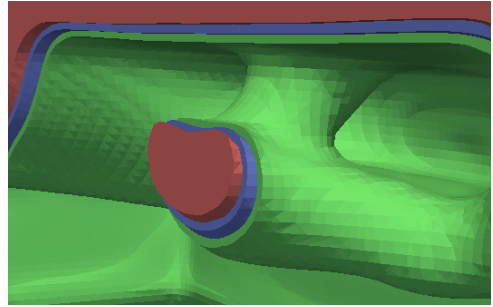


Figure 2.3: A cross-section showing the effect of erosion (red) and dilation (green) on the member size. The nominal structure is displayed in blue.

2

After evaluating the three designs, each will have a different performance. By focusing the optimization on the worst-case scenario (*e.g.* a min-max formulation), the robustness of the final result is improved, and a minimum feature size is obtained (Wang *et al.*, 2011).

In the case of stiffness maximization, it is intuitive that the eroded design always performs worst, as less material means a lower stiffness (Sigmund, 2009). This means that only one finite element solution (that of the eroded design) needs to be calculated, instead of three.

However, the worst-case design is not directly evident when optimizing for maximum eigenfrequencies, since next to the stiffness distribution, the mass distribution also plays an important role. In order to avoid calculating the eigenfrequencies three times, we use an adapted worst-case scenario: the mass-field ρ is dilated (always more mass) and the stiffness-field \mathbf{E} is eroded (always less stiffness), as is indicated in the diagram of Figure 2.2. Using these settings, a single solution of the eigenvalue problem results in worst-case eigenfrequencies, which are lower than the nominal expected value (proof is provided in Appendix A.1). These values are used in the objective function of Eq. 2.1.

Overhang limitation To ensure a maximum overhang angle in the design¹, an overhang filter is used. Effectively, it converts the projected design \mathbf{r} to a printable design \mathbf{p} (Fig. 2.2) by removing all features overhanging beyond a critical angle. In this case, all three designs are filtered, resulting in three printable designs (nominal $\bar{\mathbf{p}}$, eroded $\check{\mathbf{p}}$, and dilated $\hat{\mathbf{p}}$). Note that the combination of the robust method with an overhang filter affects the effective minimum feature size, which could be corrected using more elaborate formulations (Pellens *et al.*, 2019). Naturally, the nominal design $\bar{\mathbf{p}}$ serves as the printable design used for actually printing the part, as indicated by the green box in Fig. 2.2.

The overhang filter as proposed by Langelaar (2016) proceeds layer-wise through the structure and determines the maximum printable density of each element in the layer, which is used as a threshold to limit the original density. The maximum printable density is determined by taking the maximum value of the supporting elements below the current element (3 elements in 2D as illustrated in Fig. 2.4, and 5 or 9 in 3D).

Because in the original formulation discrete elements are used as a support, the effective maximum overhang angle is non-uniform and dependent on the alignment with the Cartesian coordinate system of the mesh Langelaar (2016). Ideally, a printable cone has an axisymmetric maximum overhang angle around the print direction, independent on the

¹Maximum overhang angle as measured from the normal to the buildplate.

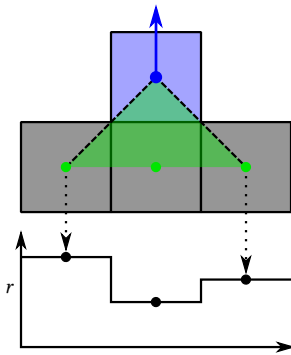


Figure 2.4: Illustration of the original sampling scheme in 2D (Langelaar, 2016), with the graph below showing the element density distribution of the supporting elements. For a vertical print direction (blue arrow), the active element (blue) may be printed if the maximum supporting density is large enough.

mesh. When using 5 support elements, the printable cone is pyramid-shaped (Fig. 2.5a), which is conservative in the off-axis directions with an effective overhang angle of 35° on a cubical mesh. The version with 9 support elements on the other hand shows the opposite behavior, being less restrictive in off-axis directions with an overhang of 55° , which violates the required maximum overhang angle (Fig. 2.5b). Various other overhang prevention approaches have been proposed (e.g., Gaynor and Guest, 2014; Hoffarth *et al.*, 2017; Qian, 2017; Van de Ven *et al.*, 2020b) each differing in effectiveness, complexity, and convergence characteristics.

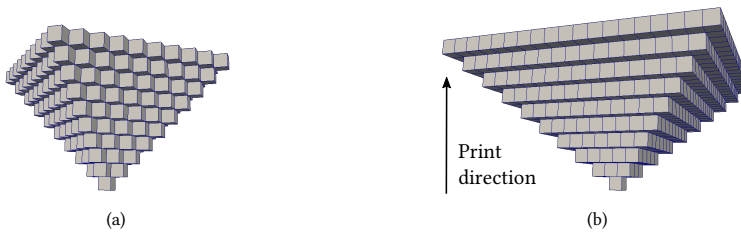


Figure 2.5: The printable cone (the largest printable volume, starting from one element) using the original implementation (Langelaar, 2016), with a 5-element (a) or 9-element support (b).

Here we propose a comparatively simple yet effective improved scheme that still benefits from the regularity of the structured mesh, but reduces the dependency on the mesh. It enables a more accurate geometric description of the maximum overhang angle and additionally enables an arbitrary print direction, a maximum overhang angle other than 45° , and a circular-shaped printable cone. To do this, interpolation is used to sample densities at locations that do not exactly coincide with an element midpoint (Fig. 2.6a). In 2D, a triangle is projected onto the supporting plane, which is the plane passing through the midpoints of the supporting elements. The current element may be printed if the maximum density within the supporting area is large enough. This maximum is located either on one of the element midpoints within the cone or at the boundary, for which linear interpolation is used². By changing the opening angle of the projecting triangle, the max-

²This is only assumed for densities in the overhang filter. For each element in the finite element analysis, its

imum overhang angle can be controlled. A rotation of the triangle results in a change of print direction, as is illustrated in Fig. 2.6b. For this case, elements adjacent to the current element are used for the rotated case, making the supporting surface fold around the corner.

2

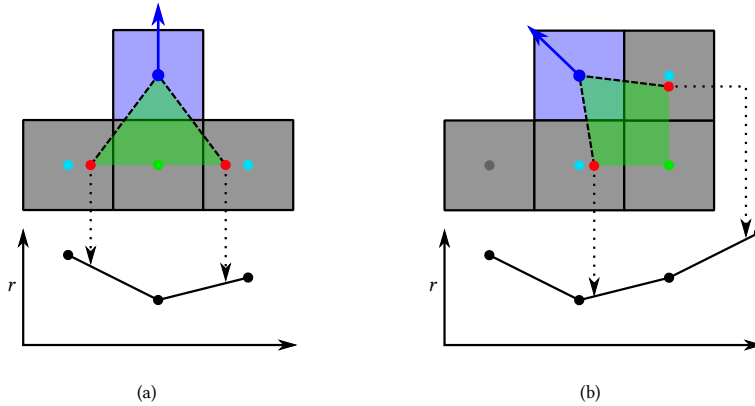


Figure 2.6: The improved sampling scheme in 2D. a) An overhang angle smaller than 45° uses one element midpoint (green) and two interpolation points (red) below the active element (blue) as support. b) A diagonal print direction, where one sampling point interpolates between the two elements to the right of the active element. Elements indicated with cyan are used only in interpolation. The horizontal axis of the density graph is wrapped around the corner.

In 3D, the supporting area is determined by a cone instead of a triangle, as demonstrated in Fig. 2.7. The allowable overhang angle is controlled by the aperture of the cone, and the print direction by its orientation. Just like the two-dimensional case, the maximum printable density is found at one of the element midpoints within the cone or at the perimeter of the cone. A number of equally spaced sampling points is defined along the perimeter, approximating the density value at those locations using bilinear interpolation based on the density values of the four closest elements. The weights used for the bilinear interpolation can be precomputed since a structured grid is used, thus ensuring a computationally efficient overhang filter.

The maximum printable density is now obtained by taking a smooth maximum of both the values at element midpoints encompassed by the cone and the sampled points along the perimeter of the projected cone. Instead of 5 or 9 points, this results in a variable number of points, depending on print orientation, maximum overhang angle, and chosen number of perimeter points. The final step in the overhang filter is to take a smooth minimum of the original density of the current element and the maximum printable density, which is identical to that of the original implementation (Langelaar, 2016).

The printable cone converges to a circular shaped cone by increasing the number of sampling points, as is demonstrated in Figs. 2.8a and 2.8b, correcting the under- and over-estimation as observed in the original 5 or 9 element support (Fig. 2.5). Using the improved

material density is constant throughout.

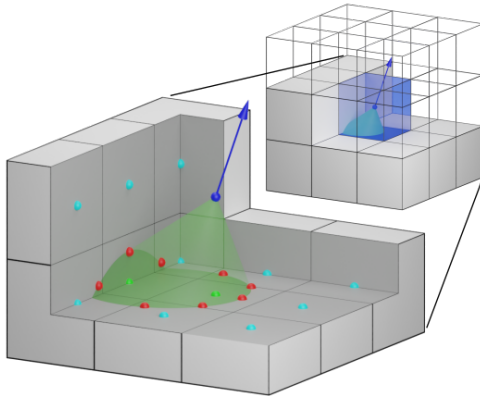


Figure 2.7: The improved sampling strategy with an arbitrary print orientation, indicated by the blue arrow. The maximum printable density of the active element (in blue) is determined by the elements in the direction of the support cone (green). A combination of densities within the cone obtained directly at element midpoint (2x green dots), and interpolated values along the perimeter of the cone (8x red dots) are used in a smooth maximum function.

method, overhang angles smaller than 45° (narrow support cones, Fig. 2.8c) can easily be modeled by simply adapting the shape of the supporting cone, thus sampling at different locations. Additionally, arbitrary printing orientations are enabled by rotating the supporting cone (Fig. 2.8d), instead of requiring domain mapping (Langelaar, 2018a). Also other support patterns, e.g., elliptic cones, are a natural extension to the method.

Note that in order for this refined overhang filter to work correctly, only processed elements are allowed to be accessed. This can be ensured by changing the element traversal pattern, depending on the print direction. In general, for overhang angles above 45° it becomes much more difficult or even impossible to obtain a traversal pattern that ensures all sampled elements are processed. A critical overhang angle of 45° is used for the present study, for which the proposed overhang filter is used for an improved geometric accuracy of the maximum overhang limitation.

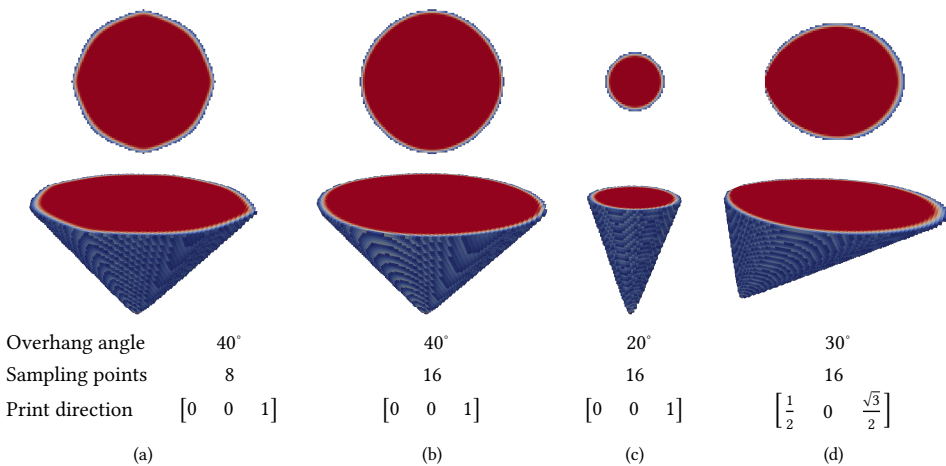


Figure 2.8: The printable cone using different number of sampling points, overhang angle, and orientation, but using the same mesh. The top row shows the top view, and in the bottom row, the perspective view is displayed.

Enforcing interfaces For the assembly of the different components to the printed body, interfaces for bolts need to be generated. This is not evident in the optimization, because there is no incentive to connect the bodies other than for stiffness. In practice, sufficient material is required at bolt locations for a hole to be drilled and threaded, as is illustrated in Fig. 2.9. Only setting the required volume to solid (*i.e.* frozen/non-design area) does not ensure printability of these locations, and they may even be removed by the overhang filter. Therefore, sufficient material is forced at the bolt locations by using an additional constraint (Langelaar, 2018b), as is depicted in Fig. 2.2. This is done by taking the root sum of squares between the density values of the nominal printable design $\bar{\mathbf{p}}$ and their desired value (in this case 1.0), denoted in a formula as

$$g_{\text{sol}} = \frac{1}{N_{\mathcal{F}}} \sqrt{\sum_{i \in \mathcal{F}} (1.0 - \bar{p}_i)^2} - \tau \leq 0. \quad (2.4)$$

The set of elements marked to be solid is denoted \mathcal{F} , the number of elements in this set $N_{\mathcal{F}}$, and a small tolerance value τ is used to allow some slack. In this manner, the optimization process will not only ensure the presence of material at these bolt regions, but also its printability.

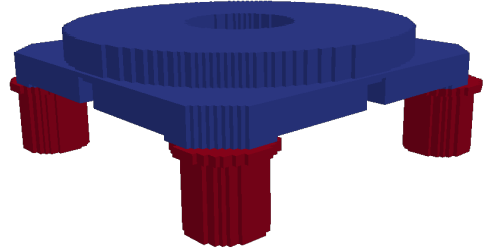


Figure 2.9: One of the magnets (blue), and in red the cylindrical interface volumes large enough for a threaded and bolted connection.

Milling

The next step in the (simulated) production process is milling (Fig. 2.2). After obtaining a printable design, pockets are cleared of support structures, as indicated in Fig. 2.10, where components are to be mounted. Here, by support structures we mean the material that is required for a printable design, but is removed in the milling step. Any support structures generated outside of the milled volume are not removed and are considered a part of the final structure. Adaptive formulations for topology optimization also exist, where support structures (not in benefit to the final performance) are identified and removed throughout the domain, instead of only in a pre-determined volume (Langelaar, 2018b; Van de Ven *et al.*, 2020a). However, this is not incorporated in the current work.

Mathematically the milling is done by taking the printable designs ($\bar{\mathbf{p}}$, $\check{\mathbf{p}}$, and $\hat{\mathbf{p}}$) and setting the entries corresponding to the milled volume to zero as

$$c_i = \begin{cases} 0 & \forall i \in \mathcal{M} \\ p_i & \forall i \notin \mathcal{M} \end{cases} \quad (2.5)$$

where c_i are the entries in design vectors $\bar{\mathbf{c}}$, $\check{\mathbf{c}}$, and $\hat{\mathbf{c}}$, denoting the milled designs and \mathcal{M} represents the elements in the milled volume, which are known *a priori*. Note that in

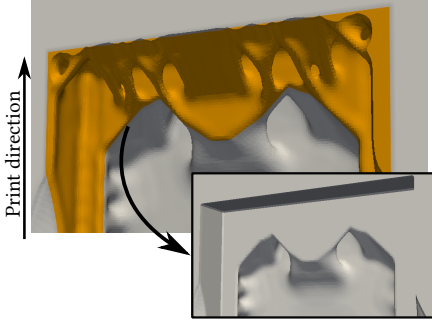


Figure 2.10: A detailed view of support structures (indicated in yellow), which are removed by the milling operation. Supports are required to print the upper side wall of the actuator pocket, and therefore these structures are generated in the optimization process.

this case, no tool access restrictions are involved, since the relevant pockets are always accessible from the base of the chuck. A more complex milling formulation, such as in (Langelaar, 2019), is therefore not required in this case.

As mentioned in Section 2.2.1, the required mass of the unassembled chuck is $M_{\text{lim}} = 7.5$ kg, for which a constraint can be formed at this point (Fig. 2.2). By a simple addition, the volume of the machined chuck frame can be calculated as

$$V = \sum_i \bar{c}_i V_e, \quad (2.6)$$

with V_e the volume of one element. The volume limit V_{lim} is calculated as

$$V_{\text{lim}} = \frac{M_{\text{lim}}}{\rho_{\text{alu}}}, \quad (2.7)$$

with material density ρ_{alu} . Strictly speaking, the volume constraint should be an equality constraint, but since the upper bound is generally active, it can be reduced to an inequality constraint, which is easier to implement in the optimization (Eq. 2.1).

Support structure minimization Since the milled field is used for the volume constraint instead of the printed field, the use of support structures is unbounded, which may lead to excessive material use during the print process. This effect is counteracted by adding a penalty on the volume of removed support structures, keeping the amount of support material to a minimum. The volume of the cleared support structures can simply be calculated from the difference between the nominal printed volume and the volume after milling V (Eq. 2.6) as

$$V_{\text{supp}} = V_{\text{print}} - V, \quad \text{with} \quad V_{\text{print}} = \sum_i \bar{p}_i V_e. \quad (2.8)$$

This value is added to the objective in Eq. 2.1 as a penalty value (Fig. 2.2)

$$g_{\text{supp}} = \alpha \frac{V_{\text{supp}}}{N_{\mathcal{M}}}, \quad (2.9)$$

where the volume is normalized using the number of elements marked for milling $N_{\mathcal{M}}$, and α is a small penalty factor that determines how much focus is on limiting the amount of

support structure. This causes support structures to appear only when they are effective in supporting material beneficial for higher eigenfrequencies. A detail of a resulting structure can be seen in Fig. 2.10.

2

Material interpolation

The material properties of the chuck's milled body are a function of density field \mathbf{c} , as can be seen in Fig. 2.2. They are interpolated using SIMP (Solid Isotropic Microstructure with Penalization), which is a standard method in topology optimization (Bendsøe and Sigmund, 2003). This enforces a penalization on intermediate design variables (neither 0 or 1), and helps the optimization process to converge towards an interpretable black-and-white design. In eigenfrequency optimization often problems are encountered with localized eigenmodes in low-density areas ($c \approx 0$) and their low corresponding frequencies. To alleviate these problems we use the approach proposed by Zhu *et al.* (2009), where a small linear part is added to the usual cubic power of SIMP (Eq. 2.10). This prevents the stiffness from vanishing as compared to the mass for very small densities c . The stiffness \mathbf{E}_p and mass ρ_p distribution of the printed and milled part can be calculated using the eroded $\check{\mathbf{c}}$ and dilated $\hat{\mathbf{c}}$ density fields, respectively, as

$$\begin{aligned} E_{p,i} &= E_{\text{alu}} \left(c_{\min} + (1 - c_{\min}) (0.1\check{c}_i + 0.9\hat{c}_i^3) \right), \\ \rho_{p,i} &= \rho_{\text{alu}} \hat{c}_i, \end{aligned} \quad (2.10)$$

where a minimum design variable c_{\min} prevents the system matrices from becoming (more) singular. In the current design case the matrices are already singular because of rigid-body-modes, but these modes are known analytically and accounted for, as is explained in Section 2.2.2.

Component assembly

At this point the distribution of density and elasticity modulus is known throughout the milled product, and the components (magnets and measurement bar) can be added (Fig. 2.2). Similar to the milling operation, this is done by setting the entries in the final material properties (\mathbf{E} and ρ) to either that of the milled part or to that of the components as

$$E_i = \begin{cases} E_{c,j} & \forall i \in \mathcal{C}_j \\ E_{p,i} & \forall i \notin \bigcup_j \mathcal{C}_j \end{cases} \quad (2.11)$$

and

$$\rho_i = \begin{cases} \rho_{c,j} & \forall i \in \mathcal{C}_j \\ \rho_{p,i} & \forall i \notin \bigcup_j \mathcal{C}_j, \end{cases} \quad (2.12)$$

where $E_{c,j}$ and $\rho_{c,j}$ denote the modulus of elasticity and density for each component with elements \mathcal{C}_j .

Bolted interfaces are modeled by connecting two components with a patch of solid material (Fig. 2.11). Since all components are modeled in the same mesh, the connecting patch is 1 element thick. The diameter of the patch is calculated according to a 30° frustum starting at the bolt head, corresponding to the pressure cone of the bolt (Budynas and Nisbett, 2006). In this way the bolts are modeled in an effective, yet simple manner.

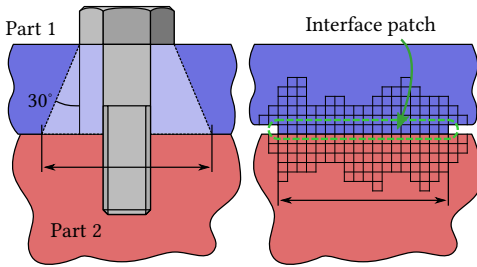


Figure 2.11: A bolted interface with indicated frustum, used to determine the patch diameter (left). The two discretized parts are connected by a solid patch of 1 element thickness (right).

Geometry mapping The CAD geometry of the magnetic actuators is converted to a 3-dimensional structured grid (voxel grid) by using a rasterizing algorithm, also called solid voxelization. Effectively, this means that all the elements of which the center-point is inside the solid CAD geometry are detected, and placed into the sets \mathcal{C}_j representing the different components. The result of this operation can be seen in Fig. 2.12.

The voxelization is implemented as a simple scanline algorithm (see, e.g., [Foley et al., 1993](#)) in three dimensions. Rays are cast in each axis-aligned direction, through the center of each element in the mesh. For each ray, intersection with the geometry is tested, which generally results in one or multiple pairs of entry-exit intersections. When an element is within an intersected range of all three the x , y , and z -directions, its center is inside the geometry and thus can be marked as part of the considered geometry set \mathcal{C}_j . This process only needs to be done once, prior to the optimization.

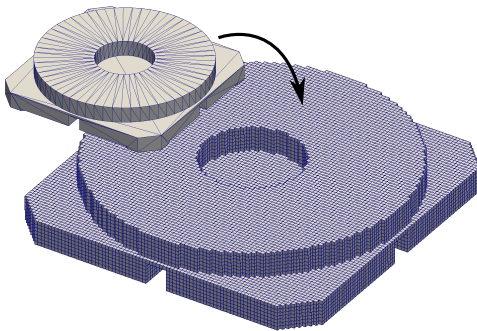


Figure 2.12: An example of voxelization, where the original boundary representation of a magnet and its mount (top left) is mapped onto a 1 mm grid (bottom right).

Finite element modeling

The entire domain is discretized into a grid of trilinear hexahedral solid elements with a full integration scheme and dimensions $1 \times 1 \times 1$ mm, corresponding to the design resolution. For each of the elements, the material properties associated with the respective components and/or optimization variables have been determined by the preceding steps shown in Fig. 2.2, where the (penalized) Young's modulus \mathbf{E} and the mass density ρ depend on the eroded \hat{c} and dilated \hat{c} design fields, respectively (Eqs. 2.10-2.12). Following standard topology optimization procedure, the stiffness \mathbf{K} and mass \mathbf{M} matrices can be constructed by linear scaling of each element i with the (penalized) Young's modulus E_i

and density ρ_i as

$$\mathbf{K} = \bigoplus_i^{N_{el}} E_i \mathbf{K}_0 \quad \text{and} \quad \mathbf{M} = \bigoplus_i^{N_{el}} \rho_i \mathbf{M}_0, \quad (2.13)$$

where \mathbf{K}_0 and \mathbf{M}_0 represent the unit stiffness and mass element matrix, and the operator \mathbf{A} represents the matrix assembly. The two element matrices are identical throughout the domain, since a structured mesh of equal-sized elements is used.

After assembly, the next step in Fig. 2.2 is to calculate the eigenfrequencies. The three lowest eigenfrequencies are found as solutions to the generalized eigenvalue problem, denoted as

$$\begin{aligned} (\mathbf{K} - \Omega_i^2 \mathbf{M}) \boldsymbol{\phi}_i &= \mathbf{0} \quad \text{for } i = 1, 2, 3 \\ 0 < \Omega_1 &\leq \Omega_2 \leq \Omega_3, \end{aligned} \quad (2.14)$$

where Ω_i and $\boldsymbol{\phi}_i$ are the structural eigenfrequencies and their corresponding eigenvectors. The entire analysis domain (including all components) consists of a total of 9.0 million elements, and 27.6 million degrees of freedom. This very large number of degrees of freedom poses a computational challenge, especially because calculating a single eigenfrequency is already an order of magnitude more expensive than the solution of a static response.

For an efficient solution, we resort to parallelization of the problem. The finite element routines are implemented using the PETSc library (Balay *et al.*, 2019), which provides parallel linear solvers, data structures for parallelization, and domain decomposition. For the solution of the eigenfrequencies (Eq. 2.14), specialized eigensolvers are used from the SLEPc library (Hernandez *et al.*, 2005), which is an add-on to PETSc. A Krylov-Schur algorithm with a shift-and-invert strategy is used to obtain the three lowest eigenfrequencies Ω_i and corresponding eigenvectors $\boldsymbol{\phi}_i$. In the calculation of eigenvalues, the repeated solution to a large linear system of equations is required, for which we use the iterative Stabilized BiConjugate-Gradient (BiCGStab) method, preconditioned with an algebraic multigrid preconditioner.

Since the motion stage is free-floating, no boundary conditions are present, making the stiffness matrix singular. To prevent numerical problems in the solvers, deflation is used to account for the six rigid body modes (*i.e.* nullspace) in both the eigensolver and its internal linear solver. The deflation ensures a solvable linear system of equations and prevents recomputation of the rigid body modes, which are already known explicitly (Geradin and Rixen, 2015). Further details on the aforementioned algorithms can be found in the PETSc and SLEPc documentation (Balay *et al.*, 2019; Hernandez *et al.*, 2005).

Settings

In Table 2.1, all settings as used in the optimization can be found. To help convergence, the first few iterations the overhang filter is not active, but is gradually phased in during iterations 15-65, reducing the aggressiveness of this filter (similar approach as by [Van de Ven et al. \(2020b\)](#)). Also the robustness factor β is gradually increased during the optimization process in iterations 10-90. The chosen filter radius and erosion/dilation thresholds result in an effective minimum feature size of $2r_{\text{filt}}\sqrt{\eta_{\text{er}} - 0.5} \approx 3.2$ mm, according to [Trillet et al. \(2021\)](#).

Table 2.1: Options and settings as used in the optimization

Symbol	Value	Description
E_{alu}	65 GPa	Young's modulus (aluminium)
ρ_{alu}	2700 kg/m ³	Density (aluminium)
E_{neo}	160 GPa	Young's modulus (neodymium)
ρ_{neo}	7500 kg/m ³	Density (neodymium)
E_{ss}	200 GPa	Young's modulus (stainless steel)
ρ_{ss}	8000 kg/m ³	Density (stainless steel)
ν	0.3	Poisson's ratio (all materials)
c_{min}	10 ⁻⁵	Minimum density
r_{filt}	5 mm	Filter radius
η_{er}	0.6	Erosion threshold
η_{di}	0.4	Dilation threshold
β	10 ⁻⁹ -10 ¹	Projection intensity factor
	45°	Overhang angle
	8	Overhang sampling points
τ	10 ⁻⁵	Solid constraint tolerance
α	10 ⁻⁶	Support structure penalty factor

2.3 Demonstrator and experimental validation

After the optimization, a final geometry is obtained as shown in Fig. 2.13a. This geometry is the iso-surface of the voxel grid of the nominal printable design $\bar{\mathbf{p}}$ at a density value of 0.5. The iso-surface can be generated using the marching cubes algorithm, which is implemented in, e.g., the open source visualization application Paraview (Ahrens *et al.*, 2005). The support structures and required volumes for component interfaces can clearly be identified. In Fig. 2.13b, the internal structure of the chuck can be seen. The final geometry contains several enclosed voids, which were not accounted for during the optimization. To prevent trapped metal powder, the enclosed voids are removed by manual post-processing. Four small voids were converted to solid material, and for the large void in the center, two holes were added for powder removal after printing, as indicated in Fig. 2.13b.

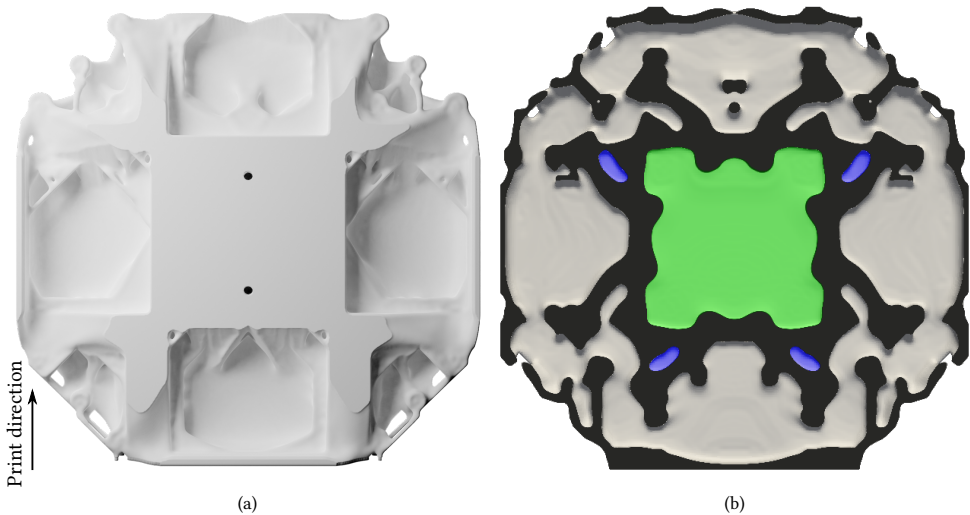


Figure 2.13: a) The (printable) geometry of the optimized chuck. b) Cross-section of the geometry, showing the internal structure of the chuck. Several small enclosed voids are removed (blue) and for the large cavity in the middle (green), extra holes are added to allow powder evacuation.

The evolution of the eigenfrequencies throughout the optimization is shown in Fig. 2.14, from which can be seen that the final frequencies are 607, 763, and 897 Hz. However, these values refer to the robust worst-case design (Section 2.2.2). From a verification analysis on the nominal design, we find the expected eigenfrequencies as 667, 837, and 1011 Hz. The corresponding mode shapes (Fig. 2.15) are as expected from a fairly flat plate; a torsional, saddle, and umbrella mode.

To get an indication of the optimized performance relative to other designs, three reference cases are established. The first two reference designs use a 100% material inside the design domain (Fig. 2.16a). Since the chuck is originally optimized with a volume fraction of 50%, the mass of a completely solid chuck will double. Therefore, the first reference has equal height to the optimized chuck, but doubled mass. In the second reference design, the height of the chuck is reduced such that the mass is equal to that of the optimized

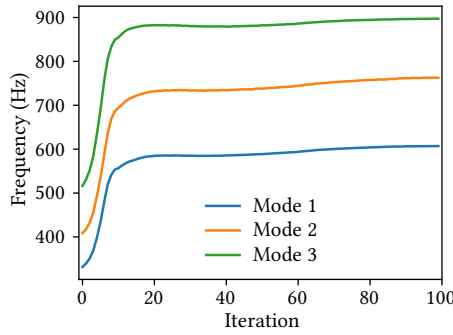


Figure 2.14: Iteration history of the eigenfrequencies.

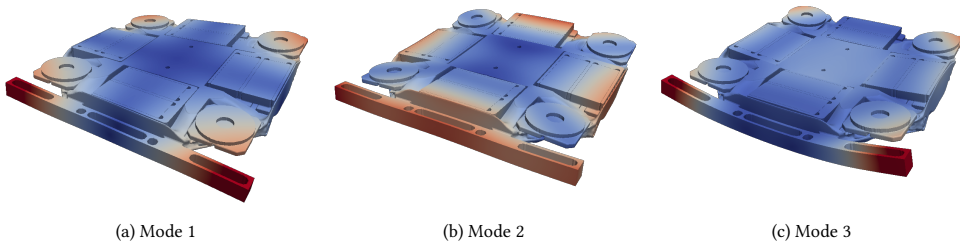


Figure 2.15: a) The first eigenmode at 667 Hz (torsion mode). b) Second eigenmode at 837 Hz (saddle mode). c) Third eigenmode at 1011 Hz (umbrella mode).

design. And thirdly, a conventional and manually designed chuck (with equal mass and dimensions to the optimized design) is analyzed (Fig. 2.16b). An overview of the results for these variations can be found in Table 2.2. The optimized design clearly outperforms all reference chucks. With respect to solid designs, the performance is roughly doubled, or the mass can significantly be reduced while still increasing performance. When compared to a conventional and manually designed chuck, also a considerable performance increase of about 15% can be realized.

Table 2.2: Results of the numerical comparison between optimized and reference designs. (*) Mass of the machined part only, excluding any components.

	Units	Optimized	Reference designs		
			Equal mass	Equal height	Conventional
Mass*	kg	7.5	7.5	15	7.5
Height	mm	48	30	48	48
Mode 1	Hz	667	353 -47%	569 -15%	547 -18%
Mode 2	Hz	837	414 -51%	815 -2.6%	735 -12%
Mode 3	Hz	1011	525 -48%	944 -6.6%	880 -13%

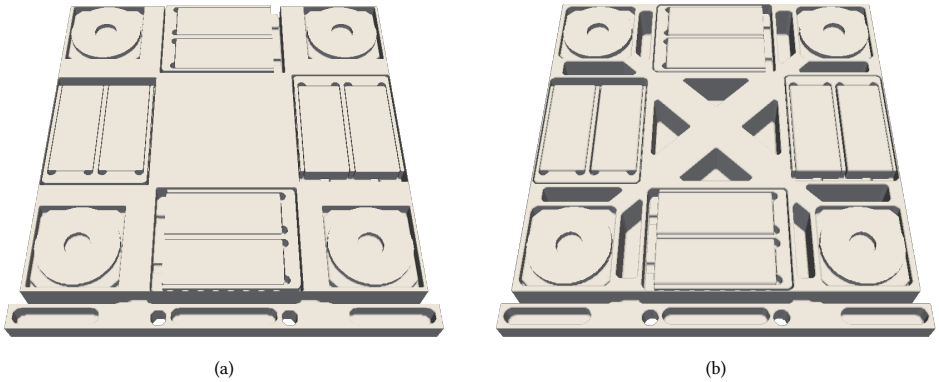


Figure 2.16: a) Solid reference design, with equal mass or equal height. b) Conventional reference design, with equal mass and equal height.

In terms of computational time, the entire optimization took 25 hours. This means that each of the 100 design iterations which were performed, requires an average of 15 minutes. The computations were executed on a 192-core computing node (8× Intel Xeon 8168 24-core CPU and 1536GB of memory).

2.3.1 Additive manufacturing

For larger and complex designs, the part orientation in the build chamber is the key element for successful printing. Since print orientation is fixed throughout the optimization, several part orientations have been analyzed prior to the optimization. Finally, it was chosen to orient the part vertically for minimal stress in the horizontal plane, to limit the amount of support structures required, and for an easy part separation from the build-plate. The disadvantage of this approach is the need to use the full build height, the initial powder investment, and longer job duration due to the recoater time. However, this is offset by the opportunity to print multiple parts simultaneously (up to 4 in one job) and allowing the use of multiple lasers in the MetalFAB1 system (Additive Industries, 2021). No extra support structures nor any further adaptations to the design were required, as the overhang filter enforces a self-supported design (Section 2.2.2).



Figure 2.17: The first print attempt, showing the locally overheated and deformed parts, causing recoater damage.

The first print was halted due to too large heat accumulation at the connection of two overhanging areas. Locally melted material protruded above the powder bed, resulting in recoater damage (Fig. 2.17). Incorporation of a process-based simulation of the printing process into the optimization can potentially avoid these kind of failures, and help in obtaining a first-time-right print, although its computational feasibility is currently out of reach for the design resolution targeted in this study (Misiun *et al.*, 2021). After reorienting the parts with respect to the recoater, the build job ran smoothly over the full part height (Fig. 2.18a). The selected print parameter settings are balancing productivity (30 μm layer thickness) and density, resulting in an ‘as printed’ density above 99.95% (from cross-sectional analysis) of the AlSi10Mg material. Two parts were printed simultaneously in a total of 10 days, effectively resulting in 5 days build time per part.

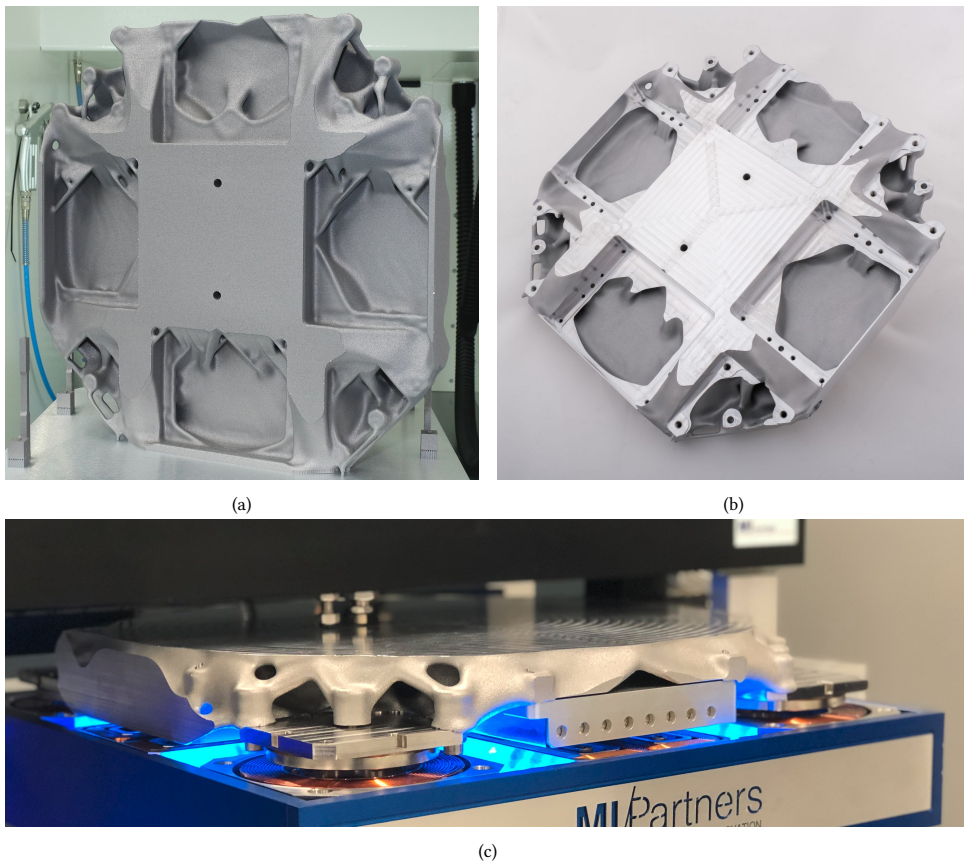


Figure 2.18: a) The printed chuck after the powder-bed fusion process is finished. b) After machining, support structures are removed and interfaces for the components added. c) Assembled chuck in operation, levitated above the long-stroke stage.

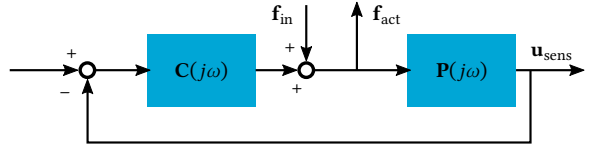
In order to achieve surface and dimensional requirements for the interfaces of all the magnets which cannot be achieved by the printing process, the part is post-processed by

traditional machining methods (Fig. 2.18b). The final step is to assemble the magnets and mount the chuck on the long-stroke chuck, making it ready for usage (Fig. 2.18c).

2.3.2 Validation

The chuck position in all six degrees of freedom is actively controlled by a closed-loop feedback loop, which can be used for a frequency-response measurement (Fig. 2.19). Five eddy current sensors and one laser interferometer provide position measurement of the chuck, and eight (sets of) permanent magnets are able to apply forces on the chuck when placed in magnetic fields generated by external voice coils (Fig. 2.1). A force or moment can be applied on the different degrees of freedom of the chuck $\mathbf{f}_{\text{act}}(t) = [F_x, F_y, F_z, M_x, M_y, M_z]$ by applying a load on multiple actuators simultaneously. Similarly, displacements in global degrees of freedom $\mathbf{u}_{\text{sens}}(t) = [U_x, U_y, U_z, \theta_x, \theta_y, \theta_z]$ (translations or rotations) are obtained by a linear combination of the different sensor signals. Further details on sensing and actuation in this multi-input multi-output system can be found in [Laro et al. \(2013\)](#); [Van der Veen et al. \(2017\)](#).

Figure 2.19: Feedback loop with indicated measurement signals for experimental validation of the stage.



By adding an harmonic disturbance signal $\mathbf{f}_{\text{in}}(t)$ to the input forces (Fig. 2.19), the behavior of the structure can be obtained independently of the controller. After taking the discrete Fourier transforms of these signals into the frequency domain, the sensitivity function $\mathbf{S}(j\omega)$ and the process sensitivity function $\mathbf{R}(j\omega)$ can be calculated ([Munnig Schmidt et al., 2011](#)) as

$$S_{ij}(j\omega) = \frac{f_{\text{act},i}(\omega)}{f_{\text{in},j}(\omega)} \quad R_{ij}(j\omega) = \frac{u_{\text{sens},i}(\omega)}{f_{\text{in},j}(\omega)}, \quad (2.15)$$

which are multi-input multi-output (*i.e.* matrix) transfer functions. Using the analytical relations of these two transfer functions

$$\begin{aligned} \mathbf{S}(j\omega) &= (\mathbf{I} + \mathbf{P}(j\omega)\mathbf{C}(j\omega))^{-1} \\ \mathbf{R}(j\omega) &= \mathbf{P}(j\omega)(\mathbf{I} + \mathbf{P}(j\omega)\mathbf{C}(j\omega))^{-1}, \end{aligned} \quad (2.16)$$

the transfer function of the original plant can be extracted as

$$\mathbf{P}(j\omega) = \mathbf{R}(j\omega)\mathbf{S}(j\omega)^{-1}. \quad (2.17)$$

Here, the multi-input multi-output transfer functions of plant and controller are denoted $\mathbf{P}(j\omega)$ and $\mathbf{C}(j\omega)$, respectively.

From the frequency response functions of the two out-of-plane rotations (tip and tilt), shown in Fig. 2.20, the resonance peaks can clearly be identified, which occur at the eigenfrequencies of the chuck. This leads to the experimentally determined eigenfrequencies, which are summarized in Table 2.3. It is seen that the predicted and measured frequencies are in close agreement, with a discrepancy of around 1%.

Table 2.3: Experimental validation of the optimized design.

	Units	Numerical	Experimental	
Mode 1	Hz	667	673	-0.9%
Mode 2	Hz	837	829	+1.0%
Mode 3	Hz	1011	1021	-1.0%

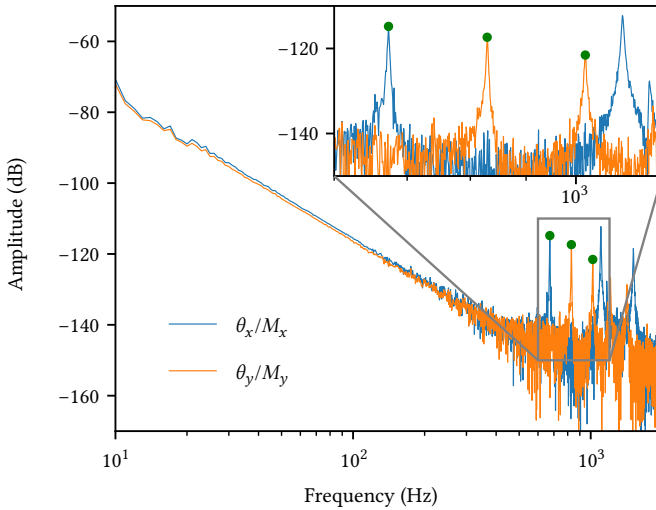


Figure 2.20: Frequency response functions of the two out-of-plane rotations.

2.4 Discussion

In the current work, topology optimization is combined with AM for a high-performance dynamic application of industry-relevant complexity. The fact that an optimal design is reached in 25 hours, is paramount for practical use. When dimensions or component positions change, re-runs are necessary. The fast design time also facilitates comparative studies of different product requirements by running multiple optimizations. Especially for repeated optimization of customized products, where the design goal (*e.g.* performance) is similar, these techniques can have a huge benefit in terms of automation. In fields where time-to-market is important, a fully automated pipeline from concept to production could be made, only requiring the optimization structure to be set up once.

The superior performance of the optimized chuck as compared to reference designs (Table 2.2) clearly demonstrates the added benefit of combining topology optimization with AM. Recently, advances in topology optimization of 5-axis milling have been made (Guest and Zhu, 2012; Langelaar, 2019). It would be worthwhile to investigate the performance benefit of combining AM and topology optimization, as compared to combining milling and topology optimization, or even the combination of all three methods.

In the current design, the only manual post-processing operation required is the removal of enclosed voids. In the large central void, two access holes were added to release the metal powder (as seen in Fig. 2.18a), and four other small voids were removed by converting them to solid material. However, these modifications can have a detrimental effect

on the final performance. In this case the effects are negligible, but this is not a certainty in general. Therefore, the avoidance of enclosed voids should be taken into account during the optimization. This is still an ongoing research topic, where promising methods have been proposed in recent years (e.g., [Li et al., 2016](#); [Gaynor and Johnson, 2020](#)).

The optimized design is experimentally validated with a discrepancy of around 1%. This indicates that the modeling using a structured mesh that does not exactly represent the geometry still yields accurate results. However, the accuracy will most likely deteriorate for coarser mesh sizes, because the geometric error in the voxelization process will increase. Next to this, it can also be hard to model small gaps between components, which are linked to the element size, in this case 1 mm. Possible solutions include the use of substructuring for passive components ([De Klerk et al., 2008](#); [Koh et al., 2020](#)).

For the application of a high-precision motion stage, the eigenfrequencies are not the only important aspect in the final performance. Accurate positioning is achieved by closed-loop feedback control, making the controller and controller-structure interaction equally important. By simultaneous optimization of both the controller and structure, even better performance in terms of bandwidth and positioning accuracy can be expected ([Van der Veen et al., 2017](#)), which is an area for future research.

2.5 Conclusion

In this work, we have demonstrated a fast and systematic process for the design of structures with high dynamic performance, exploiting the combination of additive manufacturing and topology optimization. The methodology is demonstrated using the design case of a high-precision motion system and is applicable to a wide range of industrial applications requiring high eigenfrequencies. All steps of the manufacturing process (additive manufacturing, milling, and assembly) are incorporated into the optimization procedure. This results in optimized designs that are almost directly producible. Only minimal manual modifications were required to remove enclosed voids, otherwise trapping the metal powder used in the laser powder-bed fusion process.

Specifically in the overhang filter, an improved sampling scheme was proposed to allow more freedom in the choice of overhang angle and print direction. This scheme represents the geometric overhang more accurately in a Cartesian grid and is less dependent on the orientation of the grid.

Small geometric features require a fine design resolution, which comes at a computational cost. In the current work, external components are added by voxelization into the same mesh. This has the benefit of only having one mesh, but the disadvantage is that components may only be separated from each other by a minimum gap size of one element. More effective inclusion of components for dynamic structures remains a direction for future research.

A novel cost-effective robust formulation was proposed to allow feature size control without computation of additional eigenvalue problems. By combining the eroded design field for the stiffness matrix and the dilated for the mass matrix, a worst-case estimate is obtained, effectively reducing the computational cost by a factor 3 for the calculation of eigenfrequencies. In this design case, a new optimal design is generated in 25 hours using 192 CPU cores, which enables practical use and opens new opportunities for design methodology of industrial applications.

As is expected, the optimized design achieves superior performance. In the current design case of a high-precision motion stage, a performance increase of around 15% is reached as compared to conventional designs. Additionally, the optimized design is experimentally validated with a measured performance within 1% of the simulated performance. Not only does this reinforce the confidence that the performance can be predicted correctly, especially in this example with multiple components, but that also the manufacturing considerations of the optimization are sufficient for production. Using the outlined approach, this study demonstrates that the benefits of topology optimization in combination with additive manufacturing can be transferred to industrial high dynamic applications, where superior performance often is the driving factor.

Even further improvements in performance may be achieved by optimization on a system level. In the case of a high-precision motion system, the controller and the closed-loop interaction with the structure are as important as the structure itself. Therefore, this provides a valuable research direction for the next generation of dynamic systems.

3

Limitation of resonances

In many engineering applications, the dynamic frequency response of systems is of high importance. In this paper, we focus on limiting the extreme values in frequency response functions, which occur at the eigenfrequencies of the system, better known as resonant peaks. Within an optimization, merely sampling the frequency range and limiting the maximum values results in high computational effort. Additionally, the sensitivities of this method are not complete, since only information about the resonance peak amplitude is included. The design dependence with respect to the frequency of the extreme value is missed, thus hampering the convergence. To overcome these difficulties, we propose a constraint which can efficiently and accurately limit resonant peaks in a frequency response function. It has a close relation with eigenfrequency maximization, however in that case the amplitudes of the frequency response are unconstrained. In order to keep the computational time low, efficient implementation of this constraint is studied using reduced-order models based on modal truncation and modal truncation augmentation. Furthermore, approximated sensitivities are investigated, resulting in a large computational gain, while still yielding very accurate sensitivities and designs with almost equivalent performance compared to the non-approximated case. Conditions are established for the accuracy and computational efficiency of the proposed methods, depending on the number of peaks to be limited, numbers of inputs and outputs, and whether or not the system input and output are collocated.

3.1 Introduction

The dynamic behavior of structures is a key aspect of the design process for many engineering applications. A frequency response function (FRF) expresses the amplification of the system under harmonic dynamic excitation, which is a critical aspect of its functionality. In some applications, the maximum response must be limited, for example in the case of sensitive equipment which needs protection (Tsai and Lin, 1994), for limiting acoustic transmission (Fesina *et al.*, 2017), or in systems for high positioning accuracy (Van der Veen *et al.*, 2017). Alternatively, a transmission ratio at a resonance frequency might be limited from below, for instance in sensor equipment which needs a minimum response (Xia *et al.*, 2014).

Many engineering applications focus on maximizing eigenfrequencies in order to extend the bandwidth or the operating frequency range. Doing this manually is a time-consuming and difficult iterative process. With structural optimization methods this iterative process can be performed automatically. Specifically, topology optimization is a very powerful approach, since no initial concept needs to be given, and a wide range of resulting shapes and layouts is possible (Sigmund and Maute, 2013). For the classical problem of optimizing eigenfrequencies, many approaches already have been proposed, see, *e.g.*, Zargham *et al.* (2016) for an overview. Several methods exist to maximize specific eigenfrequencies (Diaz and Kikuchi, 1992; Ma *et al.*, 1995), to create a gap between two eigenfrequencies (Jensen and Pedersen, 2006), or to obtain eigenfrequencies close to desired frequencies (Ma *et al.*, 1994). However, resonance occurs when a structure is harmonically excited at the eigenfrequencies, causing extreme responses. This phenomenon has received no attention in all the aforementioned methods.

Besides eigenfrequencies and eigenmodes, the dynamic behavior of a system is also determined by the geometric location and direction of both the input load and the output at which displacement is observed. Some optimization formulations focus on minimizing the vibrational amplitude for steady-state periodic loading (*i.e.* dynamic compliance) at a specific operating frequency (Ma *et al.*, 1993; Jog, 2002; Du and Olhoff, 2007a). Alternative objective functions have recently been studied more extensively to improve convergence of these problems, especially for operating frequencies above the first natural frequency, based on the input power (Niu *et al.*, 2018; Silva *et al.*, 2020). Instead of one specific working frequency, others focus on minimizing the frequency response amplitude over a range of frequencies (Ma *et al.*, 1993; Yoon, 2010; Shu *et al.*, 2011; Liu *et al.*, 2015). However, for some applications only the peak amplitudes of a frequency response within a range of frequencies are of importance. The minimization of maximum frequency response amplitude in the entire frequency range (*i.e.* the H_∞ -norm) is shown for a sizing optimization of a beam model (Venini and Pingaro, 2017), but not yet in a topology optimization setting.

The approach of Venini and Pingaro (2017) could be used to limit the maximum value of the FRF, schematically shown in Fig. 3.1. It relies on an iterative search to obtain the frequency corresponding to the maximum amplification (Bruinsma and Steinbuch, 1990). However, this algorithm requires many evaluations of the FRF and the solution of additional eigenvalues, making it infeasible for practical use in large scale continuum problems. Especially in cases with low damping, where very sharp resonance peaks are present, extra search iterations are needed to obtain the maximum value with sufficient accuracy, adding further to the computational cost. Furthermore, the optimization con-

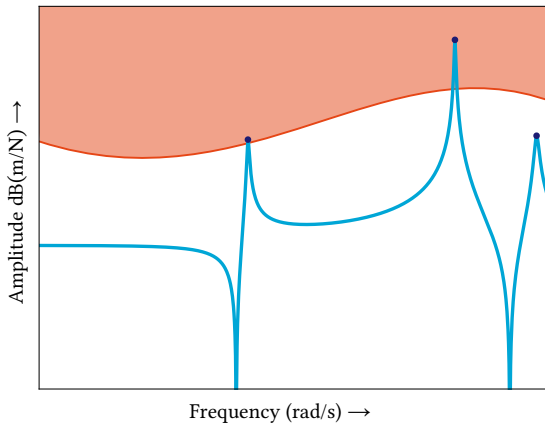


Figure 3.1: Resonant peaks of the frequency response function are not allowed to be above the indicated limit.

vergence with this method is slow, because sensitivity information regarding the resonant peak is incomplete. The sensitivities include information on the maximum peak amplitude, but not on the frequency at which the peak is located. Additionally, by only focusing on the maximum peak frequency, the multi-modal nature of the peak amplitudes is not captured. This means that whenever the amplitude of one or more peaks are close to the maximum peak amplitude, a small design change could cause one of the other peaks to become the maximum peak, leading to a jump in peak frequency and a non-smooth behavior in maximum peak value. Only using the maximum peak value also limits practical uses such as individually constraining peaks at distinct levels, or upper limits which are a function of frequency (see Fig. 3.1). This motivates the present study of constraining a finite number of peak amplitudes in a set of multiple frequencies, instead of only considering the global maximum peak. Other implementations of a resonant peak constraint, which can overcome the above limitations, have not been studied, to the best of our knowledge.

For each point in the frequency response function, a different complex-valued linear system needs to be solved, which involves tremendous computation time for large scale problems, even for only a few frequency points. Additionally, a second linear system needs solving in the case of non-self-adjoint problems, increasing the computational effort even more. Computation time could be saved by using a reduced-order model, requiring at each frequency point only a small system to be solved. Many different methods exist to create reduced-order models tailored for a wide variety of applications, see, *e.g.*, [Besselink *et al.* \(2013\)](#). In the field of structural dynamics, the most common is modal truncation (MT), where eigenvectors are used to create the reduced-order model. An alternative is modal truncation augmentation (MTA), where a reduction basis consisting of eigenvectors is augmented with correction vectors, to compensate the errors introduced by the removal of higher-frequency modes (for detailed information, see, *e.g.*, [Rayleigh \(1945\)](#); [Dickens *et al.* \(1997\)](#); [Craig and Kurdila \(2006\)](#); [Besselink *et al.* \(2013\)](#)). Both these methods are suitable for approximating the low-frequency range with high accuracy.

When using a reduced-order model, calculating the frequency response function becomes inexpensive, but to calculate fully consistent sensitivities, the design dependence of the base vectors has to be taken into account ([Hooijkamp and van Keulen, 2018](#)). These

base vector sensitivities are expensive and usually involve the solution of a full linear system per base vector. A possible reduction in computational cost can be achieved by neglecting the sensitivities of the reduction basis. Using such approximate sensitivities, Han (2012) investigates frequency response sensitivities for a Krylov-based reduced-order model, and concludes that the sensitivities are still usable although some degree of accuracy is lost. Furthermore, Yoon (2010) reports the approximate sensitivities hamper the optimization process due to their inaccuracy in non-self-adjoint problems. The direct reason for this lack of accuracy has not yet been clarified. The reduction method is usually chosen such that the response, in this case a resonance peak, is most accurate. However, in an optimization the sensitivities are driving, thus in addition to an accurate response, the accuracy of the sensitivities is equally important.

We propose a constraint which can effectively limit extreme values in an FRF (Fig. 3.1), where our focus is on weakly damped structures. Using the eigenfrequencies of a mechanical system, which are related to the peak values of the FRF, a lower or upper limit can be set on the resonant peaks. Each eigenfrequency of interest is individually constrained to take care of the non-smoothness problem of the maximum amplitude described earlier, i.e. jumps in frequency corresponding to the maximum resonant peak are not possible. Additionally, having a constraint per resonant peak enables individual peaks to be limited by distinct limits, and the use of frequency-dependent limit functions becomes possible, thus providing a more flexible constraint than the approach of Venini and Pingaro (2017), who only use the maximum resonant peak value. Furthermore, by including the eigenvalue sensitivity information, our sensitivities become consistent with the resonance frequency and thus more accurate. To limit the time spent in calculating the resonance peak amplitudes and their sensitivities, we propose to use reduced-order models with approximated sensitivities. Using the reduction strategies MT and MTA, the accuracy and optimization convergence of the approximated sensitivities is investigated for both self-adjoint and non-self-adjoint problems. The implementation uses density-based topology optimization, but can be applied to other topology optimization approaches as well (Sigmund and Maute, 2013). For clarity, we will limit ourselves to the SISO case, but the method is also extendable to MIMO cases.

The paper is organized as follows. In Section 3.2, the considered finite element model is introduced, followed by the definition of the optimization problem. The proposed constraint is explained in detail, by either solving full systems or model reduction techniques (MT and MTA). Additionally, for the reduction methods, both the consistent and approximate sensitivity calculation is described. Section 3.3 studies the different implementations using both self-adjoint and non-self-adjoint test cases. The performance of the approximated sensitivities are inspected and also their effect on the optimization is shown. Next to that, results of some variations in limit functions are given, to show potential in practical use.

3.2 Methods

3.2.1 Dynamic response modeling

Working towards a model suited for topology optimization, we first establish the considerations used regarding design parametrization and secondly, the numerical modeling of the dynamic response. Since density-based topology optimization is used, each element's elasticity and density is scaled continuously according to the design variables \mathbf{x} between x_{\min} (void) and 1 (solid) (Bendsøe and Sigmund, 2003). First, the design variables are filtered using a spatial density filter, resulting in filtered design variables $\boldsymbol{\rho}$ (Bruns and Tortorelli, 2001). To force the optimizer to a clear solid/void design, intermediate density variables are penalized using scaling factors for the element matrices of stiffness κ and mass μ , respectively, as

$$\kappa_i = (1 - w)\rho_i^p + w\rho_i \quad \text{and} \quad \mu_i = \rho_i. \quad (3.1)$$

This penalization was investigated by Zhu *et al.* (2009) in order to prevent low-frequency eigenmodes of void areas, which often hamper topology optimizations using eigenfrequencies. For the scaling of stiffness, it uses a combination of a linear term (weighted by w) and a part with exponent p .

For the discretization we use bi-linear quadrilateral finite elements, a 2×2 Gaussian quadrature, and assume a plane strain condition. The stiffness and mass matrices are assembled, respectively, by

$$\mathbf{K} = \mathbb{A}_i^{n_{el}} \kappa_i \mathbf{K}_{el}^{(i)} \quad \text{and} \quad \mathbf{M} = \mathbb{A}_i^{n_{el}} \mu_i \mathbf{M}_{el}^{(i)}, \quad (3.2)$$

with the assembly operator \mathbb{A} and the element matrices denoted $\mathbf{K}_{el}^{(i)}$ and $\mathbf{M}_{el}^{(i)}$.

We introduce damping in the form of structural damping (i.e. hysteresis), often used in airplane vibrations and flutter analysis, which is proportional to displacement. Effectively, a damping factor of η is used to create a complex stiffness (Craig and Kurdila, 2006). This kind of damping does not change the frequencies at which the peak amplitudes occur, which means the undamped eigenfrequencies can directly be used. A viscous damping such as Rayleigh or modal damping could also be used without adding computational effort, as the damped eigenfrequencies correspond to the peak amplitudes in that case, which can be calculated as a simple correction on the undamped eigenfrequencies.

Using a steady-state SISO system with harmonic inputs and outputs for the sake of simplicity, the discretized N -dimensional frequency-domain system of equations is

$$\begin{aligned} (\mathbf{K}(1 + i\eta) - \omega^2 \mathbf{M}) \mathbf{u}(\omega) &= \mathbf{b}q(\omega), \\ y(\omega) &= \mathbf{c}^T \mathbf{u}(\omega), \end{aligned} \quad (3.3)$$

where \mathbf{u} denotes the state vector capturing the displacements and deformations of the entire structure. The input vector \mathbf{b} describes the spatial distribution and direction of the unit input force, and the output vector \mathbf{c} describes that of the observed unit displacement. The unit input vector is scaled with the input force q and the resulting output displacement is denoted y , both dependent on frequency ω . For a derivation is referred to any dynamics text book, such as Craig and Kurdila (2006).

We can write this into a complex frequency-dependent transfer function $G(j\omega)$, denoting the transmission between input force and output displacement,

$$\begin{aligned} G(j\omega) &= \frac{y(\omega)}{q(\omega)} = \mathbf{c}^T (\mathbf{K}(1 + i\eta) - \omega^2 \mathbf{M})^{-1} \mathbf{b} \\ &= \mathbf{c}^T \mathbf{Z}(\omega)^{-1} \mathbf{b}, \end{aligned} \quad (3.4)$$

with $\mathbf{Z}(\omega)$ the complex symmetric $N \times N$ frequency dependent dynamic stiffness matrix. The magnitude¹ of this function $|G(j\omega)|$ is used to obtain the amplification of harmonic amplitudes from input to output, possibly scaled to decibel, denoted as $|G(j\omega)|_{\text{dB}}$.

The undamped eigenfrequencies Ω_i and eigenvectors ϕ_i of the system can be calculated by solving the generalized eigenvalue problem

$$\mathbf{K}\phi_i = \Omega_i^2 \mathbf{M}\phi_i \quad \text{for } i = 1, \dots, n \quad (3.5)$$

for which the eigenfrequencies are ordered as $0 \leq \Omega_1 \leq \Omega_2 \leq \dots \leq \Omega_n$ for the n eigenfrequencies of interest. The eigenvectors $\Phi = [\phi_1, \phi_2, \dots, \phi_n]$ are mass-orthonormalized according to $\Phi^T \mathbf{M} \Phi = \mathbf{I}$. Since structural damping is used, the peak frequencies are equal to the undamped eigenfrequencies $\omega_i = \Omega_i$, at which the FRF amplitude $|G(\omega = \omega_i)|$ reaches its extreme values.

3.2.2 Optimization problem formulation

A general optimization problem involving resonance peak constraints can be formulated as

$$\begin{aligned} \min_{\mathbf{x}} \quad & f(\mathbf{x}) \\ \text{s.t.} \quad & |G(j\omega_j(\mathbf{x}), \mathbf{x})|_{\text{dB}} \leq g_{\text{upp}}(\omega_j(\mathbf{x})) \quad \forall \omega_j \in \mathcal{S}_{\text{upp}} \\ & |G(j\omega_k(\mathbf{x}), \mathbf{x})|_{\text{dB}} \geq g_{\text{low}}(\omega_k(\mathbf{x})) \quad \forall \omega_k \in \mathcal{S}_{\text{low}} \\ & x_{\min} \leq \mathbf{x} \leq 1 \end{aligned} \quad (3.6)$$

The proposed constraints can be used as either an upper limit or as a lower limit (Eq. 3.6) for the response at any peak frequency, provided these frequencies are known from eigenvalue calculation. Any peak frequency ($\omega_i \forall i \leq n$) can be placed in subsets \mathcal{S}_{upp} or \mathcal{S}_{low} , or both. Additionally, the formulation is not limited to one single upper and lower limit function (g_{upp} and g_{low}), e.g. the first resonance peak could be limited differently than the second. For robustness against mode switching, a mode tracking strategy (Kim and Kim, 2000) is advisable to ensure continuity of the constraints.

Any reasonable choice of objective function f is possible, but in this paper we will limit ourselves to an objective function in the form of a mean eigenvalue (Ma *et al.*, 1995). To maximize n eigenfrequencies, the harmonic mean of those frequencies is taken as objective

$$f(\mathbf{x}) = - \left(\sum_{i=1}^n \frac{1}{\Omega_i(\mathbf{x})^2} \right)^{-1}. \quad (3.7)$$

¹The notation $|\cdot|$ means to take the complex norm or magnitude of the value \bullet .

This objective function is relatively insensitive to mode switching, which otherwise could introduce discontinuities if not taken into account correctly (see *e.g.*, [Kim and Kim, 2000](#); [Du and Olhoff, 2007b](#)). In order not to obscure the scope of the paper, we choose to avoid using these techniques. Additionally, this objective helps preventing trivial solutions: in case n peaks corresponding to the n lowest frequencies are limited from above, a possible trivial solution would be to create n artificial rigid body modes (by means of disconnected parts or mechanisms), which have no effect on the point of interest and a very low transmission ratio, but do replace the lowest eigenfrequencies.

In order to prevent ill-conditioning of the system matrices, the lower bound on the design variables is set to x_{\min} . Secondly, a volume constraint is imposed to prevent trivial all-solid solutions. In total this leads to the following optimization problem which is considered throughout this paper:

$$\begin{aligned}
 \min_{\mathbf{x}} \quad & - \left(\sum_{i=1}^n \frac{1}{\Omega_i(\mathbf{x})^2} \right)^{-1} \\
 \text{s.t.} \quad & V(\mathbf{x}) \leq V_{\text{lim}} \\
 & |G(j\omega_j(\mathbf{x}), \mathbf{x})|_{\text{dB}} \leq g_{\text{upp}}(\omega_j(\mathbf{x})) \quad \forall \omega_j \in \mathcal{S}_{\text{upp}} \\
 & |G(j\omega_k(\mathbf{x}), \mathbf{x})|_{\text{dB}} \geq g_{\text{low}}(\omega_k(\mathbf{x})) \quad \forall \omega_k \in \mathcal{S}_{\text{low}} \\
 & x_{\min} \leq \mathbf{x} \leq 1
 \end{aligned} \tag{3.8}$$

For further use, we abbreviate the frequency response value at $G(j\omega_i)$ as G_i . In subsequent sections, three different methods are proposed to calculate the peak values $|G_i|$. All methods require the eigenpairs (Ω_i, ϕ_i) to be calculated beforehand.

3.2.3 Full method

The most straightforward method to calculate the FRF amplitudes at each required peak frequency, by solving the full linear system:

$$G_i = \mathbf{c}^T \mathbf{u}_i = \mathbf{c}^T \mathbf{Z}(\omega_i)^{-1} \mathbf{b} \quad \forall \omega_i \in \mathcal{S}_{\text{upp}} \cup \mathcal{S}_{\text{low}}. \tag{3.9}$$

The sensitivities of this function with respect to the filtered design variables are

$$\begin{aligned}
 \frac{dG_i}{d\rho_j} &= - \mathbf{c}^T \mathbf{Z}(\omega_i)^{-1} \frac{d\mathbf{Z}(\omega_i)}{d\rho_j} \mathbf{Z}(\omega_i)^{-1} \mathbf{b} \\
 &= - \xi_i^T \left(\frac{d\mathbf{K}}{d\rho_j} (1 + i\eta) - \omega_i^2 \frac{d\mathbf{M}}{d\rho_j} - 2\omega_i \mathbf{M} \frac{d\omega_i}{d\rho_j} \right) \mathbf{u}_i \\
 &= - \xi_i^T \mathbf{K}_{\text{el}}^{(j)} \mathbf{u}_i \frac{d\kappa_j}{d\rho_j} (1 + i\eta) + \omega_i^2 \xi_i^T \mathbf{M}_{\text{el}}^{(j)} \mathbf{u}_i \frac{d\mu_j}{d\rho_j} + 2\omega_i \xi_i^T \mathbf{M} \mathbf{u}_i \frac{d\omega_i}{d\rho_j},
 \end{aligned} \tag{3.10}$$

where \mathbf{u}_i is the state vector containing the solution of the harmonic response, and ξ_i the adjoint vector at each peak frequency ω_i . The last term in Eq. 3.10 adds the sensitivity information with respect to the peak frequency (and thus the eigenfrequency), which cannot be included in any method which iteratively finds the peak value in an FRF (such as [Venini](#)

and Pingaro, 2017). Both the state and adjoint require a full complex-valued system to be solved,

$$\mathbf{Z}(\omega_i)\mathbf{u}_i = \mathbf{b} \quad \text{and} \quad \mathbf{Z}(\omega_i)\boldsymbol{\xi}_i = \mathbf{c}, \quad (3.11)$$

where the state is only dependent on the input vector \mathbf{b} , and the adjoint depends on the output vector \mathbf{c} . Hence, the importance of the output location on the sensitivities is explained by the adjoint system having the output vector as a right-hand side. Note that these equations could be solved using one matrix factorization. In case an iterative solver is used, the systems would have to be solved separately if $\mathbf{b} \neq \mathbf{c}$.

To complete the sensitivity calculation, the derivatives of the interpolation functions (Eq. 3.1) are

$$\frac{d\kappa_j}{d\rho_j} = p(1-w)\rho_j^{p-1} + w \quad \text{and} \quad \frac{d\mu_j}{d\rho_j} = 1. \quad (3.12)$$

The peak frequency sensitivities are equal to the undamped eigenfrequency sensitivities in case of structural damping, and are calculated by

$$\frac{d\omega_i}{d\rho_j} = \frac{d\Omega_i}{d\rho_j} = \frac{1}{\Omega_i} \boldsymbol{\phi}_i^T \mathbf{K}_{\text{el}}^{(j)} \boldsymbol{\phi}_i \frac{d\kappa_j}{d\rho_j} - \Omega_i \boldsymbol{\phi}_i^T \mathbf{M}_{\text{el}}^{(j)} \boldsymbol{\phi}_i \frac{d\mu_j}{d\rho_j}, \quad (3.13)$$

which does not require the solution of any extra linear systems (a derivation is found in e.g., Haftka and Gürdal, 1992).

The peak responses of a damped dynamic system are complex values and so are their sensitivities. To obtain the magnitude of the frequency response, the complex norm is taken as²

$$|G_i| = \sqrt{G_i G_i^*} = \sqrt{\text{Re}(G_i)^2 + \text{Im}(G_i)^2}. \quad (3.14)$$

The sensitivity of the complex norm is calculated as

$$\frac{d|G_i|}{d\boldsymbol{\rho}} = \frac{1}{|G_i|} \left(\text{Re} \left(\frac{dG_i}{d\boldsymbol{\rho}} \right) \text{Re}(G_i) + \text{Im} \left(\frac{dG_i}{d\boldsymbol{\rho}} \right) \text{Im}(G_i) \right), \quad (3.15)$$

resulting in a real valued sensitivity. In case a transformation to decibel is used, the response and its sensitivity can be calculated as

$$|G_i|_{\text{dB}} = 20 \log_{10}(|G_i|) \quad \text{and} \quad \frac{d|G_i|_{\text{dB}}}{d|G_i|} = \frac{20}{|G_i| \log(10)}. \quad (3.16)$$

Finally, the sensitivities are treated with the density filter as described in the work of Bruns and Tortorelli (2001).

These last five differentiation operations in Eqs. 3.12-3.16 (material interpolation, eigenfrequency, complex norm derivatives, decibel transformation, and filter) are identical in the following methods using reduced-order models.

²The notation \bullet^* means the complex conjugate of \bullet .

3.2.4 Modal Truncation

In order to reduce the time spent in calculating all the required frequency response values, model reduction techniques can be used. Although it is very expensive to compute the eigenvectors, still the solution of the dynamic systems of equations will contribute significantly to the total computation time. The main reasons for this is twofold. First of all, the eigensolver only requires solution of real-valued matrices, while the resonance peaks involve a complex-valued matrix to be solved, which can be compared to a real-valued matrix of size $2N \times 2N$. Secondly, each peak requires an unique system of equations to be solved, while an eigensolver uses only one system of equations to iteratively converge towards the eigenpairs. When using a direct solver, this means that a factorization is required for each resonance peak in the optimization problem, while only one factorization is enough for the eigensolver. In case of an iterative solver, the same could be said about the preconditioner.

By using the eigenvectors which are already computed for the objective, modal truncation can be applied to obtain smaller ($n \ll N$) reduced system matrices $\tilde{\mathbf{K}}$ and $\tilde{\mathbf{M}} \in \mathbb{R}^{n \times n}$, and input-output vectors $\tilde{\mathbf{b}}$ and $\tilde{\mathbf{c}} \in \mathbb{R}^n$ (see, e.g., [Craig and Kurdila, 2006](#)). Thus, the higher modes of the system are truncated, as is assumed that these do not greatly affect the lower frequency spectrum. The reduced system is obtained by a Galerkin projection of the full system matrices on all the known eigenvectors Φ , as

$$\begin{aligned} \tilde{\mathbf{K}} &= \Phi^T \mathbf{K} \Phi = \text{diag}(\Omega_1^2, \Omega_2^2, \dots, \Omega_n^2), & \tilde{\mathbf{b}} &= \Phi^T \mathbf{b}, \\ \tilde{\mathbf{M}} &= \Phi^T \mathbf{M} \Phi = \mathbf{I}, & \tilde{\mathbf{c}} &= \Phi^T \mathbf{c}. \end{aligned} \quad (3.17)$$

Since the matrices are projected on the eigenvectors, the resulting system matrices are diagonal.

The diagonal terms of the reduced stiffness matrix become $\tilde{Z}_{kk}(\omega) = \Omega_k^2(1 + i\eta) - \omega^2$, which makes the response calculation very efficient using modal superposition. Again the frequency ω is chosen as peak frequency ω_i , resulting in the reduced response as³

$$\begin{aligned} G_i &\approx \tilde{G}_i^{\text{MT}} = \tilde{\mathbf{c}}^T \tilde{\mathbf{Z}}(\omega_i)^{-1} \tilde{\mathbf{b}} \\ &= \sum_{k=1}^n \frac{\mathbf{c}^T \phi_k \phi_k^T \mathbf{b}}{\Omega_k^2(1 + i\eta) - \omega_i^2} \quad \forall \omega_i \in \mathcal{S}_{\text{upp}} \cup \mathcal{S}_{\text{low}}. \end{aligned} \quad (3.18)$$

In order to calculate the sensitivities of this function, two approaches are proposed. The first one is the consistent calculation of sensitivities, and the second method is an approximation of the sensitivities by ignoring the design dependence of the reduction basis.

Consistent sensitivities

The sensitivities for the consistent method become more involved than the full model sensitivities, since a reduction step has been added. The sensitivities now have to be calculated

³The use of a reduced model is indicated by $\tilde{\cdot}$. The superscript indicates the type of model order reduction technique used: \cdot^{MT} for MT and \cdot^{MTA} for MTA)

using:

$$\frac{d\tilde{G}_i^{\text{MT}}}{dx_j} = \sum_{k=1}^n \frac{1}{\Omega_k^2(1+i\eta) - \omega_i^2} \frac{d\phi_k^T}{dx_j} (\mathbf{c}(\phi_k^T \mathbf{b}) + \mathbf{b}(\phi_k^T \mathbf{c})) - \frac{2\mathbf{c}^T \phi_k \phi_k^T \mathbf{b}}{(\Omega_k^2(1+i\eta) - \omega_i^2)^2} \left(\Omega_k(1+i\eta) \frac{d\Omega_k}{dx_j} - \omega_i \frac{d\omega_i}{dx_j} \right), \quad (3.19)$$

in which the adjoint eigenvector sensitivity of $\frac{d\phi_k^T}{dx_j}$ needs to be calculated. The term involving the eigenvector derivatives is the sensitivity with respect to the reducing basis. By solving the adjoint saddlepoint problem

$$\begin{bmatrix} \mathbf{K} - \Omega_k^2 \mathbf{M} & \mathbf{M} \phi_k \\ \phi_k^T \mathbf{M} & 0 \end{bmatrix} \begin{bmatrix} \mathbf{v}_k \\ \alpha_k \end{bmatrix} = \begin{bmatrix} -\mathbf{c}(\phi_k^T \mathbf{b}) - \mathbf{b}(\phi_k^T \mathbf{c}) \\ 0 \end{bmatrix}, \quad (3.20)$$

the adjoints \mathbf{v}_k and α_k can be calculated. For a detailed explanation the reader is referred to the work by Lee (1999, 2007).

After solving for adjoints, the eigenvector sensitivities can be obtained as

$$\frac{d\phi_k^T}{dx_i} (\mathbf{c}(\phi_k^T \mathbf{b}) + \mathbf{b}(\phi_k^T \mathbf{c})) = \frac{\alpha_k}{2} \phi_k^T \frac{d\mathbf{M}}{dx_i} \phi_k + \mathbf{v}_k \left(\frac{d\mathbf{K}}{dx_i} - \Omega_k^2 \frac{d\mathbf{M}}{dx_i} \right) \phi_k. \quad (3.21)$$

Note that for the calculation, a factorization of the matrix introduced in Eq. 3.20 is needed for each eigenvector in the base, or one iterative solution per eigenvector, for each peak to be observed. Instead of solving complex systems, now real-valued matrices can be used, which saves considerable computation time. Additionally, the number of linear systems to be solved is reduced by a factor of two in case the problem is not self-adjoint and an iterative solver is used.

Approximate sensitivities

From the exact sensitivities in Eq. 3.19, it can be seen that the first term is divided by the modal stiffness ($\tilde{Z}_{kk}(\omega_i) = \Omega_k^2(1+i\eta) - \omega_i^2$), and the second term is divided by the modal stiffness squared. The sensitivities are largest when the dynamic stiffness is very small ($\omega_i \approx \Omega_k$), causing the second term in Eq. 3.19 to become dominant, since it is squared. Therefore, in order to reduce computational effort, we propose to approximate the sensitivities by ignoring the first term containing eigenvector sensitivity terms with respect to input \mathbf{b} and output \mathbf{c} . Effectively, this means that the design dependency of the reduction basis in Eq. 3.17 is not considered and taken as constant, when taking the design sensitivities of Eq. 3.18. This results in

$$\begin{aligned} \frac{d\tilde{G}_i^{\text{MT}}}{dx_j} &\approx - \sum_{k=1}^n \frac{2\mathbf{c}^T \phi_k \phi_k^T \mathbf{b}}{(\Omega_k^2(1+i\eta) - \omega_i^2)^2} \left(\Omega_k(1+i\eta) \frac{d\Omega_k}{dx_j} - \omega_i \frac{d\omega_i}{dx_j} \right) \\ &= -\tilde{\mathbf{c}}^T \tilde{\mathbf{Z}}(\omega_i)^{-1} \Phi^T \frac{d\mathbf{Z}(\omega_i)}{dx_j} \Phi \tilde{\mathbf{Z}}(\omega_i)^{-1} \tilde{\mathbf{b}} \\ &= -\tilde{\xi}_i^T \Phi^T \frac{d\mathbf{Z}(\omega_i)}{dx_j} \Phi \tilde{\mathbf{u}}_i, \end{aligned} \quad (3.22)$$

where the reduced state and adjoint are now calculated using the reduced model by solving

$$\tilde{\mathbf{Z}}(\omega_i)\tilde{\mathbf{u}}_i = \tilde{\mathbf{b}} \quad \text{and} \quad \tilde{\mathbf{Z}}(\omega_i)^T\tilde{\boldsymbol{\xi}}_i = \tilde{\mathbf{c}}. \quad (3.23)$$

This method does not require any solution to the full linear system at all, but it may hamper convergence, because it is an approximation and information regarding the input and output is only contained via the eigenvector projection. This means that the sensitivities do not contain information anymore about the parts of \mathbf{b} and \mathbf{c} orthogonal to the eigenvectors in the basis, which was previously included in Eq. 3.21. In case the basis does not change with respect to the design (*i.e.* the eigenvectors do not change), these sensitivities are exact. Additionally, the above approximation makes implementation very easy, since the sensitivity of the approximated MT-based method (Eq. 3.22) strongly resembles the sensitivity of the full method Eq. 3.10, with the following substitutions:

$$\boldsymbol{\xi}_i \approx \Phi\tilde{\boldsymbol{\xi}}_i \quad \text{and} \quad \mathbf{u}_i \approx \Phi\tilde{\mathbf{u}}_i, \quad (3.24)$$

which are simply the projections of the approximated problem. For comparison, Table 3.1 shows an overview of the number of full system solutions required for the different methods.

Table 3.1: Comparison on the number of real and complex linear solutions required on the full system, depending on the number of peaks to be constrained n_p and the combined number of unique in- and outputs n_{io} . In case direct solvers are used, the number of matrix factorizations is equal to $n_{io} = 1$ and $n_p = 1$, except for consistent MTA, which requires $1 + n$ factorizations. All methods require the solution of n eigenvalues and eigenvectors of the full system.

Method	Consistent		Approximated		Use
	Real	Complex	Real	Complex	
Full	0	$n_{io} \cdot n_p$	N/A		A very small number of peaks
MT	$n \cdot n_p$	0	0	0	Many in- and outputs, many peaks
MTA	$n_{io} + (n + n_{io})n_p$	0	n_{io}	0	Few in- and outputs, many peaks

3.2.5 Modal Truncation Augmentation

MTA is an established concept of model reduction in the field of structural dynamics (Dickens *et al.*, 1997). By augmenting the reduction basis with extra correction vectors, the reduced model becomes more accurate. The correction vectors add localized information, which was lost by removing the high-frequency content in MT. By extending the basis with specific local information, not only the response becomes more accurate, but also the accuracy of sensitivities might be enhanced. Instead of only augmenting the solution to the input force \mathbf{b} , we choose also to add a correction with respect to output vector \mathbf{c} . Since the adjoint vector $\boldsymbol{\xi}$ is determined by solving the system using the output vector (Eq. 3.11), this should improve the approximated sensitivities. The reduction basis Φ is extended with undamped linear solutions \mathbf{v}_1 and \mathbf{v}_2 of the input and output vectors, at a shift frequency $\sigma < \Omega_1$,

$$\mathbf{v}_1 = (\mathbf{K} - \sigma^2\mathbf{M})^{-1} \mathbf{b}, \quad \mathbf{v}_2 = (\mathbf{K} - \sigma^2\mathbf{M})^{-1} \mathbf{c}, \quad (3.25)$$

to obtain the augmented reducing basis

$$\mathbf{V} = \text{span}\{\Phi, \mathbf{v}_1, \mathbf{v}_2\} \quad \text{s.t.} \quad \mathbf{V}^T \mathbf{M} \mathbf{V} = \mathbf{I}. \quad (3.26)$$

Note that for a collocated system ($\mathbf{b} \propto \mathbf{c}$), only one vector needs to be added as both vectors would be linearly dependent. In case of MIMO systems, it is trivial to add more vectors for all distinct inputs and outputs (Dickens *et al.*, 1997).

The augmentation vectors are orthonormalized with respect to the other vectors, by solving a small eigenvalue problem to diagonalize the matrix

$$\Psi^T \mathbf{M} \Psi = \mathbf{Q} \mathbf{\Lambda} \mathbf{Q}^T \quad \text{with} \quad \mathbf{Q}^T \mathbf{Q} = \mathbf{I}, \quad (3.27)$$

where $\Psi = [\Phi \quad \mathbf{v}_1 \quad \mathbf{v}_2]$, \mathbf{Q} is an orthogonal matrix containing the eigenvectors, and $\mathbf{\Lambda}$ a diagonal matrix with the eigenvalues of the un-orthogonalized projected mass matrix. Using these, we can obtain a linear combination to get the orthonormal system

$$\mathbf{\Lambda}^{-\frac{1}{2}} \mathbf{Q}^T \Psi^T \mathbf{M} \Psi \mathbf{Q} \mathbf{\Lambda}^{-\frac{1}{2}} = \mathbf{V}^T \mathbf{M} \mathbf{V} = \mathbf{I}. \quad (3.28)$$

The reducing basis thus becomes

$$\mathbf{V} = \Psi \mathbf{Q} \mathbf{\Lambda}^{-\frac{1}{2}} \quad \text{or} \quad \mathbf{V}_j = \sum_k \Psi_k \frac{Q_{kj}}{\sqrt{\Lambda_{jj}}} \quad (3.29)$$

and the reduced model can be obtained as

$$\begin{aligned} \tilde{\mathbf{K}} &= \mathbf{V}^T \mathbf{K} \mathbf{V}, & \tilde{\mathbf{M}} &= \mathbf{V}^T \mathbf{M} \mathbf{V} = \mathbf{I}, \\ \tilde{\mathbf{b}} &= \mathbf{V}^T \mathbf{b}, & \tilde{\mathbf{c}} &= \mathbf{V}^T \mathbf{c}. \end{aligned} \quad (3.30)$$

Note that the reduced stiffness matrix $\tilde{\mathbf{K}}$ now is not diagonal anymore. Therefore, we write the dynamic stiffness matrix as $\tilde{\mathbf{Z}}(\omega) = \tilde{\mathbf{K}}(1 + i\eta) - \omega^2 \tilde{\mathbf{M}}$. The peak values can be calculated using

$$G_i \approx \tilde{G}_i^{\text{MTA}} = \tilde{\mathbf{c}}^T \tilde{\mathbf{Z}}(\omega_i)^{-1} \tilde{\mathbf{b}} \quad \forall \omega_i \in \mathcal{D}_{\text{upp}} \cup \mathcal{D}_{\text{low}}. \quad (3.31)$$

It is possible to calculate consistent sensitivities of this reduced model, however, it involves a lengthy derivation which is omitted here for the sake of compactness, and can be found in the journal publication of this chapter (Delissen *et al.*, 2020). In contrast, the approximated sensitivities where we neglect the design-dependence of all base vectors, are just as straightforward to derive as with the MT method. They can be calculated using

$$\begin{aligned} \frac{d\tilde{G}_i^{\text{MTA}}}{dx_j} &\approx -\tilde{\mathbf{c}}^T \tilde{\mathbf{Z}}(\omega_i)^{-1} \mathbf{V}^T \frac{d\mathbf{Z}(\omega_i)}{dx_j} \mathbf{V} \tilde{\mathbf{Z}}(\omega_i)^{-1} \tilde{\mathbf{b}} \\ &= -\tilde{\xi}_i^T \mathbf{V}^T \frac{d\mathbf{Z}(\omega_i)}{dx_j} \mathbf{V} \tilde{\mathbf{u}}_i, \end{aligned} \quad (3.32)$$

which is merely a change of basis as compared to the approximated sensitivities of the MT method (Eq. 3.22). The reduced linear system now involve a matrix of size $(n+2) \times (n+2)$:

$$\tilde{\mathbf{Z}}(\omega_i) \tilde{\mathbf{u}}_i = \tilde{\mathbf{b}} \quad \text{and} \quad \tilde{\mathbf{Z}}(\omega_i)^T \tilde{\xi}_i = \tilde{\mathbf{c}}. \quad (3.33)$$

This last method is not as inexpensive as the approximated sensitivity MT method, due to the additional solutions required to augment the basis, but also not as expensive as the full method or the consistent sensitivity MT method (an overview is given in Table 3.1). It only requires one extra matrix factorization, or one iterative linear solution per unique input and output. Since we only consider the SISO case, only one solution (collocated system) or two solutions (non-collocated system) are required. But in case of MIMO, each unique in- and output vector of interest would have to be augmented, each requiring a linear solution (Dickens *et al.*, 1997).

3.3 Results

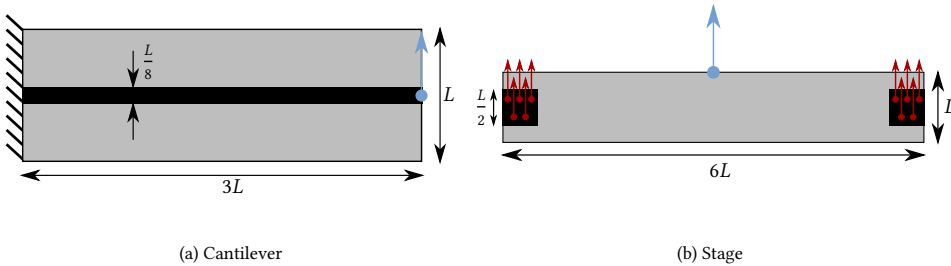


Figure 3.2: a) The cantilever problem with collocated input and output at the tip, and b) the stage problem with non-collocated input at the sides and output at the top middle.

Two test cases are used to study the optimization process, and the influence of various model reductions. First of all, a cantilever problem (Fig. 3.2a), with a solid non-design region in the middle of the domain, and a collocated input and output. Secondly, a free floating stage (Fig. 3.2b) is used, with non-collocated input and output, where the input is distributed along two square non-design domains which represent actuators. The output location is in the center of the top surface. Since the structure is free-floating, it exhibits three rigid body modes. For the MTA approach, this means that the augmentation vectors cannot be static ($\sigma = 0$). Instead a quasi-static solution is obtained at $\sigma = 50$ rad/s, which is well below the first eigenfrequency and will be used for both test cases. The objective involves $n = 3$ structural eigenvalues, which are also limited in amplitude ($n_p = 3$). For simplicity, no mode tracking is applied in all examples. Further parameters used for the optimization are listed in Table 3.2.

The optimization problem is solved using MMA (Svanberg, 1987), of which the number of iterations are limited to a maximum of 200. All the results presented converged to a stationary solution, unless otherwise mentioned. Furthermore, the objective function is scaled to be -100 in the first iteration and the volume constraint is scaled by a factor 10.

First, optimization results of the different peak constraint implementations with the consistent approach are given in Section 3.3.1. After that, in Section 3.3.2 a comparison is made between consistent and approximate sensitivities. Finally, optimizations using approximate sensitivity information are shown in Section 3.3.3.

Table 3.2: Physical properties and variables used in the optimization problems.

Parameter	Description	Value
L	Length scale	1 m
t	Thickness	0.1 m
E	Young's modulus	1 MPa
ν	Poisson's ratio	0.3
ρ	Density	1 kg/m ³
η	Hysteretic damping	10 ⁻³
x_{\min}	Minimum design value	10 ⁻³
n	Number of eigenvalues calculated	3
r	Filter radius	2 Elements
w	Interpolation ratio	0.1
p	Interpolation power	3
V_{\lim}	Volume fraction	0.5
σ	Frequency shift for MTA	50 rad/s
	Cantilever mesh	240 × 80
	Stage case mesh	240 × 40

3.3.1 Consistent Optimization

To show the operation of the proposed peak constraint, the test cases are optimized using the full method and the two reduced-order models using consistent sensitivities. For reference, the results of an unconstrained optimization (i.e. only constrained in volume) are also shown.

Cantilever

The cantilever problem is constrained with an upper limit of $g_{\text{upp}} = -1$ dB for the first three peak amplitudes. This value is arbitrarily chosen here: it is physically achievable, and this limit will cause the constraint to be active. In practice the designer would provide a limit based on operational targets. Using the method involving full system solutions for optimization (Section 3.2.3), we obtain the design shown in Fig. 3.3b. The reference design of an optimization without any peak constraints is shown in Fig. 3.3a.

An overview of the performance values is given in Table 3.3 and FRFs of the designs are shown in Fig. 3.4. From these can be seen that the peaks are indeed limited with $g_{\text{upp}} = -1$ dB. The lower peak values come at a cost, because the first two eigenfrequencies are significantly lower than in the design without peak constraints. This is reflected in the higher objective function, in which the lowest eigenfrequencies contribute most. When looking at the mode shapes in Fig. 3.5, it is evident that they are different from the reference case. At the left side of the constrained design a mechanism can be recognized, which rotates the right part of the structure such that the tip displacements are reduced.

As for the results involving reduced-order models (Sections 3.2.4-3.2.5), the final designs of the MT and MTA method are respectively shown in Fig. 3.3c and Fig. 3.3d. These

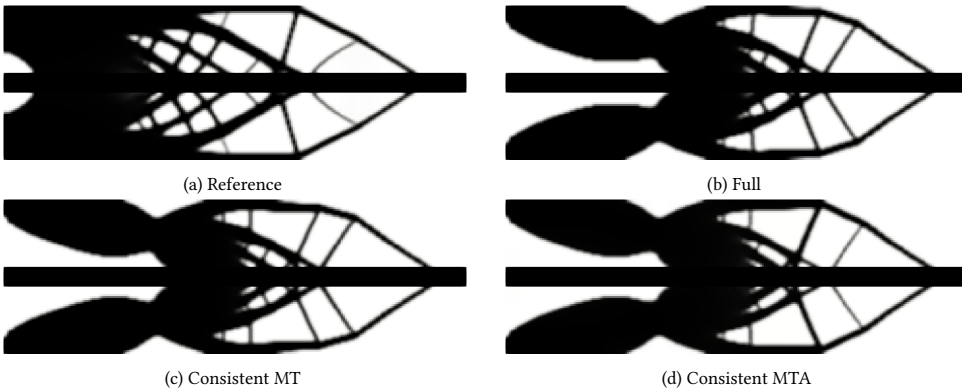


Figure 3.3: Resulting cantilever designs of the mean eigenvalue maximization without peak constraint (a) and with peak constraint, solved by the full method (b). The results of using reduced models with consistent sensitivities are shown for MT (c) and for MTA (d).

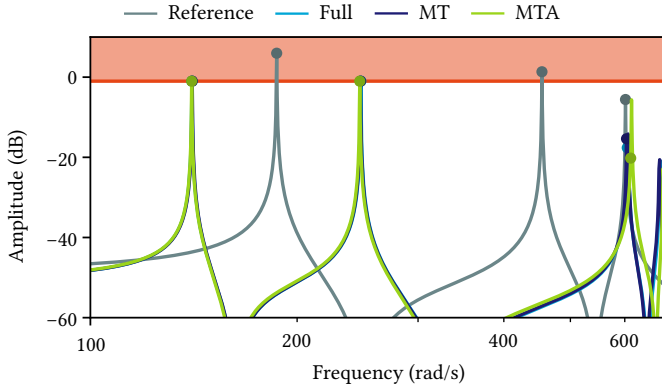


Figure 3.4: FRFs of the different cantilever designs.

designs are hard to distinguish from the design obtained using the full method (Fig. 3.3b), and their performance is equivalent (Table 3.3). Looking at the convergence history of the cantilever optimization, as shown in Fig. 3.8a, it can clearly be seen that the three methods have similar convergence. In our Python implementation, using matrix factorizations whenever possible, solving the required eigenvectors takes about 13 s, one real-valued factorization 0.85 s, and a complex factorization 2.5 s. This means that factorizing three complex matrices, required for the full method, represent a significant portion (about a third) of the computational time. Using the reduced-order models, only 3 real factorizations for MT or 4 for MTA have to be made, hence the time saved per iteration (Table 3.3). In case of iterative solvers, this computational gain is more debatable, as the adjoints cannot be calculated with simple back-substitutions anymore and separate iterative solutions are needed.

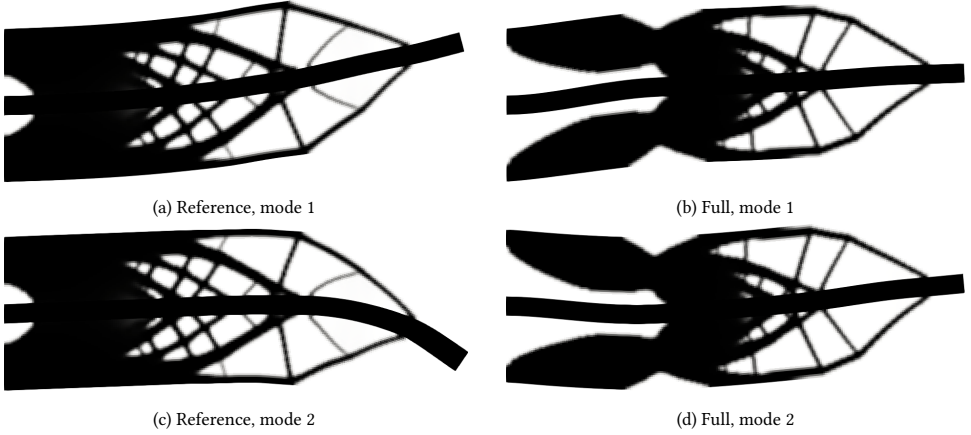


Figure 3.5: The first two eigenmodes of the optimized structure for optimization without peak constraint (a and c). First two eigenmodes of the constrained optimization using the full method with $g_{\text{upp}} = -1$ dB (b and d).

Table 3.3: Comparison of final performance values for the cantilever case, using $g_{\text{upp}} = -1$ dB. The number of inputs and outputs $n_{\text{io}} = 1$ and $n_p = 3$. Evaluated on the full model.

		Ref.	Full	MT	MTA
Objective	rad^2/s^2	-822.2	-428.2	-428.5	-427.8
Volume	-	0.500	0.500	0.500	0.500
Ω_1	rad/s	186.8	140.6	140.7	140.4
Ω_2	rad/s	454.5	247.6	247.3	246.8
Ω_3	rad/s	601.5	605.1	603.5	612.0
$ G_1 _{\text{dB}}$	dB	5.970	-1.000	-1.001	-1.001
$ G_2 _{\text{dB}}$	dB	1.343	-1.001	-1.002	-1.002
$ G_3 _{\text{dB}}$	dB	-5.580	-17.62	-15.37	-20.20
No. factorizations per iteration		-	3 Complex	3 Real	4 Real
Time / iter.	s	14.2	22.2	16.8	18.9

Although beyond the scope of this work, it should be noted that model order reduction with consistent sensitivities could become more viable using aggregation strategies. Aggregation already has been implemented successfully for instance in stress constraints (Yang and Chen, 1996) to reduce computational time for the sensitivity calculation, and in eigenvalue optimization (Torii and de Faria, 2017) to overcome differentiability issues. In our case, for the full solution strategy, each peak constraint is dependent on a different $Z(\omega_j)$, which requires an adjoint to be solved for each of the peaks. When a reduced-order model is used, the adjoints would not be expensive, as they are evaluated on the reduced model $\tilde{Z}(\omega_j)$. The expensive adjoint solutions (in this case the model reduction basis sen-

sivities) are involving identical system matrices for each peak constraint, allowing the expensive sensitivities only to be calculated once when aggregating. This effectively results in only n linear solutions on the full system for MT and $2n_{io} + n$ linear solutions for MTA, independent of the number of peaks considered, compared to the full method, still requiring the solution of $2n_p$ full complex linear systems if the constraints would be aggregated. In Table 3.1 the resulting number of solutions on the full system for an aggregated constraint could be seen as $n_p = 1$ for MT and MTA, but not for the full method.

Stage

The second example involves the optimization of a free-floating stage (Fig. 3.2b). In comparison with the cantilever case, this example has a non-collocated input and output vector. Additionally, there are rigid body modes present in this example, which means that the peaks of the 4th, 5th, and 6th eigenmode (the first three flexible modes) are constrained. We choose the constraint limit as $g_{upp} = -25$ dB.

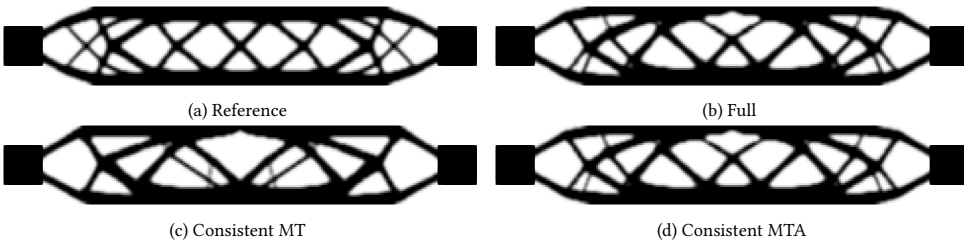


Figure 3.6: Resulting stage designs of the mean eigenvalue maximization for (a) without peak constraint and (b) with peak constraint, solved by the full method. Results of using reduced models with consistent sensitivities are shown for MT (c) and MTA (d).

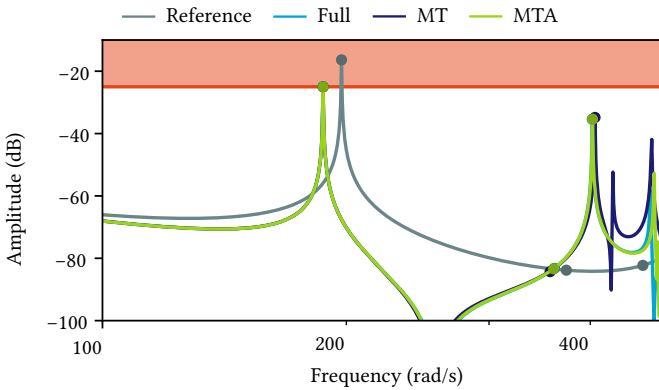
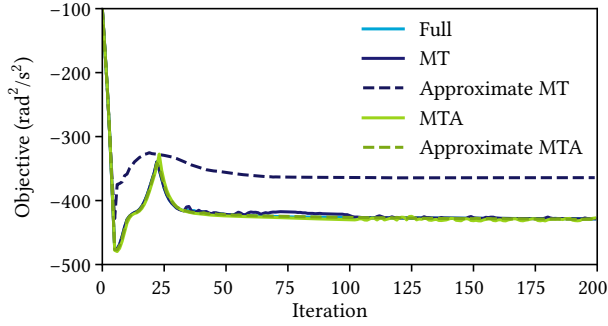


Figure 3.7: FRFs of the different stage designs.

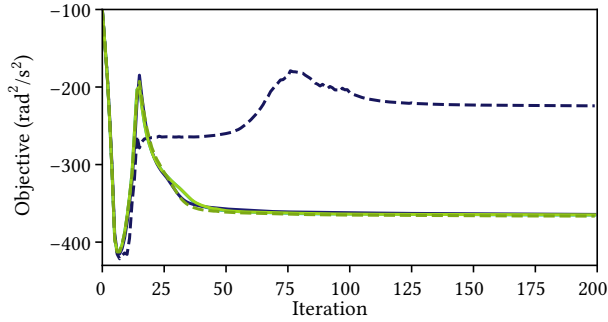
The resulting design of the optimization without peak constraint (Fig. 3.6a) and the constrained designs (Figs. 3.6b-3.6d) again show a trade-off between peak limitation and eigenfrequency values (Table 3.4). The peak limits are attained at cost of lower eigenfrequencies.

Table 3.4: Comparison of values for the stage case, using $g_{\text{supp}} = -25$ dB. Evaluated on the full model.

		Ref.	Full	MT	MTA
Objective	rad^2/s^2	-412.6	-365.0	-364.3	-364.9
Volume	-	0.500	0.500	0.500	0.500
Ω_1	rad/s	197.3	187.2	187.2	187.2
Ω_2	rad/s	373.8	361.3	356.9	360.5
Ω_3	rad/s	464.6	402.4	405.5	402.6
$ G_1 _{\text{dB}}$	dB	-16.36	-25.00	-25.00	-25.00
$ G_2 _{\text{dB}}$	dB	-83.82	-83.23	-84.29	-83.39
$ G_3 _{\text{dB}}$	dB	-82.28	-35.39	-34.82	-35.40
No. factorizations per iteration		-	3 Complex	3 Real	5 Real



(a) Cantilever



(b) Stage

Figure 3.8: Iteration history of the objective for a) the cantilever case and b) the stage case. The cantilever optimizations become feasible at iteration 25, except for approximate MT, which does not reach a feasible design within 200 iterations. For the stage, feasibility is reached at iteration 15 for all methods, except for approximate MT which only becomes feasible at iteration 82.

Between the designs resulting from the full method (Fig. 3.6b) and the consistent MTA (Fig. 3.6d), the difference in design is hardly recognizable. The design resulting from consistent MT (Fig. 3.6c) is different although its performance is equivalent to the other designs (Table 3.4 and Fig. 3.7), indicating a different local optimum. Also here, when looking at the convergence history in Fig. 3.8b, the use of reduced-order models with consistent sensitivities does not hamper optimization convergence and the convergence is very similar.

3.3.2 Comparison of consistent and approximate sensitivities

As already observed in previous section, the use of consistent sensitivities in optimization with reduced models yields comparable results to using a full model. However, using reduced-order models with consistent sensitivities in the previous examples results only marginally increased computational efficiency compared to the full method. Therefore, we investigate the effect of approximating the sensitivities of the reduced-order models, by ignoring the design dependency of the model reduction basis.

The effect of neglecting the reduction basis sensitivities, therefore not requiring any expensive solution of the adjoint problem, is visually demonstrated in Fig. 3.9. This figure shows the sensitivities of the first two peak constraints of the stage case in the first design iteration, thus consisting of a uniform density field. It is clear that the localized details around the output location (Figs. 3.9a and 3.9b) are not present in the approximate sensitivities (Figs. 3.9c and 3.9d). Identical observations could be made for the third peak constraint, not shown here. The local features are present again in the approximate sensitivities of the MTA method (Figs. 3.9e and 3.9f), where the additional vectors provide this information.

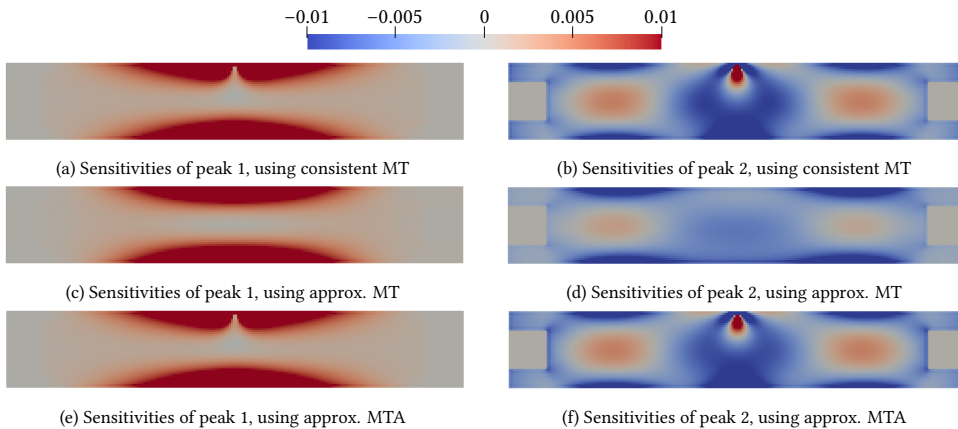


Figure 3.9: The exact sensitivities (a), and the approximate sensitivities using MT (c), of the first peak. Consistent and approximate sensitivities of the second peak respectively (b) and (d). The approximate sensitivities of the first two peaks using MTA are shown in (e) and (f).

To quantify the error between approximate and consistent sensitivity fields, we introduce a sensitivity error norm as

$$\epsilon_i = \frac{\sum_j \left| \frac{d|\tilde{G}_i|_{dB}}{dx_j} - \frac{d|\tilde{G}_i|_{dB}}{dx_j} \text{ approx} \right|}{\sum_j \left| \frac{d|\tilde{G}_i|_{dB}}{dx_j} \right|}. \quad (3.34)$$

3

Again, the sensitivities are evaluated in the first design iteration for both the test cases. In Table 3.5, the error values are reported for both the cantilever and the stage case. Two observations can be made from these values. First of all, the sensitivity error is much lower for the MTA sensitivities than for the MT. Second, the sensitivity errors for the peak constraints go up for higher eigenfrequencies when using MTA. This might be related to the choice of shift frequency σ (chosen below the first eigenvalue) to evaluate the augmented response.

Table 3.5: Comparison of sensitivity error values for the cases in the first iteration. Error norm of the approximate sensitivities with respect to the consistent sensitivities.

	Cantilever		Stage	
	MT	MTA	MT	MTA
ϵ_1	0.0619	0.000 129	0.150	0.001 47
ϵ_2	0.532	0.0789	0.330	0.072
ϵ_3	0.506	0.215	0.290	0.244

3.3.3 Optimization with approximate sensitivities

The effect on the optimization process when approximating the reduced-order model sensitivities, is demonstrated in this section. Designs and performance are compared between the consistent and approximate approaches.

Cantilever

Starting again with the cantilever case, the results of optimization with approximate sensitivities are shown in Fig. 3.10b and Fig. 3.10c for respectively MT and MTA. Especially the design optimized with approximate MTA is very similar to the consistent design (Fig. 3.10a). This can also be seen from the performance values in Table 3.6. The objective and eigenfrequencies of the consistent design and the approximated MTA design are very similar. However, the optimization with approximated MT did not even converge, as a feasible design was not reached (volume constraint violation). This can also be seen in the iteration history (Fig. 3.8a), which shows that the approximate MTA follows a similar path compared to the consistent methods, while the approximate MT completely different path as the optimization progresses.

The introduced sensitivity approximations achieve further computational gain. The timings in Table 3.6 show that the approximate MT method requires virtually no extra

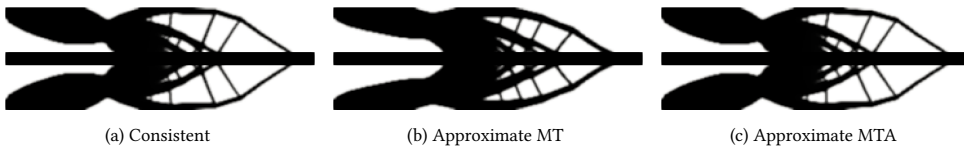


Figure 3.10: Results of the cantilever mean eigenvalue maximization with peak constraint (a), solved by the full method. The results of using reduced models with approximated sensitivities are shown for MT (c) and for MTA (d).

time to calculate the peaks and their sensitivities, compared to the reference case without peak constraints (Table 3.3). The approximate MTA method saves about a quarter of total computation time, which means that the time required to calculate the peak values and their sensitivities is shortened almost an order of magnitude (8 s for the full method versus 1.2 s for approximate MTA). When using iterative solvers, the computational gain might even be larger, since no iterative solutions are required for the sensitivities.

Table 3.6: Comparison between consistent and approximated sensitivities of final performance values for the cantilever case.

		Consistent		
		Approximated		
		Full, MT, MTA	MT	MTA
Objective	rad^2/s^2	-428.2	-364.4	-429.3
Volume	-	0.500	0.517	0.500
Ω_1	rad/s	140.6	122.9	140.8
Ω_2	rad/s	247.6	277.2	247.7
Ω_3	rad/s	605.1	597.3	604.9
$ G_1 _{\text{dB}}$	dB	-1.000	-0.999	-1.000
$ G_2 _{\text{dB}}$	dB	-1.001	-1.002	-1.002
$ G_3 _{\text{dB}}$	dB	-17.62	-42.51	-13.06
No. real factorizations		0, 3, 4	0	1
No. complex factorizations		3, 0, 0	0	0
Time / iter.	s	17-22	14.5	15.4

Stage

The optimization results of the stage case are shown in Figs. 3.11b and 3.11c for the MT and MTA methods using approximate sensitivities. For comparison, the design obtained from the consistent optimization (Fig. 3.11a) is also shown. Again, the design resulting from approximate MT is clearly distinct from the other designs. In contrast to the cantilever, the resulting MT stage design is feasible, although it took 82 iterations instead of 15, which the other methods required. Again, the convergence of the approximate MTA is very similar to the other methods (Fig. 3.8b), while the approximate MT method causes a completely different convergence path and a worse optimum.

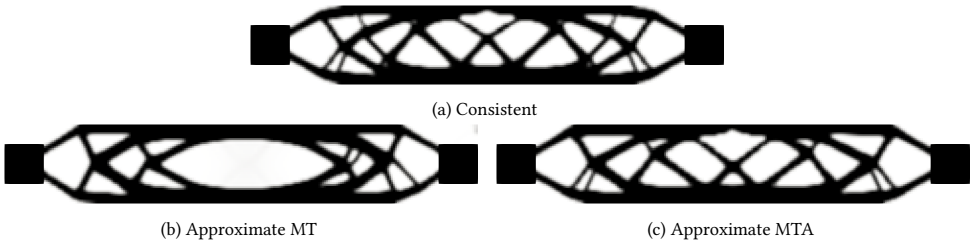


Figure 3.11: Results of the stage of mean eigenvalue maximization with peak constraint (a), solved by the full method. The methods using approximated sensitivities produce results MT (b) and MTA (c).

Table 3.7: Comparison between consistent and approximated sensitivities of final performance values for the stage case.

		Consistent	Approximated	
		Full, MT, MTA	MT	MTA
Objective	rad^2/s^2	-365.0	-224.2	-366.5
Volume	-	0.500	0.500	0.500
Ω_1	rad/s	187.2	202.6	187.2
Ω_2	rad/s	361.3	205.1	363.9
Ω_3	rad/s	402.4	219.0	404.4
$ G_1 _{\text{dB}}$	dB	-25.00	-25.00	-25.00
$ G_2 _{\text{dB}}$	dB	-83.23	-25.00	-83.13
$ G_3 _{\text{dB}}$	dB	-35.39	-29.36	-35.47
No. real factorizations		0, 3, 5	0	2
No. complex factorizations		3, 0, 0	0	0

3.3.4 Case variations

In this section, variations of the limit function are explored to gain more insight into the behavior and possibilities of the proposed constraint. Both the full and approximate MTA methods are used for the optimizations.

To illustrate the individual control of peaks in the FRF, the first variation is to choose a lower limit instead of an upper limit on the cantilever case. For the first peak we now use $|G_1|_{\text{dB}} \geq 10$ dB. The other two peak constraints are kept on their original upper limit of $g_{\text{upp}} = -1$ dB. The resulting designs and FRF are shown in Fig. 3.12, from which can be seen that the requirements are fulfilled. Although the design optimized with approximate MTA is asymmetric, it performs a little better (higher eigenvalues) than the design optimized with the full method. The bulk of the material is distributed in the same manner for both designs, with the main difference the slender structure being removed at the top part for the approximate MTA design.

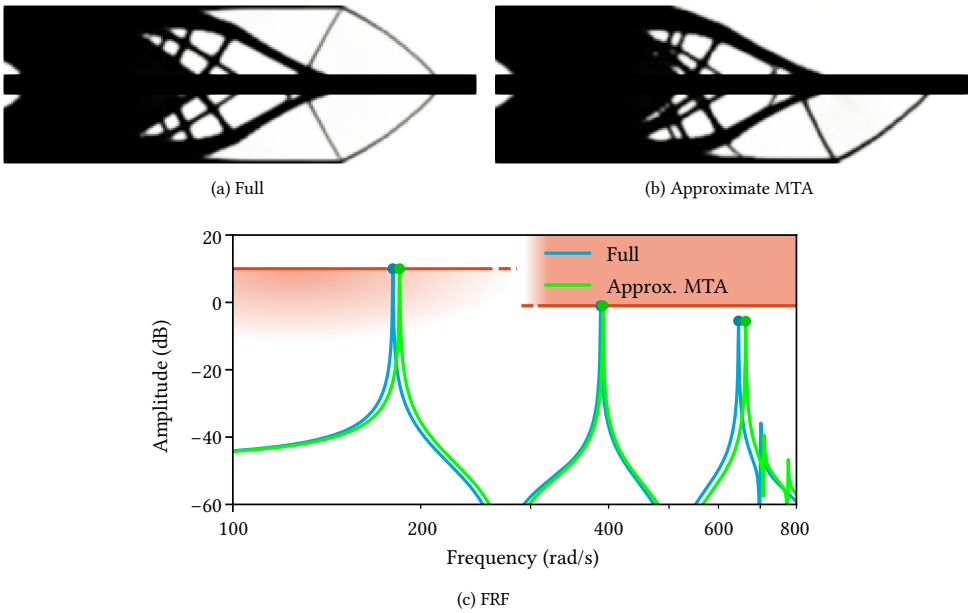


Figure 3.12: Results of choosing a lower limit for the first peak $|G_1|_{dB} \geq 10$ dB. The design from the full method (a) and the approximate MTA method (b) and their FRF (c).

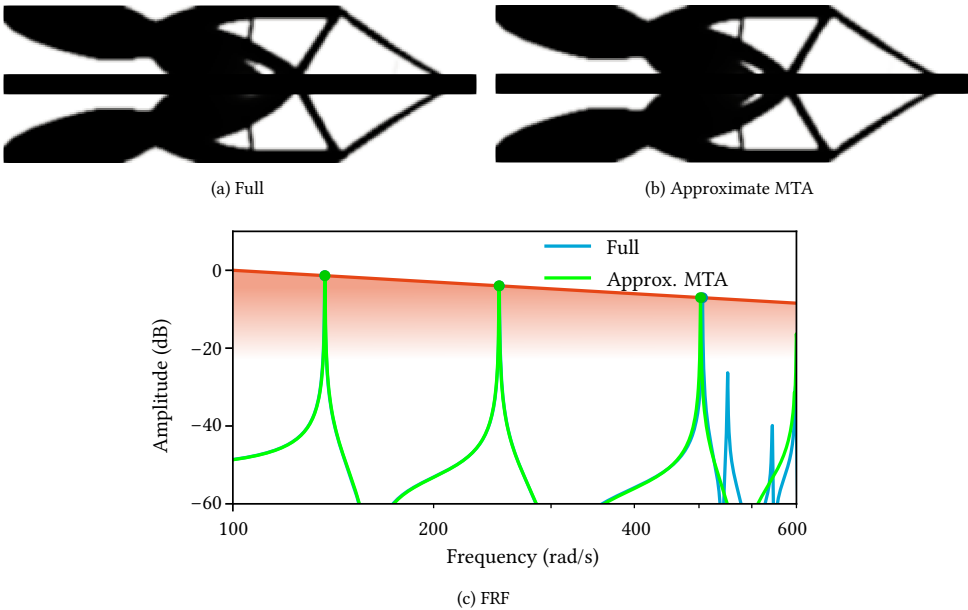


Figure 3.13: Result of choosing the frequency-dependent lower limit for all peaks as Eq. 3.35. The design from the full method (a) and the approximate MTA method (b) and their FRF (c)

Also non-constant limit functions can be used, which is demonstrated using the lower limit

$$g_{\text{low}}(\omega) = -10 \log(\omega) + 20. \quad (3.35)$$

With a logarithmic frequency axis, it represents a sloped straight line in an FRF. Any other user-defined peak envelope function can also be used for the constraint. Note that the sensitivity of this function also needs to be taken into account as this is a function of frequency. The resulting designs are feasible and all three constraints are active, as is shown in Fig. 3.13. Both optimized designs are very similar to each other, with nearly identical dynamic behavior.

Next to a frequency-dependent constraint limit, another possibility is an adaptive limit. Instead of maximizing the eigenfrequencies, the maximum peak can be minimized. Practical implementation of this min-max problem can be done using a bound formulation, which results in the following optimization problem:

$$\begin{aligned} \min_{\mathbf{x}, \beta} \quad & \beta \\ \text{s.t.} \quad & V(\mathbf{x}) \leq V_{\text{lim}} \\ & \left| G(j\omega_j(\mathbf{x}), \mathbf{x}) \right|_{\text{dB}} \leq \beta \quad \forall \omega_j \in \mathcal{S}_{\text{upp}} \\ & x_{\text{min}} \leq \mathbf{x} \leq 1 \\ & -80 \leq \beta \leq 20 \end{aligned} \quad (3.36)$$

The results of this optimization problem are shown in Fig. 3.14. The obtained designs feature appendages near the tip, that are weakly connected to the main structure. These appendages add low-frequency modes to the structure, that do not result in a large amplitude at the output point. This is advantageous in this example because the response of only the three lowest peaks is limited. It is clear that the optimizer exploits not having a penalization on low eigenfrequencies, by adding these artificial low-frequency modes in the process. This demonstrates the need for additional requirements on the optimization problem in order to obtain a meaningful design.

In practice, operational conditions might impose other requirements on the FRF. For example, in equipment operating at a constant frequency, a low response amplitude at exactly that frequency is desired. This can be achieved by extending the optimization problem in Eq. 3.36 with the constraint $\left| G(j\omega_{\text{op}}, \mathbf{x}) \right|_{\text{dB}} \leq -80$, where ω_{op} is the operational frequency, chosen as 300 rad/s, initially just in between de second and third natural frequency. Note that extra bounds on the FRF can be set without adding any computational expense when using approximate MTA.

The results of the optimization with this extra constraint can be seen in Fig. 3.15. The full design satisfies the operating frequency constraint with a value of -80.01 dB at ω_{op} , whereas the design optimized with approximate MTA is just infeasible with a value of -79.87 dB evaluated on the full model, while it is feasible on the reduced model. This might be explained by the loss of accuracy when using reduced-order models. Especially when the response is close to zero, a small absolute error might introduce a large error in the decibel scale. For the full design, the optimum design is found with $\beta = -2.00$ dB, while for the approximate MTA design $\beta = -2.40$ dB.

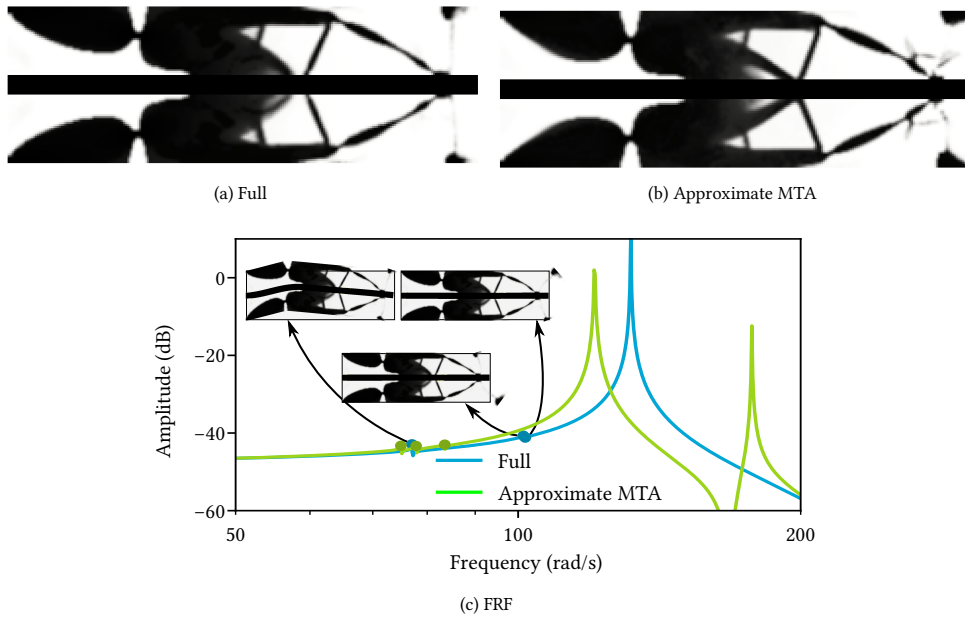


Figure 3.14: Results of a maximum peak minimization as in Eq. 3.36 (a and b) and their corresponding FRF (c), where the first three eigenmodes of the full design are shown as insets.

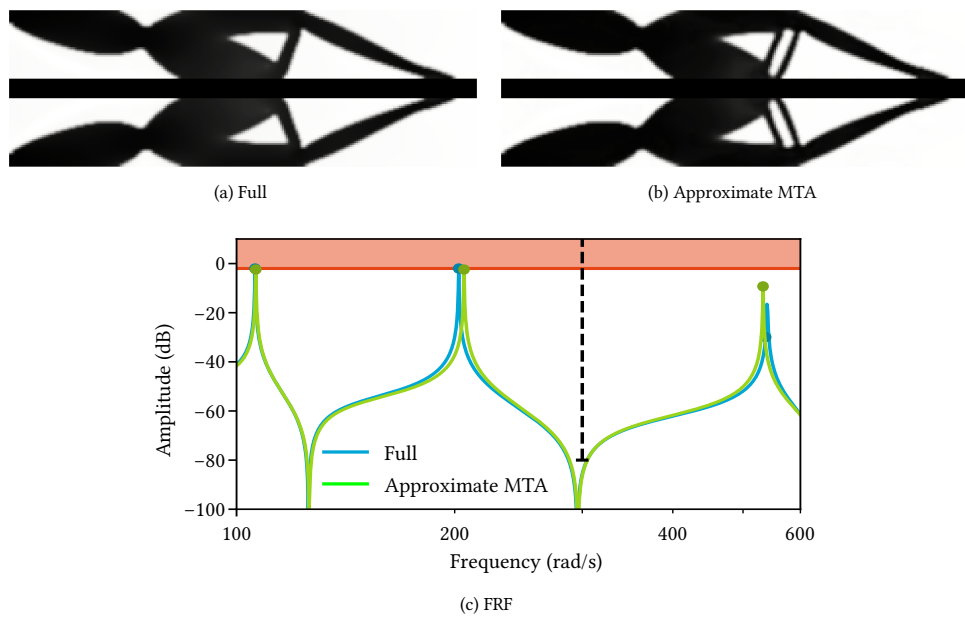


Figure 3.15: Results a maximum peak minimization subject to an additional maximum amplitude constraint at 300 rad/s (a and b) and their corresponding FRF (c).

3.4 Conclusions

In this chapter, we proposed a constraint to limit peak frequency response amplitudes. It is able to effectively and efficiently limit peak values of an FRF. By using the eigenvalues and eigenvectors of interest, versatile upper and lower limits can freely be selected per resonance peak.

Various ways to reduce the computational effort have been explored using three different implementations of this constraint, one based on solving the full system, and two involving reduced-order models (modal truncation (MT) and modal truncation augmentation (MTA)). It has been shown that by using consistent sensitivities, thus by including sensitivities of the reduction base vectors, the optimization converges to nearly identical designs with equal performance. In this case, no complex linear systems need solving anymore, but a larger number of real-valued linear solutions are required.

The sensitivities of the reduced models can be approximated by ignoring the design dependence with respect to the model reduction basis. Only having eigenmodes in the basis (MT) leads to inferior convergence during optimization and infeasible design. It is shown that the approximation in case of MT fails to reveal local details in the sensitivity field, since higher-frequency eigenmodes are truncated. By augmenting the basis with correction vectors (MTA), important local details, which were previously truncated, are resolved in the sensitivities and results similar to the consistent optimization are obtained. Sensitivity approximation has two advantages, the first being implementation ease. The sensitivities directly use the projected reduced solution for evaluation, thus easy to implement in code which already uses sensitivities based on the full model. Secondly, fewer real-valued linear solutions are required as the number is not dependent on the number of peaks anymore, but dependent on the number of augmented vectors. In examples shown, the time required to calculate the peaks and the associated sensitivities can be reduced by almost an order magnitude when using the proposed techniques, with a possibility of even further time reduction when iterative solvers are used.

Looking forward, an interesting research direction is the aggregation of peaks. Combining reduced models with aggregation of the resonant peaks, the number of full solutions can be reduced, which is not possible using the full method. Theoretically, the number of linear solutions could be independent of the number of peaks, while still using consistent sensitivities. This is especially interesting in cases where many peaks are constrained, or when many inputs and outputs are present (MIMO), making both directly evaluating the full system and the MTA method computationally expensive. In this case MT consistent optimization might be very suitable.

It needs to be noted that, depending on application demands, the damping model requires improvement for more accurate results. In order to improve accuracy, it is recommended to consider modal damping or even Voigt/Maxwell-type models, depending on the constituent material. Related to this, an interesting research direction is multi-material design in a peak limitation context, where multiple materials with different damping properties can be placed (see, e.g., [Van der Kolk et al., 2017](#)). In this manner, the amplitude of a peak can be changed both by changing the eigenmodes (as in the current work) and by effective placement of material with different damping properties.

4

Integrated optimization in the Nyquist domain

4

The design of high-performance mechatronic systems is very challenging, as it requires delicate balancing of system dynamics, the controller, and their closed-loop interaction. Topology optimization provides an automated way to obtain systems with superior performance, although its application to integrated controller-structure optimization has been limited. To allow for topology optimization of mechatronic systems for closed-loop stability and disturbance rejection properties such as modulus margin, we introduce local circular approximations of the Nyquist curve. These circular approximations enable analytical characterization of the Nyquist curve and allow for constraints that affect closed-loop performance. Additionally, a computationally efficient robust formulation is proposed for topology optimization of dynamic systems. Based on approximation of eigenmodes for perturbed designs, their dynamics can be described with sufficient accuracy for optimization, while preventing threefold increase of additional computational effort. Optimized systems with significantly higher performance are found, with bandwidths up to 350% higher than systems optimized for maximum eigenfrequencies, while still satisfying the required modulus margin. The proposed approach enables new directions of integrated (topology) optimization, with precise control over the Nyquist curve and efficient enhancement of geometric robustness.

4.1 Introduction

Many high-tech applications require positioning at both high accuracy and high speed, for which motion systems are used. These are, for instance, used in semiconductor equipment, microscopy, robotics, and medical devices (Munnig Schmidt *et al.*, 2011; Oomen, 2018). The required speed and accuracy in these positioning systems is achieved by feedback control. In the quest for more extreme performance, the design of motion systems poses a significant challenge.

The final performance and accuracy of such systems heavily depend on system dynamics, the controller, and the (closed-loop) interaction between the two (*i.e.* mechatronics). Various complex design problems have been effectively addressed by topology optimization in recent years, and the need exists to also apply it to motion systems. Although optimization is frequently used in the design of feedback controlled systems, it is mostly applied in a sequential manner. First, the structure is designed, *e.g.* for maximum eigenfrequencies using topology optimization (Ma *et al.*, 1995; Delissen *et al.*, 2022), after which a controller is tuned for this structure that achieves system requirements, such as high bandwidth, stability, and disturbance rejection (Munnig Schmidt *et al.*, 2011). However, this approach usually leads to sub-optimal system performance. High eigenfrequencies are often a characteristic of good system performance, but it does not mean that higher eigenfrequencies always result in a higher bandwidth. Therefore, for superior performance of the combined system, an integrated approach is required (Fathy *et al.*, 2001; Van der Veen *et al.*, 2015, 2017), which is also sometimes referred to as control co-design (Garcia-Sanz, 2019). Through integrated (topology) optimization, the dynamic behavior of the structure and the controller can both be adapted to accommodate each other in a more optimal manner, potentially resulting in a better closed-loop performance.

A large portion of existing research on integrated controller-structure optimization is focused on *state-feedback* controllers in the time domain, which determine their correction signals based on the state of the structure (*e.g.* positions, deformations, and/or velocities). The optimal controller in this case can be calculated algebraically as the minimizer of a linear quadratic control cost function, based on \mathcal{H}_2 synthesis (a generalization of classic LQ/LQR/LQG theory) (Doyle *et al.*, 1989; Anderson and Moore, 1989). The result is an optimal controller balancing vibration levels and control effort over time. Most existing methods reformulate the integrated controller-structure optimization problem into a nested formulation, where an optimal controller is found algebraically during each structural design iteration (Haftka, 1990; Fathy *et al.*, 2001). For the outer structural problem the same linear quadratic cost function as for the nested controller optimization can be used (Miller and Shim, 1987). However, this approach is limited to truss problems with few design variables due to its significant computational effort, as the solutions are needed of an algebraic Riccati equation and of additional Lyapunov equations for the gradients of each design variable. Alternatives in literature are based on minimizing combined strain and control energy in a steady-state setting (Ou and Kikuchi, 1996a,b; Molter *et al.*, 2013) or other (multi-)objective formulations (Zhu *et al.*, 2002; da Silveira and Fonseca, 2010). While these are computationally feasible for topology optimization, they do not directly relate to the integrated system performance. A more complete overview of different approaches is given in the review paper by Allison and Herber (2014).

4.1.1 Frequency domain control

In practice, state feedback and linear quadratic optimal controllers in the time domain are rarely used for high-performance positioning systems. For positioning systems the tracking error, disturbance rejection, and noise attenuation are essential aspects to obtain high precision. The quantification of these effects is difficult in the time domain (Doyle, 1978; Zhou *et al.*, 1996), but can be represented easier in the frequency domain. This is one of the reasons that frequency-based PID controllers are the current industry standard (Munnig Schmidt *et al.*, 2011).

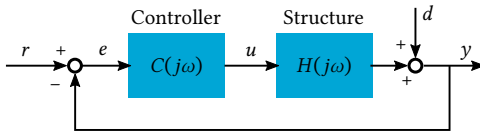


Figure 4.1: Controller and plant placed in a feedback loop, with the aim for the output y to track the reference signal r . The correction signal u generated by the controller is based on the measured error e . If tuned correctly, the closed-loop system is able to reject disturbances d .

In order to clearly describe the open challenges for integrated controller-structure optimization in the frequency domain, we will first discuss some aspects of classical control theory. The influence of disturbances and noise on the controlled structure is characterized by the *sensitivity function* $S(j\omega)$ (Åström and Murray, 2008), which is not to be confused with the design sensitivities. The sensitivity function is the transfer function between external disturbance d and output y (Fig. 4.1), which is dependent on the frequency ω . Here, the disturbances may, for instance, be external loads on the controlled system or motions of the measurement frame. The sensitivity function is defined as

$$S(j\omega) = \frac{1}{1 + L(j\omega)}, \quad (4.1)$$

with the open-loop transfer function $L(j\omega) = H(j\omega)C(j\omega)$ of the controller and plant in series. The amplitude of the sensitivity function $|S(j\omega)|$ provides a bound on the disturbance rejection properties. A typical example is shown in Fig. 4.2a. Disturbances are attenuated in closed-loop if $|S(j\omega)| < 0$ dB, but they are amplified if $|S(j\omega)| > 0$ dB. Ideally, the sensitivity function is small for frequencies below the bandwidth ω_b , where the controller is able to correct disturbances, and which also ensures a small tracking error. Due to the *waterbed effect*, lowering the sensitivity function at certain frequencies leads to an increase at other frequencies (Munnig Schmidt *et al.*, 2011). Therefore, peaks are to be avoided for frequencies above the bandwidth to prevent over-amplification of high-frequency noise. This is usually done by limiting the maximum value of $|S(j\omega)|$ to, for instance, 6 dB. Further details can be found in textbooks on control, e.g. Åström and Murray (2008); Munnig Schmidt *et al.* (2011).

Examples in the literature of integrated optimization for PID control are less common than optimization based on linear quadratic control. One example is the work by Albers and Ottndad (2010), who use a PID controller optimization nested within a structural topology optimization based on strain energy minimization. Here, load cases are iteratively updated based on the control action. However, this approach will not yield optimal performance, since the structure is optimized for a minimum strain energy instead of the integrated system performance.

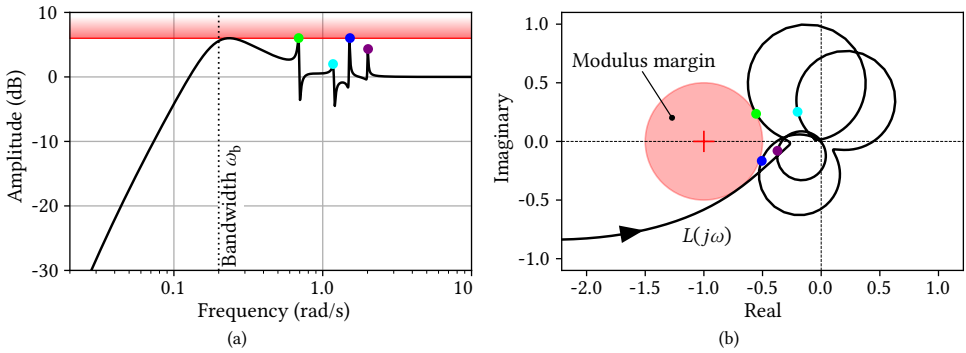


Figure 4.2: a) A typical example of a sensitivity function $|S(j\omega)|$. The upper limit of 6 dB is indicated in red. b) The corresponding Nyquist curve of the loop gain $L(j\omega)$, with the critical -1 point and modulus margin indicated in red. Peaks in the sensitivity function correspond to the points of the Nyquist curve closest to the -1 point, as indicated by the colored dots.

A truly integrated approach is proposed by [Van der Veen et al. \(2015, 2017\)](#), who optimize feedback controlled structures for a maximum bandwidth, subject to constraints on closed-loop stability and disturbance rejection. For the disturbance rejection, constraints are used that explicitly limit the sensitivity function $|S(j\omega)|$ below a certain threshold. Since the sensitivity function is a multi-modal function (Fig. 4.2a), a constraint is imposed on each individual peak value. The frequencies corresponding to the peak values cannot be calculated explicitly, so a numerical search algorithm must be used to locate the peak values (see, e.g. [Bruinsma and Steinbuch, 1990](#)). Even though the peaks are found numerically and as long as the constraints are not dependent on the peak frequency, it is possible to calculate correct gradient information and use them as constraints in an optimization ([Giesy and Lim, 1993](#); [Venini and Pingaro, 2017](#); [Delissen et al., 2020](#)). A drawback of the approach of [Van der Veen et al. \(2015, 2017\)](#) is that the number of peaks changes during the optimization, depending on the controller, the structure, and their interaction. Next to that, separate constraints need to be applied to ensure closed-loop system stability. As a result, integrated optimization including control requirements, such as closed-loop stability and disturbance rejection, remains an open challenge.

For further insight into the behavior of the sensitivity function $|S(j\omega)|$, an alternative interpretation is discussed. The sensitivity function can also be interpreted using the *Nyquist curve* of the open-loop transfer function $L(j\omega)$, as is shown in Fig. 4.2b. From Eq. 4.1 can be deduced that the reciprocal of the sensitivity function is equal to the distance from the Nyquist curve $L(j\omega)$ to the critical point at $-1 + 0j$ in the complex domain (from here on called the -1 point). A maximum in the sensitivity function therefore corresponds to a minimum distance between the open loop transfer-function $L(j\omega)$ and the -1 point. This minimum distance is also commonly known as the *modulus margin* ([Åström and Murray, 2008](#)).

Outside structural and integrated optimization, several techniques are available which focus on gradient-based tuning of controllers using the Nyquist curve, e.g. ([Karimi and Galdos, 2010](#); [Van Solingen et al., 2018](#)). These apply geometric constraints on the Nyquist curve to enforce stability and disturbance rejection margins. An advantage of constraining

the Nyquist curve is an enhanced flexibility in limiting both phase as well as amplitude of a transfer function, which is otherwise difficult to do. However, this approach is not suited for topology optimization, since the Nyquist curve $L(j\omega)$ is sampled using a finite number of frequencies, where each sampled point has to be constrained in the complex domain. This easily results in thousands of constraints that each require a computationally costly (dynamic) finite element analysis.

Topology optimization has not been done yet using the Nyquist curve, although it may offer several advantages. There is a straightforward geometrical interpretation of disturbance rejection using the open-loop transfer function $L(j\omega)$ as opposed to the sensitivity function $|S(j\omega)|$, which is in closed-loop. Also the closed-loop stability can be directly enforced by preventing encirclements of the -1 point (*i.e.* the Nyquist stability criterion in case of a stable open-loop system). This motivates the use of the Nyquist curve in controller design.

4.1.2 Robust formulation

An important requirement for practical design cases is the control on minimum feature size in the design. In topology optimization, this is generally done using a density filter in combination with a robust formulation (Bendsøe and Sigmund, 2003; Wang *et al.*, 2011). Erosion and dilation operations are performed on the design in order to generate multiple perturbed designs. By optimizing the design for worst case performance, it is made robust against uniform geometric deviations. The robust formulation indirectly ensures a minimum feature size in the design, dependent on the perturbation amount and the filter radius. Additionally, it helps in obtaining a binary void-solid design without intermediate densities, possibly also reducing the appearance of local eigenmodes (Pedersen, 2000). A disadvantage is that the application of this method requires the solution of additional perturbed designs, which, in the present setting, each require the solution of a computationally costly eigenvalue problem. Furthermore, the integrated controller-structure optimization as proposed by Van der Veen *et al.* (2015, 2017) does not allow for aggregation of all the perturbed constraint values. This is not possible because the number of peaks in the sensitivity function $|S(j\omega)|$, and thus the number of constraints, may change due to the design perturbations. The lack of aggregation results in the addition of many new constraints for each perturbed design, which all require the calculation of eigenmode design sensitivities. Thus, to apply the robust formulation to existing integrated optimization methods results in an unacceptable increase of computational effort by at least a factor three.

4.1.3 Approach and contributions

In this work, we present two main contributions towards integrated controller-structure optimization and application to more practical design cases:

1. Local approximation of the Nyquist curve using circles, which can be used in gradient-based optimization
2. An efficient robust method for dynamic topology optimization problems, that requires negligible additional computational effort

These new methods are combined, tested, and demonstrated for the integrated controller-structure topology optimization of a motion system.

Local approximation of the Nyquist curve In order to efficiently influence the shape of the Nyquist curve during optimization, local circular approximations are generated at each eigenfrequency. Using multiple circular approximations, the characteristic shape of the Nyquist curve is captured by simple geometric features. Finally, by geometric restriction of each circle in the complex domain, the global shape of the Nyquist curve can be influenced during optimization. This can be used to enforce closed-loop stability (encirclements around the -1 point) and robustness (distance to the -1 point).

This method avoids the requirement of knowing the exact frequencies at peaks in the sensitivity function, or equivalently where the Nyquist curve of $L(j\omega)$ is closest to the -1 point. Instead, locally approximated sections are used to describe the Nyquist curve close to the peak frequencies, which may be constrained away from the -1 point. Each (flexible) eigenmode in the mechanical model exhibits itself as a circle in the Nyquist curve (Fig. 4.2b), which together form its characteristic shape. This also prevents issues with a changing number of peaks in the sensitivity function, as the absence of a peak corresponds to a circle with a radius of zero at the corresponding eigenfrequency.

Circles in the Nyquist curve have historically been used to identify modal parameters of mechanical systems from experimental data (Kennedy and Pancu, 1947; Miller, 1978). Here, the reverse process is exploited by fitting a circle related to each eigenfrequency in the dynamic system, using the corresponding modal parameters. Local approximation models are actively being researched in the field of control, where they are used to, for instance, approximate the \mathcal{H}_∞ norm with limited experimental data (see, e.g. Tacx and Oomen (2021)). However, to our knowledge the current approximation-based approach proposed for integrated controller-structure optimization has not been studied before.

Computationally efficient robust formulation To apply the robust formulation to topology optimization with negligible additional computational effort, we propose to approximate both the eigenfrequencies and eigenmodes of the perturbed designs. This critical, as both of these are important to the closed-loop behavior of the system. The eroded and dilated designs are very similar to the nominal design. Therefore, it may be assumed that their dynamic behavior is also very similar. After calculation of the eigenmodes of the nominal design, approximations of eigenfrequencies and eigenmodes for the perturbed designs may be constructed from linear combinations of the nominal eigenmodes. This avoids having to solve additional eigenvalue problems for the perturbed designs.

The eigenmodes are used to construct a reduced-order model for each design. After this, closed-loop performance may be evaluated for each of the reduced-order models, using the proposed local approximation method of the Nyquist curve. The fact that the number of circles does not change during iterations allows for aggregation of the constraints. Thus, the number of constraints is equal for an optimization with or without robust formulation, which prevents calculation of additional eigenmode design sensitivities.

In this chapter, the contributions are applied to integrated controller and topology optimization with focus on closed-loop system stability and robustness margins on the disturbance rejection. The research is focused on mechanical LTI and SISO systems, but

many aspects may be generalized to a MIMO setting. A fixed-structure PID controller is used for positioning of the mechanical system with in a single motion direction, in the form of rigid body mode. Fixed actuator and sensor locations are used in the system and modal damping is assumed. Furthermore, different variations are explored, such as optimization for position dependency using multiple sensor positions (*i.e.* single-input multi-output (SIMO)) with the same controller and application of the proposed robust formulation.

The outline of this chapter is as follows. First, in Section 4.2, the local approximation of the Nyquist curve using circles is explained and demonstrated on an analytical example. In Section 4.3, the topology optimization formulation is presented. Next, in Section 4.4, all modeling aspects are explained in detail, including the proposed efficient robust formulation for dynamic problems. In Section 4.5, the potential of the proposed methods is demonstrated using numerical examples. Finally, discussion and conclusions are given in Sections 4.6 and 4.7, respectively.

4.2 Local approximation of the Nyquist curve

4.2.1 Circle parametrization

In this section is explained how the circular-shaped local approximations for the flexible eigenmodes in the Nyquist curve $L(j\omega)$ are constructed, based on theory from experimental modal analysis (Kennedy and Pancu, 1947; Miller, 1978). Given the transfer function in the Laplace domain $L(s)$, the Nyquist curve is obtained with complex frequency $s = j\omega$, which corresponds is a line along the imaginary axis. First, the general transfer function is given by its decomposition in first-order terms as

$$L(s) = \sum_i \frac{p_i}{s - \lambda_i}, \quad (4.2)$$

with participation factors $p_i \in \mathbb{C}$, and system poles $\lambda_i \in \mathbb{C}$. It is possible to obtain this decomposition from any representation of the transfer function, for instance from a state-space model as is further explained in Section 4.4.3. For frequencies $s = j\omega$ in the proximity of a system pole λ_i , the corresponding first-order term is assumed dominant, as its denominator becomes small. Therefore,

$$L(s) \approx \tilde{L}_i(s) = \check{L}_i + \frac{p_i}{s - \lambda_i} \quad \text{for } s \approx j\text{Im}(\lambda_i), \quad (4.3)$$

where the local approximation $\tilde{L}_i(s)$ consists of a constant offset $\check{L}_i \in \mathbb{C}$ and a single first-order term. The offset \check{L}_i contains the contributions of all remaining first-order terms at the frequency of interest and is calculated as

$$\check{L}_i = L(j\text{Im}(\lambda_i)) - \frac{p_i}{j\text{Im}(\lambda_i) - \lambda_i} = \sum_{k \neq i} \frac{p_k}{j\text{Im}(\lambda_i) - \lambda_k}, \quad (4.4)$$

ensuring interpolation of $L(j\text{Im}(\lambda_i)) = \tilde{L}(j\text{Im}(\lambda_i))$. An illustration of a local approximation can be seen in Fig. 4.3.

From experimental modal analysis, it is known that a transfer function of the form in Eq. 4.3 results in a circle in the complex domain (Kennedy and Pancu, 1947; Miller, 1978).

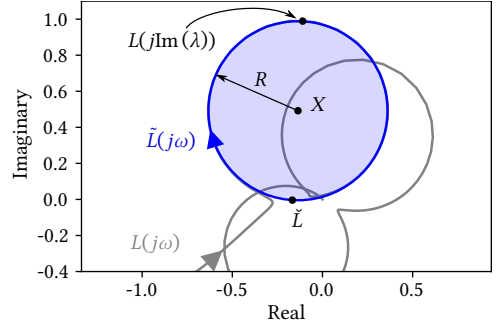


Figure 4.3: Illustration of one local circle approximation $\tilde{L}(j\omega)$ (in blue) fitted to the Nyquist curve $L(j\omega)$ in grey. The radius R , midpoint X , constant offset \tilde{L} , and an interpolatory point $L(j\text{Im}(\lambda))$ are indicated.

Its midpoint and radius are calculated, respectively, using

$$X_i = \tilde{L}_i - \frac{p_i}{2\text{Re}(\lambda_i)} \quad \text{and} \quad R_i = \frac{|p_i|}{2|\text{Re}(\lambda_i)|}. \quad (4.5)$$

An alternative and simplified proof of these relations, based on the theory of generalized circles (Schwerdtfeger, 1979), is provided in Appendix A.2. As the relations are all analytical, the derivation of the derivatives is deemed trivial and is left to the reader. By constructing local circle approximations for each relevant system pole λ_i , important features of the Nyquist curve of $L(s)$ can be described using simple geometry.

Note that the radius is non-differentiable when $|p_i| = 0$ and additionally approaches infinity when $\text{Re}(\lambda_i) \rightarrow 0$. The former case occurs when an eigenmode is not excited by the actuator or when it has no deformation at the sensor location. The latter case will normally not occur, since the real part of a complex pole is a finite negative value for a system with damping. To account for non-differentiability when $|p_i| = 0$, and thus $R_i = 0$, a small perturbation is added as

$$\tilde{R}_i = \sqrt{R_i^2 + R_{\min}^2}. \quad (4.6)$$

This ensures differentiability when $R_i = 0$ by setting a (smooth) minimum radius of R_{\min} .

4.2.2 Analytical example

To demonstrate the principle of the local circle approximation, a double mass spring damper system is used, as is shown in Fig. 4.4a. To keep the equations simple, no controller is used for this example and circles are formed for the plant $H(s)$ instead of the loop $L(s)$. The transfer function $H(s)$ for this system describes the relation between a force on either of the masses to a displacement on either. Mathematically, it is the superposition of two second-order systems (Gawronski, 2004; Munnig Schmidt *et al.*, 2011):

$$H(s) = \frac{\chi_1}{\Omega_1^2 + 2s\zeta_1\Omega_1 + s^2} + \frac{\chi_2}{\Omega_2^2 + 2s\zeta_2\Omega_2 + s^2}. \quad (4.7)$$

Here, undamped eigenfrequencies are denoted Ω_1, Ω_2 , relative damping factors ζ_1, ζ_2 , and modal contributions χ_1, χ_2 . These modal parameters can be calculated from the mass, stiffness and damping values of the double mass spring system in Fig. 4.4a and can be positive

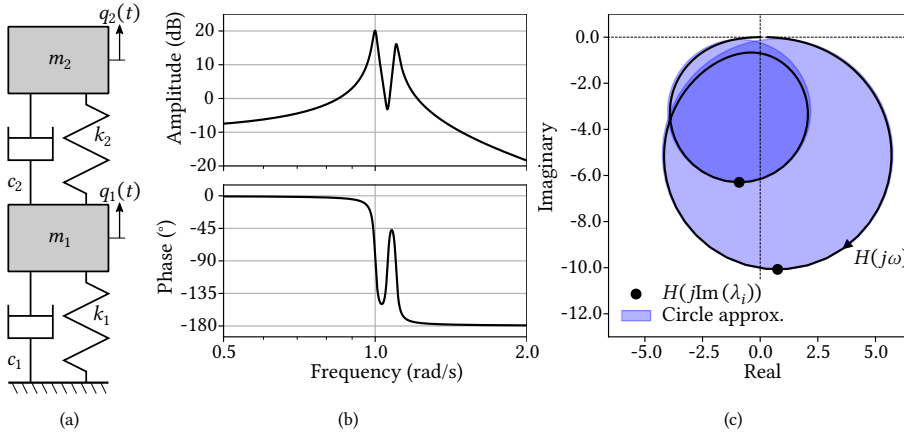


Figure 4.4: a) A double mass spring damper system, which can be described using Eq. 4.7. b) Bode plot of the double second-order system and c) corresponding Nyquist plot, where the approximated circles and interpolated points $H(j\text{Im}(\lambda_i))$ are indicated. The parameters used are $\Omega_1 = 1.0$ rad/s, $\Omega_2 = 1.1$ rad/s, $\chi_1 = 0.2 \text{ kg}^{-1}$ (collocated), $\chi_2 = 0.15 \text{ kg}^{-1}$, and $\zeta_1 = \zeta_2 = 0.01$.

(e.g. collocated) or negative (e.g. non-collocated) (Gawronski, 2004). This equation can be rewritten into a notation using system poles λ_i and their conjugates $\bar{\lambda}_i$, becoming

$$H(s) = \frac{\chi_1}{(s - \lambda_1)(s - \bar{\lambda}_1)} + \frac{\chi_2}{(s - \lambda_2)(s - \bar{\lambda}_2)}, \quad (4.8)$$

where the system poles are calculated as $\lambda_i = -\zeta_i\Omega_i + j\Omega_i\sqrt{1 - \zeta_i^2}$ in case of an underdamped system.

The Bode plot of this system in Fig. 4.4b shows the frequency-dependent amplitude and phase behavior of the transfer function $H(j\omega)$. Resonances can clearly be observed, which are located at the damped eigenfrequencies $\text{Im}(\lambda_i)$ in the Bode plot. Alternatively, the transfer function can be represented in the complex domain by a Nyquist plot, shown in Fig. 4.4c. Looking at the Nyquist plot, the circular shapes can clearly be identified, with their apexes with respect to the origin coinciding with the damped eigenfrequencies $\text{Im}(\lambda)$. Note that the furthest point from the origin can be calculated explicitly, as opposed to the distance to the -1 point, which cannot be calculated.

Circles cannot be fit directly to the second-order systems, therefore the transfer function first needs to be decomposed into first-order terms. In this case, this is simply done by rewriting Eq. 4.8 into

$$H(s) = \frac{p_1}{s - \lambda_1} - \frac{\bar{p}_1}{s - \bar{\lambda}_1} + \frac{p_2}{s - \lambda_2} - \frac{\bar{p}_2}{s - \bar{\lambda}_2}, \quad (4.9)$$

with corresponding participation factors

$$p_i = -\frac{j\chi_i}{2\text{Im}(\lambda_i)}. \quad (4.10)$$

From the four first-order systems in Eq. 4.9, only one first-order system is assumed dominant around each of the excitation frequencies $\omega \approx \text{Im}(\lambda_i)$ and $\omega \approx -\text{Im}(\lambda_i)$. Since only positive frequencies are of interest, the two approximated circles using Eqs. 4.3-4.5 can be described with radii and midpoints being

$$R_i = \frac{|\chi_i|}{4\zeta_i\Omega_i^2\sqrt{1-\zeta_i}} \quad \text{and} \quad X_i = \check{H}_i - \frac{j\chi_i}{4\zeta_i\Omega_i^2\sqrt{1-\zeta_i}}, \quad (4.11)$$

with constant offsets

$$\check{H}_i = H(j\text{Im}(\lambda_i)) + \frac{j\chi_i}{2\zeta_i\Omega_i^2\sqrt{1-\zeta_i}}. \quad (4.12)$$

4

Two circles are calculated and overlaid in Fig. 4.4c, demonstrating approximation with a close match to the original Nyquist curve. The approximation is most approximate near the eigenfrequency at which the circle interpolates the point $H(j\text{Im}(\lambda_i))$. From Eq. 4.11 can be seen that increasing the damping value or eigenfrequency would decrease circle radius, and the modal contributions χ_i have a proportional effect on the radii.

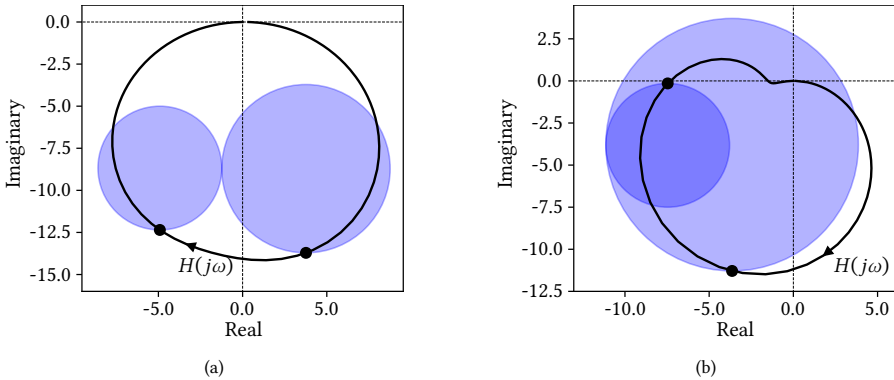


Figure 4.5: The Nyquist diagrams and local circle approximations for two systems showing mode interaction because of frequencies close to each other, at $\Omega_1 = 1.0$ rad/s and $\Omega_2 = 1.01$ rad/s. The damping parameters are $\zeta_1 = \zeta_2 = 0.01$. System input and output can be at either of the two masses. a) Interaction with both modal contributions positive ($\chi_1 = 0.2 \text{ kg}^{-1}$ and $\chi_2 = 0.15 \text{ kg}^{-1}$, e.g. collocated system) results in approximation smaller than the actual Nyquist curve. b) Interaction with opposed modal contributions ($\chi_1 = 0.3 \text{ kg}^{-1}$ and $\chi_2 = -0.15 \text{ kg}^{-1}$, e.g. non-collocated system) results in larger circles than the Nyquist curve, as the two modes cancel each other.

When eigenfrequencies are close to each other, they start interacting with each other. The mixing of modes results in non-circular shapes in the Nyquist curve. At this point the approximation in Eq. 4.3 is unable to fully capture the exact behavior, as the influence of other modes (\check{H}) is no longer (close to) constant. Using the double second-order system, this is demonstrated in Fig. 4.5a for a system with positive modal contributions (e.g. in a collocated system). In this case the two second-order terms contribute in the same direction and the total response is larger than the approximations. The opposite happens when the signs of the modal contributions are opposed (e.g. in a non-collocated system),

as can be seen in Fig. 4.5b, where the approximated circles are larger than the actual response. The two modes compensate each other and the total response becomes smaller. These examples are specifically tuned to show the effect of mode interaction, but these extreme cases may be rare to occur in an optimization setting. This will be investigated in Section 4.5 using numerical examples.

4.2.3 Constraining the Nyquist curve

Using the local circle approximations, the Nyquist curve can be parametrized in the complex domain using simple geometry. This is very useful for optimization problems where the Nyquist curve must geometrically be constrained in the complex domain.

Distance to a point For instance, the closest distance h from a circle to a point $\tau \in \mathbb{C}$ is characterized as the distance to the midpoint of the circle minus its radius

$$h(X, R) = |X - \tau| - R. \quad (4.13)$$

To calculate the distance furthest away, the radius is simply added instead of subtracted

$$h(X, R) = |X - \tau| + R. \quad (4.14)$$

Distance to a line The shortest distance to a line characterized by unit normal direction $n \in \mathbb{C}$ (with $|n| = 1$) and passing through the point τ can easily be calculated as

$$h(X, R) = \operatorname{Re}((X - \tau)\bar{n}) - R. \quad (4.15)$$

Distance to an area By composing distances to lines and points, also the distance from a circle to an area can be characterized. For instance, the shortest distance to a wedge-shaped area bounded by two line sections with normals $n_1, n_2 \in \mathbb{C}$ intersecting in the point τ , is defined as

$$h(X, R) = \begin{cases} |X - \tau| & \text{if } \mathcal{E}_1 \\ \operatorname{Re}((X - \tau)\bar{n}_1) & \text{if } \mathcal{E}_2 \\ \operatorname{Re}((X - \tau)\bar{n}_2) & \text{if } \mathcal{E}_3 \end{cases} - R, \quad (4.16)$$

where the conditions $\mathcal{E}_1, \mathcal{E}_2$, and \mathcal{E}_3 indicate which of the three sections (lines or point) is closest to the position of X . These functions are mostly smooth and differentiable, except when point X coincides with τ or at an inflection point between two segments. However, these cases will numerically rarely occur, especially when these are used in constraints that serve to keep the point X away from τ .

4.3 Application to controller-structure optimization

4.3.1 Optimization formulation

In a closed loop controlled system, the interplay between controller and structure determines the performance that can be achieved. The feedback system consists of a PID controller $C(s)$ and the structure $H(s)$, which contains a rigid body mode, placed in a loop, as is shown in Fig. 4.1.

From an optimization point of view, there is a trade-off between performance (bandwidth) and closed loop stability. Stability can be determined by inspecting the closed-loop poles, which must have a negative real part. Using the Nyquist stability criterion, closed-loop stability can also be interpreted with the Nyquist curve: for a stable closed-loop system, the open-loop curve $L(s = j\omega)$ must not encircle the -1 point (in the current case where the open-loop system is stable), which for positive ω means that $L(j\omega)$ keeps the -1 point to the left hand side for increasing frequencies (Munnig Schmidt *et al.*, 2011). Here, the open-loop transfer-function is calculated as the controller and plant in series $L(s) = H(s)C(s)$.

As discussed in the Introduction, the modulus margin gives information on how close a system is to instability, and it also provides a bound on the influence of disturbances on the controlled structure. It is characterized as the closest distance of the Nyquist curve $L(j\omega)$ to the -1 point.

To ensure a closed-loop system which is stable with a specified modulus margin, the locally approximated circles are used to constrain the trajectory of the Nyquist curve $L(j\omega)$. Constraints are defined that prevent the circle approximations, corresponding to the mechanical eigenmodes, from entering the wedge-shaped area offset by μ around the -1 point as indicated in Fig. 4.6. In this way, both stability and disturbance rejection are enforced by the constraints.

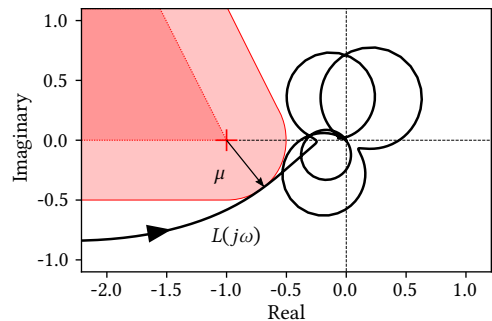


Figure 4.6: The constrained area in the Nyquist diagram indicated in red, which ensures both closed-loop stability and a modulus margin of μ . The wedge-shaped area (Eq. 4.16) is shaded in dark red, which is offset with the modulus margin to the lighter shade of red.

Also multiple Nyquist curves can be constrained simultaneously, for instance, to account for *position-dependent* dynamics. Many high-tech positioning systems consist of motion systems stacked in series to provide positioning freedom in additional movement directions or to achieve an extended range of motion. Since contactless measurements are often used (*e.g.* laser interferometry or eddy current sensors), a sensor fixed on a measurement frame therefore changes position relative to the measured object. As the measurement position affects the dynamics, it becomes position dependent (Van der Veen *et al.*, 2017). In this work, the inclusion of multiple (N_{pos}) relative sensor-positions is therefore

also considered. This results in multiple SISO control loops, or rather SIMO, each requiring performance constraints on disturbance rejection.

For the topology optimization, a density-based formulation is used (Bendsøe and Sigmund, 2003). The optimization formulation used in this work is stated as

$$\begin{aligned}
 \min_{\mathbf{x}, \omega_b} \quad & \frac{1}{\omega_b}, \\
 \text{s.t.} \quad & V(\mathbf{x}) \leq v_f V_{\max}, \\
 & h_{ij}(\mathbf{x}, \omega_b) \geq \mu \quad \forall \quad \begin{cases} i = 1, \dots, N \\ j = 1, \dots, N_{\text{pos}} \end{cases}, \\
 & 0 \leq \mathbf{x} \leq 1,
 \end{aligned} \tag{4.17}$$

where \mathbf{x} represents the pseudo-density variables used for topology optimization and ω_b the bandwidth, which is the tuning parameter of the PID controller. The number of eigenmodes in the system is equal to N , for each of which circular approximations are constrained. The aim is to maximize the bandwidth ω_b of the closed-loop system while keeping the volume V below a volume fraction v_f of the maximum volume V_{\max} , and simultaneously ensuring the circle approximations remain outside of the wedge-shaped area by using the distances h_{ij} as defined in Eq. 4.16. These distances are related to the design variables through the radii $R_{ij}(\mathbf{x}, \omega_b)$ and midpoints $X_{ij}(\mathbf{x}, \omega_b)$ of the circular local approximations.

4

4.3.2 Optimization implementation and scaling

As optimizer, MMA is used (Svanberg, 1987). Constraint and objective scaling is critical to this method, so the original optimization formulation of Eq. 4.17 is reformulated as

$$\begin{aligned}
 \min_{\mathbf{x}, x_\omega} \quad & 100 \frac{\omega_b^{(0)}}{\omega_b(x_\omega)}, \\
 \text{s.t.} \quad & 10 \left(\frac{V(\mathbf{x})}{v_f V_{\max}} - 1 \right) \leq 0, \\
 & g_{ij}(\mathbf{x}, x_\omega) \leq 0 \quad \forall \quad \begin{cases} i = 1, \dots, N \\ j = 1, \dots, N_{\text{pos}} \end{cases}, \\
 & 0 \leq \mathbf{x} \leq 1, \\
 & 0 \leq x_\omega \leq 1,
 \end{aligned} \tag{4.18}$$

where the objective is normalized with the bandwidth at the initial iteration $\omega_b^{(0)}$ and a normalized design variable x_ω is used to tune the controller. The constraints on the circles are scaled and normalized as

$$g_{ij} = 10 \left(1 - \frac{h_{ij}}{\mu} \right). \tag{4.19}$$

Instead of directly using the bandwidth as a variable, it is scaled exponentially between the user-defined bounds $[\omega_{\min}, \omega_{\max}]$ as

$$\omega_b = \omega_{\min} \left(\frac{\omega_{\max}}{\omega_{\min}} \right)^{x_\omega}. \tag{4.20}$$

This causes less sensitive behavior for parameter changes at low bandwidth, and makes all optimization variables (\mathbf{x} and x_ω) equally bounded between 0 and 1.

To ensure a feasible initial controller for a given initial structure $\mathbf{x}^{(0)}$ (uniform densities equal to the volume fraction v_f), a separate controller optimization is performed prior to the integrated controller-structure optimization. The control variable x_ω is found using the formulation of this pre-optimization, given as

$$\begin{aligned} \min_{x_\omega} \quad & 100 \frac{\omega_{\min}}{\omega_b(x_\omega)}, \\ \text{s.t.} \quad & g_{ij}(x_\omega) \leq 0 \quad \forall \begin{cases} i = 1, \dots, N \\ j = 1, \dots, N_{\text{pos}} \end{cases}, \\ & 0 \leq x_\omega \leq 1, \end{aligned} \quad (4.21)$$

which has its optimum at $\omega_b^{(0)}$. This value is used as initial bandwidth for the integrated optimization given in Eq. 4.18.

4.3.3 Topology optimization parametrization

Since a density based approach is used, the structural design variables \mathbf{x} are first filtered using a standard density filter, resulting in the filtered design field \mathbf{x}_f (Bruns and Tortorelli, 2001). The Young's modulus E_i and density ρ_i of each finite element i in the domain \mathcal{E} are obtained from the filtered design parameters using the following material interpolation

$$\begin{aligned} E_i &= E_0 \left(x_{\min} + (1 - x_{\min}) x_{f,i}^3 \right) \quad \forall i \in \mathcal{E}, \\ \rho_i &= \begin{cases} \rho_0 x_{f,i} & \text{for } x_{f,i} \geq t \\ \rho_0 \frac{x_{f,i}^6}{t^5} & \text{for } x_{f,i} < t \end{cases} \quad \forall i \in \mathcal{E}. \end{aligned} \quad (4.22)$$

The small minimum design density x_{\min} prevents the stiffness matrix from becoming exactly singular when design densities are zero.

The low mass-to-stiffness ratio in Eq. 4.22 for low densities largely prevents the occurrence of local eigenmodes (Olhoff and Du, 2005). These are unwanted eigenmodes in low density areas, with low corresponding eigenfrequencies. Local modes are further prevented using a *flood fill* algorithm on the design vector \mathbf{x} , removing any material that is disconnected or very loosely connected to actuator or sensor locations. Elements that are connected to the non-design domains through densities lower than 0.2 are recursively clipped to the maximum of their neighbors. In an extreme case, the disconnection of bodies results in additional rigid body modes at frequencies close to zero. These measures prevent undesired localized modes, improving the convergence of the optimization.

Next, the stiffness and mass matrices are assembled using the material properties \mathbf{E} and $\boldsymbol{\rho}$. For this, a grid of bilinear quadrilateral finite elements is used, with a full integration scheme and a plane strain condition. The assembly is performed as

$$\mathbf{K} = \bigoplus_{i \in \mathcal{E}} E_i \mathbf{K}_0 \quad \text{and} \quad \mathbf{M} = \bigoplus_{i \in \mathcal{E}} \rho_i \mathbf{M}_0, \quad (4.23)$$

where \mathbf{K}_0 and \mathbf{M}_0 represent element stiffness and (lumped) mass matrix, respectively, corresponding to unit material properties, and \mathbf{A} denotes the matrix assembly operation over the entire domain \mathcal{E} .

4.4 Modeling

4.4.1 Mechanical model

From the mass and stiffness matrices \mathbf{M} and \mathbf{K} , a reduced-order model is constructed using a truncated modal decomposition. This model approximates the displacement field $\mathbf{u}(t)$ by superposition of a number of eigenmodes ϕ_i scaled over time with amplitudes $q_i(t)$, denoted as

$$\begin{aligned} \mathbf{u}(t) &\approx \sum_{i=1}^N q_i(t) \phi_i = \Phi \mathbf{q}(t), \\ \Phi &= [\phi_1 \quad \dots \quad \phi_N], \end{aligned} \quad (4.24)$$

where Φ is the projection matrix containing all eigenmodes. The eigenfrequencies Ω_i and corresponding eigenmodes ϕ_i are obtained by solving the undamped eigenvalue problem for the lowest $N + 1$ modes

$$\begin{aligned} (\mathbf{K} - \Omega_i^2 \mathbf{M}) \phi_i &= \mathbf{0} \quad \forall \quad i = 0, \dots, N, \\ 0 &\leq \Omega_0 \leq \dots \leq \Omega_N, \end{aligned} \quad (4.25)$$

using mass-normalization of the eigenmodes as $\phi_i^T \mathbf{M} \phi_i = 1$. The lowest eigenfrequency $\Omega_0 = 0$ rad/ms corresponds to the rigid body mode for the degree of freedom that is controlled by the PID controller.

The projection matrix Φ is used to obtain the reduced equations of motion as

$$\begin{aligned} \Omega^2 \mathbf{q}(t) + 2\zeta \Omega \dot{\mathbf{q}}(t) + \ddot{\mathbf{q}}(t) &= \Phi^T \mathbf{f} u(t), \\ \mathbf{y}(t) &= \mathbf{G}^T \Phi \mathbf{q}(t), \end{aligned} \quad (4.26)$$

where Ω is a diagonal matrix containing the eigenfrequencies and ζ the non-dimensional damping ratio. The input force vector, as exerted by the actuator, is denoted as \mathbf{f} and the output displacement vectors as measured by the sensors with block-vector \mathbf{G} , with N_{pos} columns for each sensor. The input is denoted $u(t)$ and the outputs for all sensor positions $\mathbf{y}(t)$, as indicated in Fig. 4.1. The transfer function of the plant becomes

$$\mathbf{H}(s) = \mathbf{G}^T \Phi (\Omega^2 + 2s\zeta\Omega + s^2 \mathbf{I})^{-1} \Phi^T \mathbf{f}, \quad (4.27)$$

which describes the behavior between the input and N_{pos} outputs of the plant in the frequency domain.

4.4.2 Controller

A PID controller with additional low-pass filter is used for feedback control of the rigid body mode, which is defined by the control law

$$C(s) = k \frac{s + \frac{1}{5} \omega_b}{s} \frac{3s + \omega_b}{s + 3\omega_b} \frac{5\omega_b}{s + 5\omega_b}, \quad (4.28)$$

with tuning parameters gain k and bandwidth ω_b . This is a PID controller based on industry standard rules-of-thumb, with integral action until $\omega_b/5$, phase lead between $\omega_b/3$ and $3\omega_b$, and first-order roll-off beyond $5\omega_b$ (Munnig Schmidt *et al.*, 2011; Van der Veen *et al.*, 2015). The Bode plot of this controller can be seen in Fig. 4.7. In the optimization, only bandwidth is a design variable, and the gain is calculated using

$$k = \frac{k_0}{|H_m(j\omega_b)|} = k_0 m \omega_b^2, \quad (4.29)$$

where m is the mass of the system, and the rigid body mode response of the plant is equal to

$$H_m(s) = \frac{1}{ms^2}. \quad (4.30)$$

This ensures that the open-loop gain at the bandwidth $|L(j\omega_b)| = k_0$. In current work, the gain value is chosen as $k_0 = 1.1$, which ensures correct interaction between the controller and the rigid body mode (Munnig Schmidt *et al.*, 2011). Note that the method is not limited to this specific control law and variations in control behavior and parametrization are possible.

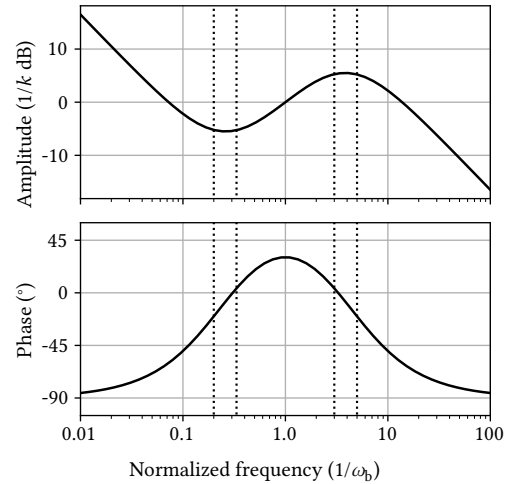


Figure 4.7: Bode plot of the controller $C(j\omega)$, with normalized axes. The dotted lines indicate frequencies at $1/5$, $1/3$, 3 , and 5 times the bandwidth ω_b .

The control law can be rewritten into state-space form

$$\begin{aligned} \dot{\mathbf{c}}(t) &= \mathbf{A}_c \mathbf{c}(t) + \mathbf{B}_c \mathbf{e}(t) \\ \mathbf{u}(t) &= \mathbf{C}_c \mathbf{c}(t) \end{aligned} \quad (4.31)$$

where \mathbf{A}_c , \mathbf{B}_c , \mathbf{C}_c represent the controller structure in canonical form (Skogestad and Postlethwaite, 2001). The vector \mathbf{c} contains the internal state of the PID controller and is of length 3.

The open-loop response is obtained by placing the controller (Eq. 4.31) and plant (Eq. 4.27) in series, connecting the output of the controller to the input of the plant. In the

form of a state-space model in the time domain this becomes

$$\begin{aligned}\dot{\mathbf{z}}(t) &= \mathbf{A}_1 \mathbf{z}(t) + \mathbf{B}_1 e(t), \\ \mathbf{y}(t) &= \mathbf{C}_1 \mathbf{z}(t),\end{aligned}\quad (4.32)$$

with system matrices and state vector

$$\begin{aligned}\mathbf{A}_1 &= \begin{bmatrix} \mathbf{A}_c & \mathbf{0} & \mathbf{0} \\ \mathbf{0} & \mathbf{0} & \mathbf{I} \\ \Phi^T \mathbf{f} \mathbf{C}_c & -\Omega^2 & -2\zeta\Omega \end{bmatrix}, \\ \mathbf{B}_1 &= [\mathbf{B}_c \quad \mathbf{0} \quad \mathbf{0}]^T, \\ \mathbf{C}_1 &= [\mathbf{0} \quad \mathbf{G}^T \Phi \quad \mathbf{0}], \\ \mathbf{z} &= [\mathbf{c} \quad \mathbf{q} \quad \dot{\mathbf{q}}]^T.\end{aligned}\quad (4.33)$$

The transfer function of the open-loop gain becomes

$$\mathbf{L}(s) = \mathbf{H}(s)\mathbf{C}(s) = \mathbf{C}(s\mathbf{I} - \mathbf{A})^{-1} \mathbf{B}, \quad (4.34)$$

which can be used to calculate the open-loop responses in the frequency domain.

4.4.3 Modal decomposition

Before circles can be mapped to the open-loop transfer-function $L(j\omega)$, the transfer function needs to be decomposed into first-order terms. From the state-space model (Eq. 4.34), the poles can directly be obtained by an eigen-decomposition of the system matrix \mathbf{A} as

$$\begin{aligned}\mathbf{A}\mathbf{Q} &= \mathbf{Q}\mathbf{\Lambda}, \\ \mathbf{A} &= \mathbf{Q}\mathbf{\Lambda}\mathbf{Q}^{-1},\end{aligned}\quad (4.35)$$

where matrix \mathbf{Q} contains all eigenmodes of the (right) eigenvalue problem and matrix $\mathbf{\Lambda}$ has all the complex-valued poles λ_i on its diagonal. Substitution into the transfer-function of Eq. 4.34 yields

$$\begin{aligned}\mathbf{L}(s) &= \mathbf{C}(s\mathbf{I} - \mathbf{Q}\mathbf{\Lambda}\mathbf{Q}^{-1})^{-1} \mathbf{B} \\ &= \mathbf{C}\mathbf{Q}(s\mathbf{I} - \mathbf{\Lambda})^{-1} \mathbf{Q}^{-1} \mathbf{B} \\ &= \sum_i^{N_s} \frac{\mathbf{P}_i}{s - \lambda_i}.\end{aligned}\quad (4.36)$$

Here, the matrix \mathbf{P}_i denotes the participation factors of all input and output combinations for mode i . The participation factors can be calculated as

$$p_{ijk} = [\mathbf{C}\mathbf{Q}]_{ji} [\mathbf{Q}^{-1} \mathbf{B}]_{ik} \quad (4.37)$$

for a general MIMO system, where the outputs are indexed with j and the inputs with k . The current application only considers one input, so the last index is omitted. The number of first-order terms equals the number of state variables $N_s = 2N + 5$; two originating from

each flexible eigenmode included in the reduced-order model, two from the rigid body mode, and three from the controller. The negative frequencies are not of interest and the five poles corresponding to controller and the rigid body mode cannot be approximated by a circle. Therefore, only N circles are fitted to the flexible modes and constrained in the complex domain. With this decomposition, the radii and midpoints of the circles can now be found using Eq. 4.5.

4.4.4 Efficient robust formulation

To apply the robust formulation in topology optimization, first perturbed designs need to be generated by erosion and dilation. This is performed using the smooth Heaviside operator defined as

$$x_{p,i}(\eta) = \frac{\tanh(\beta\eta) + \tanh(\beta(x_{f,i} - \eta))}{\tanh(\beta\eta) + \tanh(\beta(1 - \eta))} \quad \forall \quad i \in \mathcal{E}, \quad (4.38)$$

using the filtered design field \mathbf{x}_f , resulting in a projected design \mathbf{x}_p (Wang *et al.*, 2011). The parameter β determines the edge contrast of the projection and η the amount of dilation or erosion, where a value of $\eta = 0.5$ corresponds to the nominal design. By choosing multiple different values of η , multiple perturbed designs $\mathbf{x}_p(\eta_k)$ are generated.

However, straightforward analysis of each of these designs (as described to preceding sections) results in an additional computational burden, as a model has to be created for each design. This means that for each projected design the eigenvalue problem needs to be solved (Eq. 4.25), which is a very computationally intensive step in the analysis.

As an alternative, we propose to approximate the eigenfrequencies and eigenmodes of the perturbed designs, using the reduction basis Φ with eigenmodes corresponding to the nominal design. This means that only the eigenvalue problem of the nominal design needs to be solved and it is assumed that the eigenmodes of the nominal model can be used to describe the behaviour of the other perturbed designs.

The eigenvalue approximation proceeds as follows: using the different perturbed designs $\mathbf{x}_p(\eta_k)$ instead of the filtered design \mathbf{x}_f , the corresponding mass \mathbf{M}_k and stiffness \mathbf{K}_k matrices are assembled using Eqs. 4.22 and 4.23. Next, one eigenvalue problem is solved (Eq. 4.25) using the mass and stiffness matrices corresponding to the nominal design, yielding the reduction basis Φ . Instead of solving additional eigenvalue problems for the other projected designs, their system matrices are projected using the reduction basis belonging to the nominal design as

$$\tilde{\mathbf{K}}_k = \Phi^T \mathbf{K}_k \Phi \quad \text{and} \quad \tilde{\mathbf{M}}_k = \Phi^T \mathbf{M}_k \Phi. \quad (4.39)$$

These projected matrices are then diagonalized by solving the small eigenvalue problem

$$\tilde{\mathbf{K}}_k \mathbf{V}_k = \tilde{\mathbf{M}}_k \mathbf{V}_k \mathbf{Y}_k^2, \quad (4.40)$$

resulting in

$$\mathbf{V}_k^T \tilde{\mathbf{K}}_k \mathbf{V}_k = \mathbf{Y}_k^2 \quad \text{and} \quad \mathbf{V}_k^T \tilde{\mathbf{M}}_k \mathbf{V}_k = \mathbf{I}. \quad (4.41)$$

The matrix \mathbf{Y}_k is a diagonal matrix containing the approximate eigenfrequencies of the perturbed design, which are in fact Ritz values. The corresponding approximate eigenmodes

are linear combinations of the nominal eigenmodes, calculated as $\Phi \mathbf{V}_k$. The system of equations for the perturbed designs now be found as

$$\begin{aligned} \mathbf{Y}_k^2 \mathbf{q}(t) + 2\zeta \mathbf{Y}_k \dot{\mathbf{q}}(t) + \ddot{\mathbf{q}}(t) &= \mathbf{V}_k^T \Phi^T \mathbf{f} u(t), \\ \mathbf{y}(t) &= \mathbf{G}^T \Phi \mathbf{V}_k \mathbf{q}(t). \end{aligned} \quad (4.42)$$

The remainder of the analysis follows the same steps for each model, so first the controller is added to form the open-loop state-space model (Section 4.4.2). This is again decomposed into first-order systems by calculating the poles and participation factors (Section 4.4.3), after which circle approximations are formed for each eigenmode (Section 4.2.1). Finally, distances from the circles to the -1 point are calculated for each eigenmode to form constraints.

After the calculation, each perturbed model k has different constraint values $g_{ij,k}$ for each of its circles, corresponding to mode i and sensor position j . To limit the number of constraints from the different models, they are aggregated using an induced aggregation function (Kennedy and Hicken, 2015)

$$f = \frac{\sum_k f_k \exp(b f_k)}{\sum_k \exp(b f_k)}, \quad (4.43)$$

for any constraint $f = g_{ij}$. This function approximates the worse-case constraint values (*i.e.* the maximum) between the perturbed projections, controlled by the parameter b . For a large parameter b this expression approaches the true maximum. This particular function is chosen because $f = f_k$ in case all values f_k are equal. The robust parameter β introduced in Eq. 4.38 is increased during the optimization, meaning that for the initial iterations all perturbed designs are similar, and so are their constraint values. With this choice of aggregation function, the constraint values are not under- or over-estimated during the early phase of the optimization. The aggregation ensures the number of constraints does not increase when using the robust formulation, and thus no extra computational effort is required to calculate eigenmode design sensitivities (Lee, 1999).

4.5 Results

4.5.1 Case and settings

The numerical case that is used to demonstrate the method is shown in Fig. 4.8. To ensure a position-independent system, N_{pos} different sensor positions are defined at the measurement surface. Measuring at any of these locations and using that signal for feedback control should result in a closed-loop stable system with required disturbance rejection.

In Table 4.1, the settings are listed as used in the optimization, where the material properties correspond to those of aluminium. Furthermore, the maximum number of design iterations is limited to 200 to prevent excessive calculation times. For the optimization, MMA is used with default settings. A move limit of 0.05 is used on the design variables to prevent large steps and oscillations.

4.5.2 Sequential optimization

To be able to compare performance, a reference case is presented based on a sequential optimization. The structure is found by maximization of eigenfrequencies, and subsequently

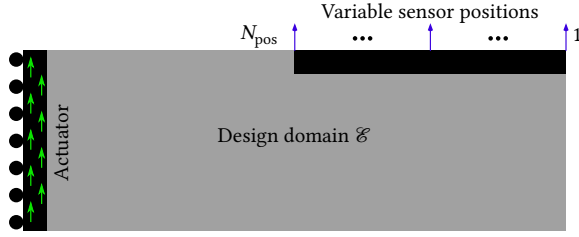


Figure 4.8: The case used for the optimizations, which has one rigid body mode in vertical direction. The actuator forces (green arrows) act uniformly on the non-design domain (black) to the left. The top-right non-design domain represents the surface where accuracy is required. Here, vertical displacements are measured at N_{pos} different sensor locations (blue arrows). The domain of dimensions 300×100 mm, with an in-plane thickness of 300 mm, and is discretized into 210×70 elements.

4

Table 4.1: Settings as used for the optimization.

Symbol	Value	Description
ω_{\min}	0.1 rad/ms	Minimum bandwidth
ω_{\max}	10.0 rad/ms	Maximum bandwidth
μ	0.5	Modulus margin
E_0	65 GPa	Young's modulus
ρ_0	2.6×10^{-6} kg/mm ³	Material density
x_{\min}	10^{-7}	Min. design density
ζ	0.01	Damping factor
N	10	Number of eigenmodes
v_f	0.3	Volume fraction
	2 elements	Density filter radius
β	1.0 - 20.0	Robust edge contrast
η	0.5 ± 0.05	Robust cutoff
b	1.0	Aggregation constant

the PID controller is optimized using the proposed method (Eq. 4.21). The optimization formulation used for the eigenfrequency maximization is given as

$$\begin{aligned}
 \min_{\mathbf{x}} \quad & 100 \frac{g_{\Omega}(\mathbf{x})}{g_{\Omega}^{(0)}}, \\
 \text{s.t.} \quad & 10 \left(\frac{V(\mathbf{x})}{v_f V_{\max}} - 1.0 \right) \leq 0, \\
 & 0 \leq \mathbf{x} \leq 1,
 \end{aligned} \tag{4.44}$$

in which g_{Ω} is the objective function, defined as

$$g_{\Omega}(\mathbf{x}) = \sum_{i=0}^3 \frac{1}{\Omega_i(\mathbf{x})}. \tag{4.45}$$

The superscripted variable $g_{\Omega}^{(0)}$ denotes the value at the initial design iteration. This formulation maximizes the harmonic mean of the first three eigenfrequencies (Ma *et al.*, 1995).

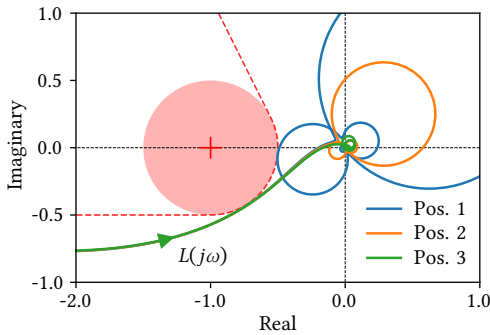


Figure 4.9: Design and Nyquist plot after maximization of eigenfrequencies and sequential maximization of bandwidth. The sensor locations are indicated with colors corresponding to the different Nyquist curves.

The resulting structure after optimization of the eigenfrequencies is shown in Fig. 4.9 and the subsequent controller optimization is able to achieve a bandwidth of 1.11 rad/ms. From the Nyquist plot in Fig. 4.9 can be seen that the controller satisfies closed-loop stability and disturbance rejection requirements. It can also be seen that only the sensor position at the tip (position 1) is limiting the bandwidth, of which the second eigenmode is touching the margin. Therefore, optimizing for different number of sensor positions will result in an equal bandwidth, provided the sensor location at the tip is included.

4

4.5.3 Integrated optimization

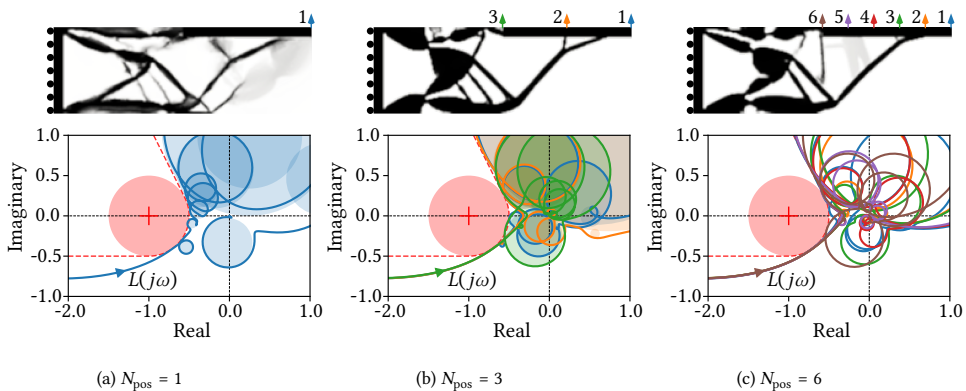


Figure 4.10: Resulting designs and Nyquist plots of integrated optimizations using the proposed method, for different numbers of sensor positions N_{pos} . For the first two Nyquist plots, the local circle approximations are also shown.

Using the proposed procedure, integrated optimizations are successfully performed for different numbers of sensor positions $N_{\text{pos}} = 1, 3, 6$. The designs and corresponding Nyquist plots are shown in Fig. 4.10. Mechanism-like structures can clearly be identified in the designs. The Nyquist plots show that all the designs meet the requirements on closed-loop stability and modulus margin. However, not all designs contain binary zero-and-one densities that can directly be interpreted. Especially the design for one sensor position ($N_{\text{pos}} = 1$) contains large areas with intermediate densities. The design with six sensor

positions also contains some areas with intermediate densities. This might be functionally interpreted as a ‘rubber band’ with a specific stiffness to tune the system dynamics.

Table 4.2: Performance overview of the sequential and multiple integrated optimizations.

Units: rad/ms	N_{pos}	Bandwidth		Eigenfrequency		
		ω_b	Ω_1	Ω_2	Ω_3	
Sequential	1, 3, 6	1.11	11.5	22.0	26.4	
Integrated	1	3.94	5.66	8.08	11.4	
Integrated	3	3.86	5.23	8.60	16.4	
Integrated	6	3.52	5.70	10.3	14.6	

An overview of the achieved performance, as compared to the sequentially optimized design, is shown in Table 4.2. All the designs optimized with the integrated approach have a bandwidth about a factor 3.5 higher than the design optimized for eigenfrequencies. Moreover, the eigenfrequencies are significantly lower for the integrated optimizations, which clearly demonstrates that the system with the highest bandwidth does not necessarily need maximized eigenfrequencies.

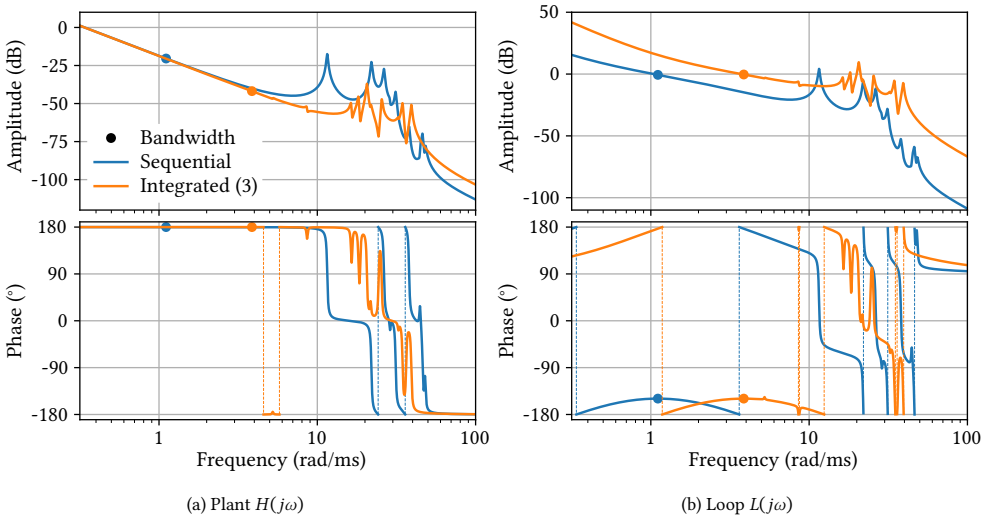


Figure 4.11: Bode plots for the plant $H(j\omega)$ and loop gain $L(j\omega)$, comparing the sequentially optimized design with the integrated optimized design for $N_{\text{pos}} = 3$. Only the response of sensor position 1 is shown.

The integrated approach is able to achieve a high bandwidth, relatively close to the eigenfrequencies. This can be explained using the Bode diagrams in Fig. 4.11, in which the dynamic response of the design optimized for integrated performance with $N_{\text{pos}} = 3$ is shown. The first eigenmode creates a resonance peak with a very small amplitude, around 5.2 rad/ms. This small amplitude means that the actuator is unable to ‘affect’ this mode and/or it cannot be ‘seen’ by the sensor (*i.e.* uncontrollable and/or unobservable). For the controller it seems as if this mode does not exist, therefore it is not limiting bandwidth.

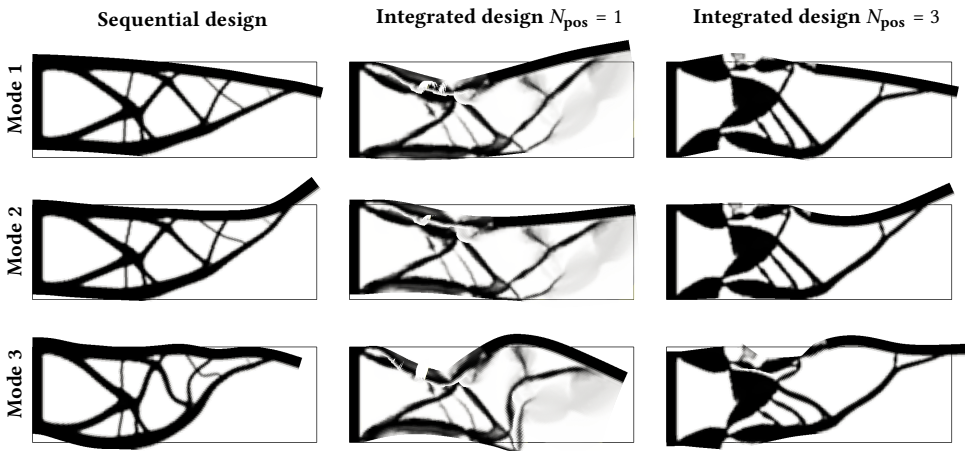


Figure 4.12: Comparison of the first three mode shapes for several designs. The outline of the domain in the undeformed situation is indicated.

Inspecting the mode shapes of the integrated designs in Fig. 4.12, this effect can clearly be seen. For some modes, the actuator is virtually at a standstill, meaning that the mode is not excited by the actuator. For other modes, the location corresponding to the sensor is at a standstill, which means the sensor does not measure the mode.

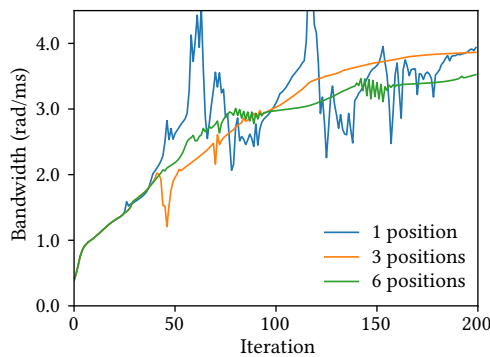


Figure 4.13: Convergence history of the bandwidth for the three integrated optimizations.

The convergence history of the three designs is shown in Fig. 4.13. Especially the design for $N_{\text{pos}} = 1$ shows significant oscillations. In the Nyquist curves of subsequent design iterations shown in Fig. 4.14, the circle corresponding to the first eigenfrequency flips its direction. This flipping is caused by the actuator or sensor displacement crossing zero and changing sign. Since the modes have a very small excitation amplitude (Fig. 4.12), the controller is able to attain a very high gain. A small variation in the design then causes a small change in the mode shape, which eventually has a large effect on the system, due to the high control gain. The designs for 3 and 6 sensor positions exhibit less oscillations and

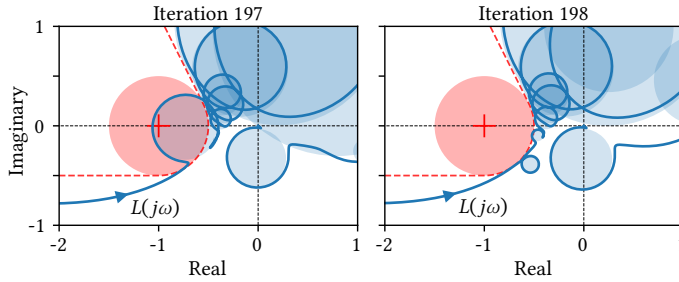


Figure 4.14: Nyquist plots showing the oscillatory behavior of integrated optimization for $N_{\text{pos}} = 1$.

4

a smoother convergence. Due to the addition of multiple sensor locations, the complexity of the optimization problem is increased and involves more trade-offs, leading to designs which are less sensitive to small variations.

4.5.4 Comparison with explicit peak constraint

To demonstrate the added value of proposed method, also an optimization based on the method of [Van der Veen et al. \(2015, 2017\)](#) is implemented. First, the frequencies corresponding to peaks in the sensitivity function are numerically located in each design iteration, after which they are used as constraints. Additionally, an explicit constraint ensuring closed-loop stability must be added, to prevent the Nyquist curve from encircling the -1 point. This is done by limiting the (smooth) maximum of all real parts of the closed loop poles below zero, thus ensuring all poles are in the left half plane. We refer to the original publications for the full description, as our interest here is primarily in the comparison with the proposed approach.

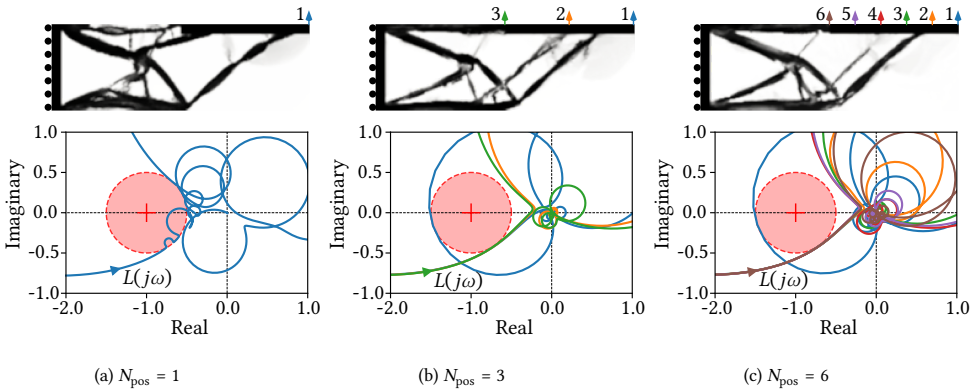


Figure 4.15: Resulting designs and Nyquist plots of integrated optimizations explicitly constraining the peaks of the sensitivity function $|S(j\omega)|$ ([Van der Veen et al., 2015, 2017](#)), for different numbers of sensor positions.

The results of the optimization based on the method by [Van der Veen et al. \(2017\)](#) are shown in Fig. 4.15. Although a structure may be recognized in the designs, the structural features look rather irregular and contain substantial amounts of intermediate densities.

The design considering one actuator position faces similar convergence issues as the proposed integrated optimization (Fig. 4.10a), where small changes in design and mode shape cause oscillations. Also for multiple sensor positions, the optimization results in infeasible designs. During the design iterations, one of the Nyquist curves loops around the -1 point, indicating closed-loop instability (Figs. 4.15b and 4.15c). In this situation, two constraints are conflicting: the stability constraint requires the Nyquist curve to pass on the right side of the -1 point, but the peak constraint prevents this by requiring the curve to stay outside the circular margin. A change of design or bandwidth will thus violate at least one of the constraints, making it difficult to escape this situation. The proposed method does not face these issues, as stability is ensured implicitly by the geometric nature of the constraints on the Nyquist curve in combination with local circle approximations.

4.5.5 Robust formulation

For the application of the robust formulation to the proposed integrated optimization, the effect of the robust parameter η is studied first. This parameter controls the amount of dilation or erosion of the design. Both the eigenfrequencies and the distances from the circle approximations to the -1 point change as a function of η , as is shown in Fig. 4.16. Here, a distinction is made between the responses when approximated using the nominal eigenmodes, as explained in Section 4.4.4, and evaluated exactly using eigenmodes corresponding to the perturbed designs. As can be expected, the error between the exact and approximated responses deviates more as the design is perturbed further away from the nominal design at $\eta = 0.5$.

Another observation that can be made in Fig. 4.16, is the fact that the distances to the -1 point are not monotonically increasing or decreasing, as is the case for compliance problems (Sigmund, 2009). The lack of a monotonic behavior means that the worst-case design is not necessarily coinciding with extreme values of η . In this work, a value of $\eta = 0.5 \pm 0.05$ is used, for which it can be assumed that the worst-case performance is likely to be included by evaluating three designs, at $\eta = 0.45, 0.5$, and 0.55 . However, for larger perturbations and given the non-monotonic behavior, evaluation of the worst-case performance might require more than three designs to be analyzed.

For the robust optimization procedure, the edge contrast parameter β is gradually increased from 1.0 to 20.0 during design iterations 50-180. Also, a filter radius of 8 elements is used to ensure a large minimum feature size.

The resulting designs of the robust integrated optimizations, using the proposed method, are shown in Fig. 4.17. All designs have clear boundaries between void and material, which is a characteristic property of the robust formulation. At some locations, hinges appear with intermediate densities to provide a low-stiffness connection. As for their performance, the design with one sensor position achieves a bandwidth of $\omega_b = 3.5$ rad/ms, and the two other designs a bandwidth of 1.9 rad/ms. A design robustly optimized for maximum eigenfrequencies, with similar settings, is found to achieve a bandwidth of 1.1 rad/ms. This means the performance increase of robust integrated optimization is still significant.

Although the bandwidth of the design with one sensor position is very high, its disturbance rejection requirement is not met, as can be seen in Fig. 4.19a. This can again be explained by the dynamic response being very sensitive to (small) design variations. For

Figure 4.16: Comparison of the effect of robust parameter η on the eigenfrequencies (top) and distances from selected circles to the -1 point (bottom), for a robust eigenfrequency optimized design. The approximated response (Eq. 4.42) is compared with the exact solution (dashed lines). A value of $\beta = 20$ is used and a filter radius of 5 elements.

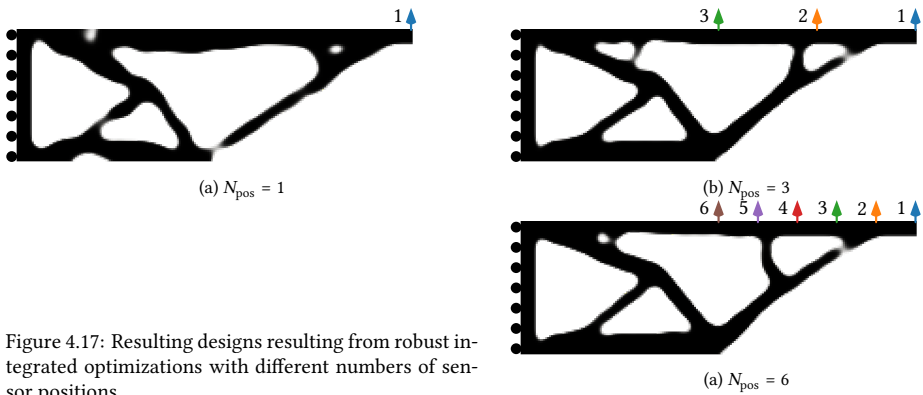
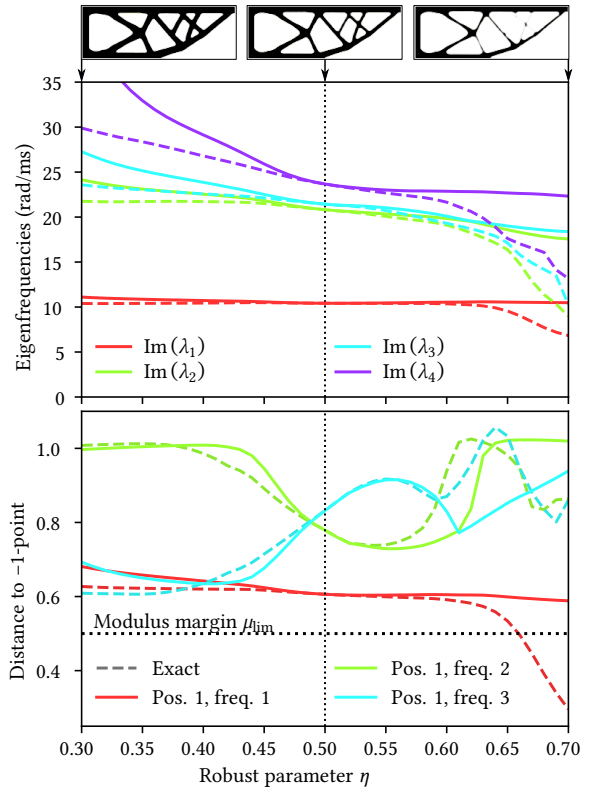


Figure 4.17: Resulting designs resulting from robust integrated optimizations with different numbers of sensor positions.

the designs optimized with 3 (Fig. 4.19b) and 6 sensor locations, the disturbance rejection requirements are satisfied for all three design perturbations and at all sensor locations.

The convergence properties are also improved using the robust formulation, as is seen in Fig. 4.20. Small oscillations are still present, but significantly less than without the robust formulation (Fig. 4.13). A lower final bandwidth is attained for all designs, compared

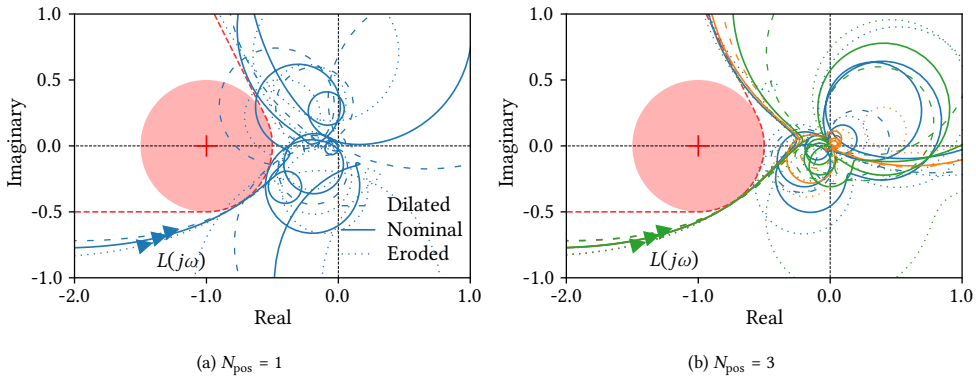


Figure 4.19: Nyquist plots corresponding to different robustly optimized designs.

to the results from optimizations without the robust formulation. However, this is counterbalanced with an increased robustness against geometric perturbations and the added control on minimum feature size.

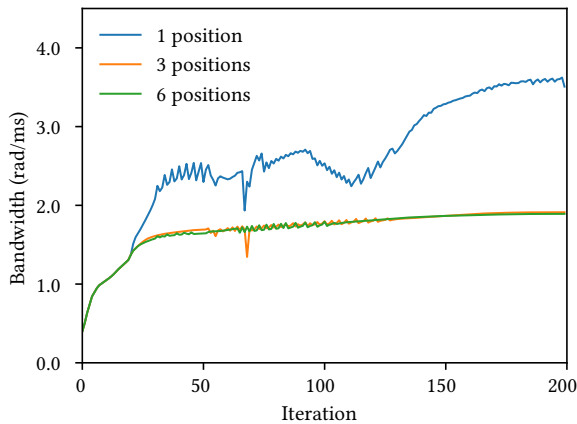


Figure 4.20: Convergence history of the bandwidth for the three robustly integrated optimizations.

The time required for this optimization using the approximated robust formulation is 55 minutes. The same optimization without robust formulation requires 49 minutes in total. This is for a total of 200 design iterations and 3 sensor positions, on a standard corporate laptop with an Intel Core i7-6600 processor. The difference of 6 minutes (12% extra calculation time) is required for the Heaviside projections, approximation of perturbed eigenmodes, and analysis of the reduced-order model for the local approximations. This is significantly less than the factor 3 that would be required without the proposed method approximating the eigenmodes for the perturbed designs.

4.6 Discussion

In the numerical examples, no issues with severe mode interaction and ill-fitting local approximations are encountered during the optimizations, which were initially identified as potentially harmful for the optimization (Fig. 4.5). The current work is focused on monolithic structures made out of metal, with a low damping coefficient ζ . Mode interaction might increase for applications with higher damping, which might lead to issues in convergence. More research is required into the effect of damping and mode interaction on the optimization.

In the examples, a discrete number of sensor positions is used to account for position-dependent dynamics. However, position dependency occurs over a continuous line or even a surface in reality. The current implementation ensures accuracy at several locations, but it does not account for any other locations also requiring accurate positioning. Even when locations may not be sensed, their accuracy may still be important to consider in the design of a motion system.

Moreover, the inclusion of an increasing number of sensor positions leads to a growth in the number of constraints for the optimization. As eigenmode design sensitivities are required for each constraint, this directly increases computational cost. Therefore, future research should focus on methods to include many sensor locations without excessive computational cost.

The presented framework potentially allows for frequency-dependent constraints. This could be used, for instance, to incorporate more stringent limitations on high-frequency eigenmodes. Another possibility is to include the influence of time delay in the control loop, which has a frequency-dependent effect on the phase. Following the same approach based on the Nyquist curve could allow for consideration of this effect.

In reality, many systems are MIMO, for which the methods presented in the current work may also be used (e.g. sequential loop closing (Skogestad and Postlethwaite, 2001)). However, for a coupled MIMO system multiple loops interact with each other, which requires further analysis of closed-loop behavior. This is done in the method of Van der Veen *et al.* (2017), but it requires additional constraints and thus significantly more computational time. Efficient extension to MIMO systems therefore remains an open issue for future research.

4.7 Conclusion

A novel approach to integrated controller-structure topology optimization is proposed. It builds on a flexible framework enabling local approximation of the Nyquist curve using circular shapes. These circles allow analytical formulation of constraints in the complex domain, making them suitable for gradient-based optimization. In this manuscript, the approximating circles are used to constrain the Nyquist curve in an integrated controller-structure optimization, thus enforcing closed-loop stability and disturbance rejection properties. The approach is general and can be extended to other control objectives that can be expressed by the Nyquist curve.

From the numerical examples, it can be seen that the proposed method is able to greatly improve system performance. For the studied problem, the state-of-the-art method in literature (Van der Veen *et al.*, 2015) is not able to converge to feasible designs due to

conflicting stability and disturbance rejection constraints. In the proposed method, this problem does not occur as stability and disturbance rejection are ensured simultaneously by geometrical restriction of the Nyquist curve. Using numerical examples, the integrated optimization achieves improvements up to 350% in terms of bandwidth compared to sequential optimization, while ensuring a sufficient modulus margin.

Also position-dependent dynamics is considered, by the addition of constraints on the SISO Nyquist curves for multiple sensor positions. Not only does this lead to a structure and controller that can be used at each of the sensor locations, it also improves convergence properties of the optimization. Optimizing for only one sensor position results in designs that are very sensitive to small variations in mode shape around the actuator and sensor positions, leading to severe oscillations. By optimizing for multiple sensor locations, this detrimental effect is noticeably reduced.

Furthermore, a computationally efficient robust formulation is introduced, approximating the dynamics of the eroded and dilated designs. It allows for analysis and optimization of perturbed designs without significant additional computational cost, instead of a threefold increase using the conventional approach. The validity of the approximation is demonstrated for small design perturbations. For larger design perturbations extra care is required, because non-monotonic behavior is observed for the modulus margins, potentially resulting in interior worst cases for robust optimization. Using the proposed formulation, the obtained designs are more robust against geometric deviations, a length scale is imposed, and a positive effect on optimization convergence is observed. Furthermore, the approximation-based robust formulation is not limited to the current application, but may also be used for other types of topology optimization involving dynamics.

There are several gaps to bridge in order to arrive at real-world systems with ultimate performance, such as incorporation of time delay, MIMO control, ensuring accuracy over large surfaces, and further reduction of computational effort. Despite the remaining challenges, this work provides a step forward in computational design methods for next generation high-precision motion systems.

5

Large-scale integrated optimization for MIMO

5

The design of high-precision motion systems is challenging, because it involves the interaction between system dynamics and MIMO closed-loop control. This makes topology optimization a promising design method in this field. In this work, focus is on the simultaneous optimization of controller and topology for large-scale 3D problems and MIMO control, where the aim is to increase bandwidth while ensuring a robustness margin on disturbance rejection properties. Based on local approximations of the \mathcal{H}_∞ norm, constraints can be formed that ensure rejection of combined disturbances in MIMO systems. Furthermore, to reduce computation time spent on design sensitivities, the eigenmode adjoint systems of equations are solved approximately using a reduced-order model. Using 3D examples with control in 6 degrees of freedom, designs are generated with bandwidths over 150% higher compared to designs optimized for maximum eigenfrequencies, while satisfying requirements on the \mathcal{H}_∞ norm. Next to this, the local approximations provide a natural way to aggregate the MIMO behavior, thus reducing the number of constraints by a factor 6. Finally, the approximation of eigenmode design sensitivities significantly reduces the computation time by more than two orders of magnitude, while keeping sufficient accuracy for an effective optimization. The methods presented enable the 3D integrated controller-structure topology optimization for MIMO in an efficient and effective manner, providing new possibilities for the design of motion systems with superior performance.

5.1 Introduction

Topology optimization is a promising tool for the design of high-precision motion systems (Van der Veen *et al.*, 2017; Delissen *et al.*, 2022), such as those found in semiconductor equipment, microscopy, robotics, and medical devices. The design of such systems is challenging as it involves both dynamics and control (Munnig Schmidt *et al.*, 2011; Oomen, 2018). Performance of a motion system is typically characterized by the bandwidth, which is the frequency up to which a reference signal can be tracked. A higher bandwidth thus means the ability to operate at higher speeds. However, an increase of bandwidth comes at the cost of increased sensitivity to disturbances. These disturbances may be due to vibrations from the environment, measurement noise, or imperfections of the system, and can cause stability issues or reduce accuracy. Achieving a high bandwidth with sufficient disturbance rejection requires careful design of the integrated system (Munnig Schmidt *et al.*, 2011). Moreover, many positioning systems operate in multiple degrees of freedom, requiring MIMO control. This makes the design even more challenging, as the performance and disturbance rejection requirements must be satisfied simultaneously in multiple directions (Skogestad and Postlethwaite, 2001).

To enable the automatic generation of motion system designs, while satisfying integrated system requirements, topology optimization is a prime candidate due to its large design freedom. Performance of motion systems is typically specified in the frequency domain, as it allows for straightforward quantification of system accuracy (Munnig Schmidt *et al.*, 2011). Relatively few studies into integrated controller-structure topology optimization in the frequency domain are found in literature. Albers and Ottnad (2010) consider both a topology optimization and a PID controller for a SISO system, but not in an integrated way, as the objective for the structure (stiffness) does not directly relate to the controlled system performance. Providing a framework for truly integrated controller and large scale topology optimization for MIMO systems is the aim of this work. Before discussing our approach and contributions, we review the relevant state of the art on this topic.

5.1.1 State of the art

Van der Veen *et al.* provide a truly integrated topology optimization formulation, first for SISO systems 2015, and later also for MIMO 2017. In their MIMO approach, all peak amplitudes of the diagonal entries of the *sensitivity function* are constrained, thus ensuring robustness for disturbance rejection of the individual input and output pairs. The sensitivity function for MIMO systems $\mathbf{S}(j\omega)$ transfer function between disturbances \mathbf{d} to outputs \mathbf{y} , dependent on complex frequency $j\omega$ (Fig. 5.1). It characterizes the sensitivity of a closed-loop system to disturbances and also robustness against relative plant model errors (Skogestad and Postlethwaite, 2001). The amplitudes of the entries $|S_{ij}(j\omega)|$ quantify the disturbance rejection properties, which must be limited below a threshold to ensure robustness against disturbances. As the sensitivity function is multi-modal and may have peaks at multiple frequencies, separate constraints are imposed on individual peaks. Only limiting the diagonal entries $|S_{ii}|$, as is done by Van der Veen *et al.* (2017), does not consider the combined disturbances and interactions between the different controlled degrees of freedom. When a disturbance enters one loop, it may have detrimental effects on another loop through the interactions of $S_{ij}(j\omega)$ (Skogestad and Postlethwaite, 2001).

To enable large-scale topology optimization, it is important to consider computational effort. The system dynamics are commonly captured using a reduced model in motion system design, usually by including a truncated series of eigenmodes (Munnig Schmidt *et al.*, 2011; Besselink *et al.*, 2013; Van der Veen *et al.*, 2017). After constructing the reduced-order model, it reduces the computational effort required for evaluation of the sensitivity function $\mathbf{S}(j\omega)$. However, it requires additional effort to calculate the design sensitivities of the associated constraints. These are needed for the gradient-based optimization methods on which topology optimization relies (Svanberg, 1987). Each constraint involving the sensitivity function requires evaluation of (adjoint) design sensitivities for each eigenmode included in the reduced system (Lee, 1999; Van der Veen *et al.*, 2017). This results in extensive computation time as each adjoint design sensitivity requires the solution of a large linear system of equations. The total computation time thus rapidly grows when including many constraints and/or many eigenmodes, hampering the application to topology optimization in 3D.

Straightforward limitation of all entries of the sensitivity function with the method of Van der Veen *et al.* (2017) leads to a quadratic growth of the number of constraints, as a function of the number of inputs and outputs of the system. This growth is even larger in case multiple sensor positions are included to account for position-dependent dynamics, which is a common requirement in motion systems. Due to the computational effort required for these constraints, this is deemed an infeasible approach.

Alternatively, the disturbance rejection properties for MIMO systems can be quantified using the maximum singular value of the sensitivity function $\bar{\sigma}(\omega) = \bar{\sigma}(\mathbf{S}(j\omega))$ (provided the closed-loop system is stable). This provides an upper bound to the combined output \mathbf{y} due to combined disturbances \mathbf{d} (Figs. 5.1 and 5.2). Instead of having to constrain all separate entries of $|S_{ij}(j\omega)|$ as in the aforementioned approach, only one scalar value needs to be limited. Considering all frequencies, the worst-case maximum singular value $\bar{\sigma}(\omega)$ is captured by the \mathcal{H}_∞ norm. This quantity is often used to determine the robustness properties of a MIMO system (Skogestad and Postlethwaite, 2001).

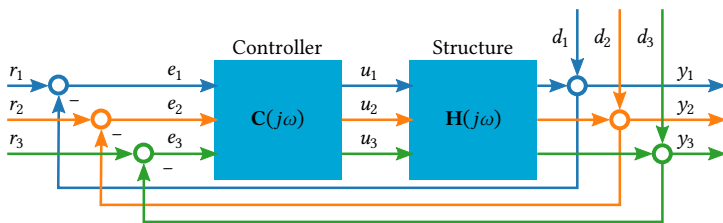


Figure 5.1: A MIMO system, where controller and structure are placed in feedback loops. The system is designed for the outputs \mathbf{y} to track the reference signals \mathbf{r} and to reject disturbances \mathbf{d} . Based on the measured error \mathbf{e} , the controller $\mathbf{C}(j\omega)$ determines the correction signal \mathbf{u} . The plant $\mathbf{H}(j\omega)$ contains couplings between the different degrees of freedom.

In literature, the \mathcal{H}_∞ norm is also used as an objective for topology optimization considering uncertain loads for a MIMO dynamic compliance problem (Venini, 2019). However, this approach has two severe drawbacks. First, it requires significant computation power to numerically find the \mathcal{H}_∞ norm, as the transfer function (*i.e.* $\mathbf{S}(j\omega)$) needs to

be sampled many times and no reduced-order model or modal truncation is used. Second, the max-max nature of the \mathcal{H}_∞ norm may cause issues with non-differentiability. As the maximum singular value $\bar{\sigma}(\omega)$ may reach extreme values at multiple frequencies, each candidates for the \mathcal{H}_∞ norm, multi-modal behavior is observed (Fig. 5.2). However, only the largest peak is marked as the \mathcal{H}_∞ norm and minimized. In case multiple peaks of $\bar{\sigma}(\omega)$ reach equal maximum values at different frequencies, as can be expected when an upper limit is imposed, the \mathcal{H}_∞ norm becomes non-differentiable. Additionally, the maximum singular value of a single peak may present a second source of non-differentiability when two (or more) singular values coincide as the maximum. The numerical calculation of gradient information might not be the direct issue, but the discontinuities in gradient information can potentially lead to significant oscillations in the gradient-based optimization process, thus hampering convergence (e.g., as seen in [Zhu et al., 2003](#)). As will be discussed below, in this paper we propose an approach to overcome these difficulties, and enable constraints on the \mathcal{H}_∞ norm suitable for gradient-based optimization.

5

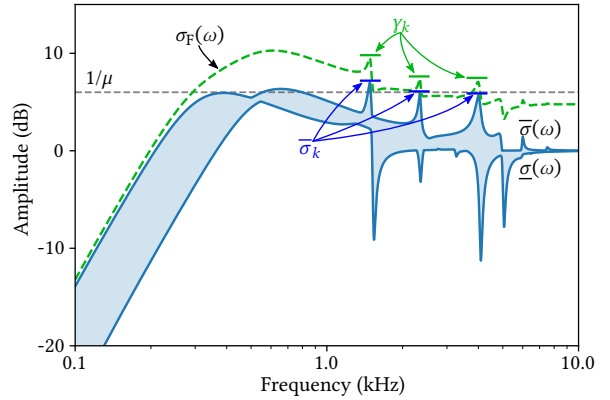


Figure 5.2: Figure showing the smallest ($\underline{\sigma}(\omega)$) and largest ($\bar{\sigma}(\omega)$) singular values of the sensitivity function $\mathbf{S}(j\omega)$. Also the the Frobenius norm $\sigma_F(\omega)$ and local approximations are illustrated.

Other literature focused on the tuning of controllers only, where the \mathcal{H}_∞ norm is constrained in gradient-based optimization, e.g., [Karimi and Galdos \(2010\)](#); [Van Solingen et al. \(2018\)](#), impose constraints on a discrete grid of sampling points. This avoids the multimodality over the frequency range. However, many constraints in a fixed frequency grid are required to capture the extreme values, which is infeasible for topology optimization due to the computational effort required for the adjoint design sensitivities of each constraint.

5.1.2 Contributions

In this work, a framework is presented that enables large-scale 3D topology optimization of MIMO systems. This is achieved by both limiting the number of constraints required and reducing the computational effort needed for each constraint. Furthermore, the proposed approach aims to reduce the impact of multimodality on optimization convergence. Three main contributions can be distinguished:

1. A MIMO constraint formulation based on local approximations of the \mathcal{H}_∞ norm, suitable for gradient-based optimization.

2. Approximation of eigenmode design sensitivities using an augmented reduced model.
3. Application to integrated 3D controller and topology optimization.

Without going into full detail, we here outline the followed approaches.

Approximation of the H_∞ norm Using a double approximation of the \mathcal{H}_∞ norm with an adaptive correction scheme avoids non-differentiability and multi-modality. First, the maximum singular value is approximated over all frequencies using the Frobenius norm. This provides an analytical and differentiable upper bound of the maximum singular value $\bar{\sigma}(\omega)$ using all entries of the sensitivity function $\mathbf{S}(j\omega)$. Next, local approximations are constructed for $\mathbf{S}(j\omega)$ around each closed-loop pole frequency of the system. This provides an upper bound of the local \mathcal{L}_∞ norm to the Frobenius norm, for a frequency interval close to each closed-loop pole frequency. Finally, the approximation is corrected to enable exact limitation of the local \mathcal{L}_∞ norms. This is done based on the exactly calculated (non-differentiable) \mathcal{L}_∞ norm of the maximum singular value $\bar{\sigma}(\omega)$ in a frequency interval close to the characteristic frequency. This both makes the number of constraints independent on the number of in- and outputs, and prevents issues with non-differentiability.

In Chapter 4, local approximations were used to account for multi-modality of the sensitivity function (in the form of the Nyquist curve and the modulus margin). This idea is inspired by the work of [Tacx and Oomen \(2021\)](#), who use local models based on rational functions to locally approximate the \mathcal{H}_∞ norm in multiple finite-frequency intervals when limited data is available. Here, we propose to extend the local circle approximations introduced in Chapter 4 towards MIMO systems and the \mathcal{H}_∞ norm.

Approximation of eigenmode design sensitivities The calculation time required for the eigenmode design sensitivities is mainly determined by the solution of an adjoint system of equations. To reduce the calculation time, the solution is approximated using a reduced-order basis. We demonstrate that a modal truncated basis, as is used for the analysis of the system dynamics, does not provide sufficient accuracy. Therefore, the basis is augmented with a new set of Krylov vectors in each design iteration, enhancing the accuracy of the approximate solution. Calculation of the augmented Krylov vectors is significantly less time-consuming as compared to explicitly solving the adjoint systems.

Reduced-order models based on Krylov vectors are commonly used to interpolate transfer functions, with accurate input-output behavior ([Besselink et al., 2013](#)). In Chapter 3, it has been shown that augmentation with a quasi-static correction vector significantly improves the quality of the design sensitivities. Here, that idea is extended to MIMO and further generalized to enhance accuracy at low computational cost.

Integrated 3D motion system optimization The proposed contributions are applied to integrated controller and topology optimization for a motion system in the frequency domain. The case of a magnetically levitating motion stage is used to demonstrate the method, which is able to move in 6 degrees of freedom. For the control of the LTI MIMO system, a fixed structure diagonal PID controller is used. Next to a constraint on the disturbance rejection properties (using the approximate \mathcal{H}_∞ norm), an additional constraint is used to enforce closed-loop stability. Especially the 3D application is challenging, not only because control is required in 6 degrees of freedom, but also because both the number and calculation time of relevant eigenmodes increases. With this demonstration of the pro-

posed methods, we show that the computational effort lowered such that optimization of industry-relevant motion stages is within reach.

This chapter is structured as follows. First, in Section 5.2, all steps towards the approximation of the \mathcal{H}_∞ norm for a MIMO system are presented. In Section 5.3, the modeling aspects on both the mechanical and control side are explained in detail, specifically for the intended application of a motion stage with multiple rigid body modes. Next, Section 5.4 presents a method to efficiently calculate adjoint eigenvector design sensitivities, enabling optimization with large scale finite-element models. The effectiveness of the proposed methods is demonstrated in Section 5.5, where results for both 2D and 3D topology optimization cases are presented. Finally, discussion and conclusions are given in Sections 5.6 and 5.7, respectively.

5.2 Approximation of the H_∞ -norm

5.2.1 H_∞ norm

The disturbance rejection properties for a MIMO system are characterized by the (output) sensitivity function

$$\mathbf{S}(j\omega) = (\mathbf{I} + \mathbf{L}(j\omega))^{-1}, \quad (5.1)$$

where $\mathbf{L}(j\omega) = \mathbf{H}(j\omega)\mathbf{C}(j\omega)$ is the open loop gain with n inputs and outputs, and $\mathbf{S} \in \mathbb{C}^{n \times n}$. This is the transfer function between the disturbances \mathbf{d} and the system output \mathbf{y} (Fig. 5.1).

The ability to reject disturbances (in case of a stable closed-loop system) for MIMO is related to the singular values of $\mathbf{S}(j\omega)$. These provide bounds on the amplification of combined disturbances \mathbf{d} on the system output $\mathbf{y} = \mathbf{S}(j\omega)\mathbf{d}$ as

$$\underline{\sigma}(\omega) \leq \frac{\|\mathbf{S}(j\omega)\mathbf{d}\|_2}{\|\mathbf{d}\|_2} \leq \bar{\sigma}(\omega) \quad \forall \quad \|\mathbf{d}\|_2 \neq 0, \quad (5.2)$$

where $\underline{\sigma}(\omega)$ and $\bar{\sigma}(\omega)$, respectively, are the lowest and highest singular values of $\mathbf{S}(j\omega)$ (Skogestad and Postlethwaite, 2001). These bounds are shown in Fig. 5.2. Note that for SISO systems, the maximum and minimum singular values simply reduce to the amplitude of the transfer function $\underline{\sigma}(\omega) = \bar{\sigma}(\omega) = |S(j\omega)|$.

The worst case value for disturbance rejection corresponds to the maximum $\bar{\sigma}$ over all frequencies. This is defined as the \mathcal{H}_∞ norm (Skogestad and Postlethwaite, 2001)

$$\|\mathbf{S}\|_\infty = \max_\omega \bar{\sigma}(\omega). \quad (5.3)$$

It is the aim to limit this value below a given threshold

$$\|\mathbf{S}\|_\infty \leq \frac{1}{\mu}, \quad (5.4)$$

which for a SISO system is identical to ensuring a modulus margin μ . Note that this measure does not provide information on closed-loop stability, for which the closed-loop poles are used (Van der Veen *et al.*, 2017).

The \mathcal{H}_∞ norm thus signifies the largest maximum singular value over all frequencies in the form

$$\|\mathbf{S}\|_\infty = \max_{\omega} \{\max\{\sigma_1(\omega), \dots, \sigma_n(\omega)\}\}, \quad (5.5)$$

where $\sigma_i(\omega)$ represent all the singular values of $\mathbf{S}(j\omega)$. For gradient-based optimization, this max-max operation is troublesome to incorporate, since the maximum operator is non-differentiable when multiple of its arguments are equal.

5.2.2 Frobenius norm

To avoid the inner maximum operator, the maximum singular value $\bar{\sigma}(\omega)$ can be approximated using a differentiable operation. This is done using the Frobenius matrix norm (Golub and van Loan, 1996), defined as

$$\sigma_F(\omega) = \|\mathbf{S}(j\omega)\|_F = \sqrt{\sum_{i=1}^n \sum_{j=1}^n |S_{ij}(j\omega)|^2}. \quad (5.6)$$

The Frobenius norm aggregates all the entries of the sensitivity matrix $\mathbf{S}(j\omega)$ into one single value, independent on the number of inputs and outputs. An alternative equivalent definition of the Frobenius norm is given as (Golub and van Loan, 1996)

$$\sigma_F(\omega) = \sqrt{\sum_{i=1}^n \sigma_i(\omega)^2}, \quad (5.7)$$

using the individual singular values $\sigma_i(\omega)$ of the matrix $\mathbf{S}(j\omega)$. From an optimization perspective, this can be recognized as the widely used p-norm of the singular values (with $p = 2$), thus approximating the maximum singular value.

The Frobenius norm provides analytical bounds to the maximum singular value of matrix as (Golub and van Loan, 1996)

$$\frac{1}{\sqrt{n}} \sigma_F(\omega) \leq \bar{\sigma}(\omega) \leq \sigma_F(\omega), \quad (5.8)$$

which are indicated in Fig. 5.2. In contrast to the maximum singular value, the Frobenius norm (Eq. 5.6) is differentiable, making it suitable for use in gradient-based optimization.

Combining Eqs. 5.3 and 5.8, using the Frobenius norm to bound the \mathcal{H}_∞ norm over all frequencies ω as

$$\frac{1}{\sqrt{n}} \max_{\omega} \sigma_F(\omega) \leq \|\mathbf{S}\|_\infty \leq \max_{\omega} \sigma_F(\omega). \quad (5.9)$$

However, the maximum operation over all frequencies is still present, and is non-differentiable when multiple equal maximum peaks occur. For this, we propose a divide-and-conquer strategy.

5.2.3 Local circle approximation

To avoid non-differentiability and multi-modality over the entire frequency range ω , the maximum Frobenius norm is approximated over smaller frequency ranges using local circle approximations. In the previous Chapter 4, local circle approximations were introduced to approximate the Nyquist curve of the open-loop response $L(j\omega)$. By analytical

fitting characteristic circular features to the Nyquist curve, the use of efficient geometric constraints is enabled in the complex plane.

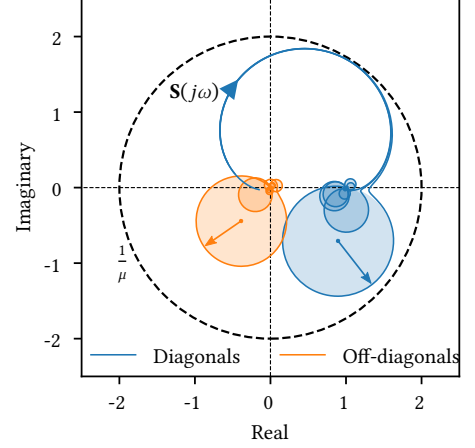


Figure 5.3: Nyquist plot of an arbitrary sensitivity function $\mathbf{S}(j\omega) \in \mathbb{C}^{3 \times 3}$, with several fitted circles indicated. Also the limit of $1/\mu$ is indicated.

5

Like the Nyquist curve, the closed-loop sensitivity function $\mathbf{S}(j\omega)$ also contains characteristic circles, which can be seen in the Nyquist diagram in Fig 5.3. These circles are caused by the mechanical eigenmodes, which are still present in the closed-loop system, even though their poles are shifted due to the loop closing. Using the same procedure as presented in Chapter 4, local approximations are made for each flexible eigenmode k in the system as

$$\mathbf{S}(j\omega) \approx \check{\mathbf{S}}_k + \frac{\mathbf{P}_k}{j\omega - \xi_k} \quad \text{for } \omega \approx \text{Im}(\xi_k), \quad (5.10)$$

where ξ_k are the closed-loop system poles and \mathbf{P}_k matrices of participation factors. Further details on how to calculate these can be found in Chapter 4. The constant offset matrices $\check{\mathbf{S}}_k$ are calculated as

$$\check{\mathbf{S}}_k = \mathbf{S}(j\text{Im}(\xi_k)) + \frac{\mathbf{P}_k}{\text{Re}(\xi_k)}. \quad (5.11)$$

As seen in Chapter 4, this corresponds exactly to circles with midpoints and radii, respectively, being

$$X_{ijk} = \check{S}_{ijk} - \frac{P_{ijk}}{2\text{Re}(\xi_k)} \quad \text{and} \quad R_{ijk} = \frac{|P_{ijk}|}{2\text{Re}(\xi_k)}, \quad (5.12)$$

where the indices denote output i , disturbance input j , and mode k . Note that $\text{Re}(\xi_k) < 0$ is required for closed-loop stability, which means the radii and midpoints are finite values.

From Eq. 5.6, it can be deduced that the local maximum Frobenius norm occurs at a frequency where the individual amplitudes of the sensitivity function $|S_{ij}(j\omega)|$ are large. Using the introduced circle approximations, the maximum amplitudes of the sensitivity functions in the vicinity of $\omega \approx \text{Im}(\xi_k)$ can be approximated as

$$\max_{\omega \approx \text{Im}(\xi_k)} |S_{ij}(j\omega)| \approx |X_{ijk}| + R_{ijk}. \quad (5.13)$$

However, the maximum amplitudes of the individual $|S_{ij}(j\omega)|$ do not necessarily coincide at one frequency, preventing the calculation of an exact upper bound. Using the approximation of Eq. 5.13, the local maximum Frobenius norm is now (approximately) bounded by γ_k as

$$\max_{\omega \approx \text{Im}(\xi_k)} \sigma_F(\omega) \lesssim \gamma_k. \quad (5.14)$$

By combining Eqs. 5.6 and 5.13, the approximate upper bound is calculated as

$$\gamma_k = \sqrt{\sum_{i=1}^n \sum_{j=1}^n (|X_{ijk}| + R_{ijk})^2}. \quad (5.15)$$

Through the bounds provided in Eq. 5.8, the value γ_k thus also provides an approximate upper bound for the local \mathcal{L}_∞ norm of $\bar{\sigma}$ for frequencies close to $\text{Im}(\xi_k)$ as

$$\max_{\omega \approx \text{Im}(\xi_k)} \bar{\sigma}(\omega) \lesssim \gamma_k. \quad (5.16)$$

Note that γ_k is only non-differentiable when $|X_{ijk}| = 0$, or when $|P_{ijk}| = 0$. For the numerical examples presented in Section 5.5, this did not cause any issues. In case it does cause issues, the absolute value can simply be approximated by a continuously differentiable function, e.g., $|x| \approx \sqrt{|x|^2 + \varepsilon}$ with a small value ε .

5.2.4 Adaptive correction factor

Knowing only the approximate upper bounds γ_k is not sufficient for the current optimization purpose of limiting the \mathcal{H}_∞ norm, which must be constrained to an exact value of $1/\mu$. Therefore, an adaptive correction factor is used to improve the accuracy of the approximation. This is inspired by an existing formulation for topology optimization that includes constraints on maximum stress value, by [Le et al. \(2010\)](#). In their work, a smooth maximum stress is computed aggregating all stresses in the domain, using the p-norm. For the optimization problem an exact limit is required on the maximum stress, but the p-norm overestimates the maximum stress value. Therefore, a correction factor is introduced to normalize the aggregated stress measure used in the constraint, in order to match the exact maximum stress value. This correction factor is adapted during the design iterations, and stabilizes as the optimization progresses with smaller and smaller design changes.

This concept can also be applied here, by introducing a correction factor a_k such that

$$\bar{\sigma}_k = a_k \gamma_k, \quad (5.17)$$

in which the correction factor is approximately bounded as $1/\sqrt{n} \lesssim a_i \lesssim 1$, according to the bounds that the Frobenius norm provides in Eq. 5.8. The variable $\bar{\sigma}_k$ denotes the maximum singular value close to $\text{Im}(\xi_k)$, and is defined as

$$\bar{\sigma}_k = \max_{\omega_a \leq \omega \leq \omega_b} \bar{\sigma}(\omega). \quad (5.18)$$

This value is non-differentiable, but can be found numerically using, for instance, a simple bisection algorithm. For efficient numerical evaluation of the singular values of $\mathbf{S}(j\omega)$, a

limited number of eigenmodes is included in the mechanical model, as further explained in Section 5.3. The frequency range used for bisection is defined by

$$\omega_a = \frac{\text{Im}(\xi_{k-1}) + \text{Im}(\xi_k)}{2} \quad \text{and} \quad \omega_b = \frac{\text{Im}(\xi_k) + \text{Im}(\xi_{k+1})}{2}, \quad (5.19)$$

using the sorted closed-loop pole frequencies as

$$\dots \leq \text{Im}(\xi_{k-1}) \leq \text{Im}(\xi_k) \leq \text{Im}(\xi_{k+1}) \leq \dots \quad (5.20)$$

After a numerical search of $\bar{\sigma}_k$, the exact correction factor a_k can be calculated as

$$a_k = \frac{\bar{\sigma}_k}{\gamma_k}. \quad (5.21)$$

As the topology optimization progresses towards a final design, the design changes usually become smaller and smaller. Therefore, it can be assumed that also the correction factor a_k stabilizes during the optimization. During optimization, the correction factor is treated as a constant, which means it does not need differentiation.

By calculating multiple local approximations over the frequency range of interest, the true \mathcal{H}_∞ norm equal to the largest of the locally approximated norms. Multiple constraints can now be formed for each flexible eigenmode k as

$$\alpha_k \gamma_k \leq \frac{1}{\mu}. \quad (5.22)$$

Note that mode switching might occur during optimization, causing constraints to switch order. Depending on the problem and the chosen optimization algorithm, this may lead to convergence issues or oscillations. For cases where it is important to avoid switching, mode tracking can be used to reorder the constraints (Kim and Kim, 2000). In the numerical examples of Section 5.5 no issues regarding mode switching were observed, so no mode tracking is used.

To summarize, the steps of the entire procedure to compute approximations of the \mathcal{H}_∞ norm are as follows

1. Find the relevant closed loop poles ξ_k for each flexible eigenmode k
2. Construct local circle approximations to $\mathbf{S}(j\omega)$ around $\omega \approx \text{Im}(\xi_k)$: Eq. 5.12
3. Calculate the Frobenius norm bound γ_k using the circle approximations: Eq. 5.14
4. Numerically find the true maximum singular values $\bar{\sigma}_k$ around $\omega \approx \text{Im}(\xi_k)$: Eq. 5.18
5. Calculate the (damped) correction factors a_k based on the true values $\bar{\sigma}_k$: Eq. 5.21
6. Use the approximated local \mathcal{L}_∞ norms $\alpha_k \gamma_k$ as constraints: Eq. 5.22

5.3 Modeling

The modeling largely follows the same procedure as in Chapter 4. For the sake of completeness, the modeling steps are also explained here, with focus on the MIMO aspects. As a starting point, the mass and stiffness matrices (\mathbf{M} and \mathbf{K}) dependent on the design variables \mathbf{x} are given, as is described in Chapter 4.

5.3.1 Mechanical model

The mechanical model of the structure is generated using a truncated series of undamped eigenmodes. The N flexible eigenmodes are calculated by solving the eigenvalue problem

$$\begin{aligned} (\mathbf{K} - \Omega_k^2 \mathbf{M}) \boldsymbol{\phi}_k &= \mathbf{0} \quad \forall \quad k = 1, \dots, N, \\ \boldsymbol{\phi}_k^T \mathbf{M} \boldsymbol{\phi}_k &= 1 \\ 0 < \Omega_1 \leq \dots \leq \Omega_N, \end{aligned} \quad (5.23)$$

where the $\boldsymbol{\phi}_k$ and Ω_i denote the eigenmodes and eigenfrequencies, respectively. Besides to the N flexible eigenmodes, there are N_c rigid body modes with a frequency of 0 kHz.

To enable efficient calculation of the eigenmodes for large-scale 3D topology optimization, the problem is parallelized using domain decomposition. This is implemented using the data structures and linear solvers of the PETSc library (Balay *et al.*, 2019), and the eigensolvers of its add-on SLEPc (Hernandez *et al.*, 2005). As in Chapter 2, a Krylov-Schur algorithm with a shift-and-invert strategy is used to obtain the lowest N flexible modes. This algorithm resorts to the repeated solution of linear systems involving the pencil $\mathbf{K} - \zeta_s \mathbf{M}$, with shift frequency ζ_s . The linear systems are solved using the iterative BiCGStab method, preconditioned with an algebraic multigrid preconditioner (Hernandez *et al.*, 2005; Balay *et al.*, 2019; Saad, 2003).

In the current application of a motion stage, the absence of boundary conditions results in multiple rigid body modes Φ_R , up to 6 for systems in 3D. As the rigid body modes can be constructed explicitly and to prevent wasting computational effort by their recalculation, deflation is used to remove them from the search space (Balay *et al.*, 2019; Geradin and Rixen, 2015). This also prevents potential numerical issues due to a singular stiffness matrix \mathbf{K} .

All the N_c rigid body modes in Φ_R and N flexible eigenmodes are placed in the projection matrix Φ as

$$\Phi = [\Phi_R \quad \boldsymbol{\phi}_1 \quad \dots \quad \boldsymbol{\phi}_N]. \quad (5.24)$$

This projection matrix is used to obtain the reduced system of equations describing the structure in the time domain as

$$\begin{aligned} \Omega^2 \mathbf{q}(t) + 2\zeta \Omega \dot{\mathbf{q}}(t) + \ddot{\mathbf{q}}(t) &= \Phi^T \mathbf{F} \mathbf{u}_p(t), \\ \mathbf{y}_p(t) &= \mathbf{G}^T \Phi \mathbf{q}(t). \end{aligned} \quad (5.25)$$

Here, Ω is a diagonal matrix containing all eigenfrequencies, starting with the N_c zeros corresponding to the rigid body modes. The matrices containing all the input and output unit vectors are denoted \mathbf{F} and \mathbf{G} , respectively. The input \mathbf{u}_p represents the amplitude of the force of the actuator and \mathbf{y}_p represents the measurements of the sensors. The state vector \mathbf{q} contains the modal amplitudes corresponding to all the eigenmodes. Transformed into the Laplace domain, the transfer function becomes

$$\mathbf{H}_p(s) = \mathbf{G}^T \Phi (\Omega^2 + 2s\zeta \Omega + s^2 \mathbf{I})^{-1} \Phi^T \mathbf{F}, \quad (5.26)$$

which is dependent on complex frequency s .

5.3.2 Rigid body decoupling

Using rigid body decoupling the transfer function of the plant can be made diagonal for low frequencies. This limits the interaction between the control loops at low frequencies, and aids in the design of a decentralized (diagonal) controller (Van der Veen *et al.*, 2017; Skogestad and Postlethwaite, 2001). Additionally, it allows for transformation of the inputs and outputs of the plant to forces and motions purely based on the rigid body modes, e.g. $\mathbf{u} = [f_x \ f_y \ f_\theta]$ and $\mathbf{y} = [y_x \ y_y \ y_\theta]$ for a 2D system (Fig. 5.1). A constant input to one of these signals results in a constant acceleration for one of the rigid body modes.

By using the pre- and post-compensation matrices \mathbf{W}_a and \mathbf{W}_s , the plant of Eq. 5.26 is statically decoupled. Its inputs and outputs are related as

$$\mathbf{u}_p = \mathbf{W}_a \mathbf{u} \quad \text{and} \quad \mathbf{y} = \mathbf{W}_s \mathbf{y}_p, \quad (5.27)$$

which makes the transfer function of the decoupled plant equal to

$$\mathbf{H}(s) = \mathbf{W}_s \mathbf{H}_p(s) \mathbf{W}_a. \quad (5.28)$$

Omitting the derivation, the decoupling pre-compensation matrix is calculated as (Van der Veen *et al.*, 2017)

$$\mathbf{W}_a = \left(\mathbf{G}^T \Phi_R \Phi_R^T \mathbf{F} \right)^{-1} \mathbf{G}^T \Phi_D, \quad (5.29)$$

where Φ_D contains independent user-defined motions, e.g., containing unit translations and rotations. In the current work, the unit translation and rotation vectors are normalized such that the maximum displacement throughout the domain equals 1 mm. The subsequent post-compensation matrix imposes a mass normalization, such that $\lim_{s \rightarrow 0} s^2 \mathbf{H}(s) = \mathbf{I}$. This matrix is calculated as (Van der Veen *et al.*, 2017)

$$\mathbf{W}_s = \left(\mathbf{G}^T \Phi_D \right)^{-1}. \quad (5.30)$$

Note that the rigid body modes are required to be mass orthonormalized as

$$\Phi_R^T \mathbf{M} \Phi_R = \mathbf{I}. \quad (5.31)$$

Further details and derivation of the design sensitivities can be found in the work of Van der Veen *et al.* (2017).

5.3.3 Controller

The decoupled plant of Eq. 5.28 can effectively be controlled using a decentralized diagonal controller structure. Again, the same controller structure (PID with additional low pass filter) as in Chapter 4 is used (Munnig Schmidt *et al.*, 2011; Van der Veen *et al.*, 2017), which is defined as

$$C_{ii}(s) = k_i \frac{s + \frac{1}{5} \omega_{b,i}}{s} \frac{3s + \omega_{b,i}}{s + 3\omega_{b,i}} \frac{5\omega_{b,i}}{s + 5\omega_{b,i}}. \quad (5.32)$$

The controllers are tuned with the parameters k_i denoting gain and $\omega_{b,i}$ denoting the bandwidth. Because the mass is normalized with the post-compensation matrix \mathbf{W}_s in Eq. 5.30, the loop gain at the bandwidth $\left| L_{ii}(j\omega_{b,i}) \right| = k_i \omega_{b,i}^2$ is independent of the system mass. To

ensure correct interaction between the controller and the rigid body modes, the gain at the bandwidth is chosen as $|L_{ii}(j\omega_{b,i})| = k_0$. This results in a controller gain of

$$k_i = \frac{k_0}{\omega_{b,i}^2}. \quad (5.33)$$

In current work, a value of $k_0 = 1.1$ is used. The method is not limited to this decentralized MIMO control law can potentially be extended to other controller variations.

The control law, relating the measured error \mathbf{e} to the correction signal \mathbf{u} (Fig. 5.1), can be rewritten into state-space form

$$\begin{aligned} \dot{\mathbf{c}}(t) &= \mathbf{A}_c \mathbf{c}(t) + \mathbf{B}_c \mathbf{e}(t) \\ \mathbf{u}(t) &= \mathbf{C}_c \mathbf{c}(t) \end{aligned} \quad (5.34)$$

where \mathbf{A}_c , \mathbf{B}_c , \mathbf{C}_c represent the controller structure in canonical form (Skogestad and Postlethwaite, 2001). The vector \mathbf{c} contains the internal state of the PID controller and is of length $3N_c$, where N_c is the number of controllers used. As each rigid body mode is separately controlled using a controller, N_c is equal to the number of rigid body modes.

5.3.4 Closed loop system

The final step in the modeling is to obtain the transfer function of the closed-loop sensitivity function $\mathbf{S}(s)$, which can be represented in state-space form as

$$\begin{aligned} \dot{\mathbf{z}}(t) &= \mathbf{A}_s \mathbf{z}(t) + \mathbf{B}_s \mathbf{d}(t) \\ \mathbf{y}(t) &= \mathbf{C}_s \mathbf{z}(t) + \mathbf{D}_s \mathbf{d}(t) \end{aligned} \quad (5.35)$$

with system matrices and state vector

$$\begin{aligned} \mathbf{A}_s &= \begin{bmatrix} \mathbf{A}_c & -\mathbf{B}_c \mathbf{W}_s \mathbf{G}^T \Phi & \mathbf{0} \\ \mathbf{0} & \mathbf{0} & \mathbf{I} \\ \Phi^T \mathbf{F} \mathbf{W}_a \mathbf{C}_c & -\Omega^2 & -2\zeta \Omega \end{bmatrix}, \\ \mathbf{B}_s &= [-\mathbf{B}_c \quad \mathbf{0} \quad \mathbf{0}]^T, \\ \mathbf{C}_s &= [\mathbf{0} \quad \mathbf{W}_s \mathbf{G}^T \Phi \quad \mathbf{0}], \\ \mathbf{D}_s &= \mathbf{I}, \\ \mathbf{z} &= [\mathbf{c} \quad \mathbf{q} \quad \dot{\mathbf{q}}]^T. \end{aligned} \quad (5.36)$$

The transfer function of the sensitivity function then becomes

$$\mathbf{S}(s) = (\mathbf{I} + \mathbf{L}(s))^{-1} = \mathbf{C}_s (s\mathbf{I} - \mathbf{A}_s)^{-1} \mathbf{B}_s + \mathbf{D}_s, \quad (5.37)$$

which is used to fit local circle approximations. The closed-loop poles ξ_k are found as the eigenvalues of the closed-loop matrix \mathbf{A}_s . In total there are $5N_c + 2N$ closed-loop poles: 3 for each controller, 2 for each rigid body mode, and also 2 for each flexible mode. The participation factors \mathbf{P}_k can be found using a modal decomposition as described in Chapter 4.

Circles and \mathcal{H}_∞ norm approximations only have to be constructed for the N poles with largest imaginary values, which correspond to the flexible eigenmodes. To use the approximated \mathcal{H}_∞ norm in an optimization setting in order to control disturbance rejection properties, closed-loop stability is necessary and must be enforced by, e.g., constraining the real part of the closed-loop poles below zero.

5.4 Approximation of eigenmode design sensitivities

In this section, first will be explained how consistent eigenmode design sensitivities can be calculated for large-scale systems. Based on this, a strategy is proposed to approximate the eigenmode sensitivities and reduce computation time.

5.4.1 Consistent eigenmode sensitivities

Given the generalized eigenvalue problem as defined in Eq. 5.23, the eigenmode design sensitivities capture how the eigenmode changes as the design is changed. To calculate the eigenmode sensitivities efficiently for problems with many design variables and relatively few constraints, the adjoint method is used. In the work of Lee (1999), it can be found that the adjoint sensitivities for an arbitrary response function $f(\Omega_k, \phi_k)$ with respect to the stiffness matrix \mathbf{K} and mass matrix \mathbf{M} can be calculated, respectively, using

$$\frac{\partial f}{\partial \mathbf{K}} = -\mathbf{v}_k \otimes \phi_k \quad \text{and} \quad \frac{\partial f}{\partial \mathbf{M}} = \left(\Omega_k^2 \mathbf{v}_k + \frac{\alpha_k}{2} \phi_k \right) \otimes \phi_k. \quad (5.38)$$

Here, the adjoint variables \mathbf{v}_k and α_k are found by solving the saddlepoint problem given as

$$\begin{bmatrix} \mathbf{K} - \Omega_k^2 \mathbf{M} & -\mathbf{M} \phi_k \\ -\phi_k \cdot \mathbf{M} & 0 \end{bmatrix} \begin{bmatrix} \mathbf{v}_k \\ \alpha_k \end{bmatrix} = \begin{bmatrix} \frac{\partial f}{\partial \phi_k} \\ \frac{1}{2\Omega_k} \frac{\partial f}{\partial \Omega_k} \end{bmatrix}, \quad (5.39)$$

which is a non-singular system of equations.

For a small problems, the solution to this expression can simply be found using a factorization of Eq. 5.39. Factorizations need to be created for the matrices corresponding to each of the eigenvalues Ω_k , which can be reused for the eigenmode design sensitivities from different constraints. However, it is usually not feasible to factorize the matrices for large-scale problems, due to limitations in time and/or memory. Instead, the systems of equations are usually solved by Krylov methods (e.g., GMRES, BiCGStab, MINRES (Paige and Saunders, 1975; Saad, 2003)), which iteratively find the solution. For an efficient operation of these iterative methods, preconditioners (such as multigrid) are used (Saad, 2003). However, because of changed structure, it is not directly possible to use the same solvers and preconditioners that were used in solving the eigenvalue problem of Eq. 5.23 (Benzi et al., 2005). Therefore, an alternative approach is proposed in which the same solvers and preconditioners can be used as in the solution of the eigenvalue problem.

From here on the subscript k is omitted for clarity. The first equation in Eq. 5.39 reads

$$(\mathbf{K} - \Omega^2 \mathbf{M})\mathbf{v} = \mathbf{r}, \quad \text{with} \quad \mathbf{r} = \frac{\partial f}{\partial \phi} + \alpha \mathbf{M} \phi. \quad (5.40)$$

This system of equations is singular, due to the original eigenvalue problem defined in Eq. 5.23. However, it can be solved by combining a homogeneous solution $c\phi$ and a particular solution \mathbf{v}_p as

$$\mathbf{v} = \mathbf{v}_p + c\phi. \quad (5.41)$$

Now, substituting this into Eq. 5.40 and rewriting yields

$$(\mathbf{K} - \Omega^2\mathbf{M})\mathbf{v}_p = \mathbf{r}. \quad (5.42)$$

This system of equations is still singular, but a particular solution \mathbf{v}_p can be found, e.g., by constraining one of its entries or to find the minimum norm solution with $\phi^T\mathbf{v}_p = 0$. To make the system consistent, the right-hand-side must be orthogonal to the eigenmode. This is done by choosing the unknown α_k as

$$\alpha = -\phi^T \frac{\partial f}{\partial \phi}, \quad (5.43)$$

which ensures the condition $\phi^T\mathbf{r} = 0$.

After a particular solution \mathbf{v}_p is found, the homogeneous solution can be obtained using the second equation in Eq. 5.39 as

$$c = -\phi^T\mathbf{M}\mathbf{v}_p - \frac{1}{2\Omega} \frac{\partial f}{\partial \Omega}. \quad (5.44)$$

The procedure explained here needs to be executed a total of $N \cdot N_{\text{constr}}$ times: N times for every constraint that depends on the eigenmodes. This makes it very suitable when few responses (*i.e.* constraints) are dependent on only few eigenmodes. However, for the current application many constraints and eigenmodes are required, which would result in a colossal computational load.

5.4.2 Approximate eigenmode sensitivities

The computationally expensive step is in the computation of the particular solution \mathbf{v}_p given in Eq. 5.42. By approximating the particular solution \mathbf{v}_p , solving this system of equations may be prevented. The approximation of eigenmode sensitivities has extensively been researched for direct sensitivities (see, e.g. Wang, 1990; Lin *et al.*, 2020), but to the best of our knowledge not yet in an adjoint setting.

The particular solution may be approximated using a linear combination of basis vectors \mathbf{W} as

$$\mathbf{v}_p \approx \mathbf{W}\tilde{\mathbf{v}}_p, \quad (5.45)$$

preventing the computationally costly solution of Eq. 5.42. By Galerkin projection, the reduced system of equations becomes

$$(\tilde{\mathbf{K}} - \Omega^2\tilde{\mathbf{M}})\tilde{\mathbf{v}}_p = \mathbf{W}^T\mathbf{r}, \quad (5.46)$$

with the reduced-order system matrices

$$\tilde{\mathbf{K}} = \mathbf{W}^T\mathbf{K}\mathbf{W} \quad \text{and} \quad \tilde{\mathbf{M}} = \mathbf{W}^T\mathbf{M}\mathbf{W}. \quad (5.47)$$

Instead of having to solve a large system of equations, it is approximated using a small one. After approximation, the remaining steps in the eigenmode sensitivity calculation are identical as presented in Section 5.4.1.

The main difficulty is to determine which vectors to incorporate in the basis \mathbf{W} , as it affects the final accuracy of the approximate solution. A straightforward choice is to use the eigenmodes Φ , which are already known and required for the analysis. However, this might yield inaccurate results, in particular with respect to the input and output locations, as was shown in Chapter 3. In order to improve accuracy, the eigenmodes are augmented with a moment matching basis. Moment matching is a method to obtain reduced-order models with accurate input-output relations (Grimme, 1997; Antoulas, 2004).

To augment the basis with moment matching vectors, Krylov subspaces are used. A general Krylov subspace with N_r vectors is defined as

$$\mathcal{K}_r(\mathbf{A}, \mathbf{b}) := \text{span}\{\mathbf{b}, \mathbf{A}\mathbf{b}, \mathbf{A}^2\mathbf{b}, \dots, \mathbf{A}^{N_r-1}\mathbf{b}\}. \quad (5.48)$$

For a collocated SISO system, the moment matching basis is calculated as

$$\mathbf{V} = \mathcal{K}_r(\mathbf{K}_\zeta^{-1}\mathbf{M}, \mathbf{K}_\zeta^{-1}\mathbf{f}), \quad (5.49)$$

where \mathbf{f} is the input/output vector and \mathbf{K}_ζ is defined as the shifted pencil

$$\mathbf{K}_\zeta := \mathbf{K} - \zeta^2\mathbf{M}, \quad (5.50)$$

with the shift frequency ζ corresponding to the interpolation frequency for moment matching, chosen such that \mathbf{K}_ζ is non-singular. In a general MIMO problem there are multiple inputs and outputs, for which the moment matching basis can be calculated as the union of multiple Krylov subspaces (Grimme, 1997)

$$\mathbf{V} = \bigcup_{i=1}^{N_{i_0}} \mathcal{K}_r(\mathbf{K}_\zeta^{-1}\mathbf{M}, \mathbf{K}_\zeta^{-1}\mathbf{f}_i), \quad (5.51)$$

where the different \mathbf{f}_i represent all N_{i_0} unique input and output vectors, $\mathbf{f}_i \in \text{span}\{\mathbf{F}, \mathbf{G}\}$. In total the moment matching basis then contains $N_r \cdot N_{i_0}$ columns. This moment matching basis is combined with the existing eigenmodes to obtain the basis used to approximate the eigenmode sensitivities. The resulting basis is made orthonormal with respect to the mass matrix \mathbf{M}

$$\mathbf{W} = [\Phi \quad \mathbf{V}] \quad \text{s.t.} \quad \mathbf{W}^T\mathbf{M}\mathbf{W} = \mathbf{I}. \quad (5.52)$$

In order to calculate the MIMO moment matching basis of Eq. 5.51, Algorithm 1 presents an adapted block Arnoldi algorithm (Saad, 2003). This algorithm ensures orthogonality of the basis and is numerically stable for higher order Krylov vectors, by using the modified Gram-Schmidt process on each newly calculated basis vector.

Algorithm 1 Block Arnoldi augmentation

Require: $\mathbf{W} \leftarrow \Phi$
Ensure: $\mathbf{W}^T \mathbf{M} \mathbf{W} = \mathbf{I}$

$\mathbf{K}_\zeta \leftarrow \mathbf{K} - \zeta^2 \mathbf{M}$ \triangleright Apply matrix shift
for $j = 1, \dots, N_r$ **do** \triangleright Loop over Krylov size
 for $i = 1, \dots, N_{io}$ **do** \triangleright Loop over in/outputs
 if $j = 1$ **then** \triangleright Initial Krylov vector
 $\mathbf{f} \leftarrow \text{M-Orthonormalize}(\mathbf{f}_i, \mathbf{W})$
 else
 $\mathbf{f} \leftarrow \mathbf{v}_i$ \triangleright Higher powers
 end if
 $\mathbf{p} \leftarrow \mathbf{K}_\zeta^{-1} \mathbf{M} \mathbf{f}$
 $\mathbf{v}_i \leftarrow \text{M-Orthonormalize}(\mathbf{p}, \mathbf{W})$
 $\mathbf{W} \leftarrow [\mathbf{W} \ \mathbf{v}_i]$ \triangleright Store vector
 end for
end for

A known issue for the block Arnoldi algorithm is the chance of linearly dependent vectors appearing (Ruhe, 1979). Whenever the candidate vector \mathbf{p} in the algorithm is linear dependent on the basis \mathbf{W} , the vector will have a length close to zero after the modified Gram-Schmidt process. Subsequent normalization then results in a vector with random numerical noise. Monitoring for the situation is recommended, however, in the numerical examples of Section 5.5 no issues with linear dependency were encountered.

The augmented reduction basis \mathbf{W} is not used for the analysis of the controlled system, since the moment matching adds new eigenvalues to the reduced-order model (Ritz values of the original system) that might destabilize the closed loop system. Therefore, the analysis proceeds with the eigenmodes Φ , and the augmented basis \mathbf{W} is only used for the approximation of eigenmode sensitivities.

The computationally costly steps in this algorithm is the multiplication with the shifted and inverted matrix to expand the Krylov subspace. The type of linear system of equations

Table 5.1: Comparison in computational effort for eigenmode sensitivities in one design iteration. (*) No factorization is required in case it is reused from the eigenvalue solver. In the application presented N and N_{constr} are both large, while N_r and N_{io} are relatively small.

	Consistent	Approximate
Factorizations / Preconditioner setup	N	1 (0*)
Backsubstitutions / Iterative solutions	$N \cdot N_{\text{constr}}$	$N_r \cdot N_{io}$
ROM solutions	-	$N \cdot N_{\text{constr}}$

is similar, as the system matrix in Eq. 5.42 and \mathbf{K}_ζ in Eq. 5.50 are both shifted matrices. However, there are significant benefits in the moment matching approach as opposed to calculating consistent eigenmode design sensitivities:

- Shift frequency ζ can be chosen such that the matrix \mathbf{K}_ζ is non-singular
- The same preconditioner and solvers can be reused for computing all Krylov vectors
- The same solver and preconditioner used to solve the eigenvalue problem (Eq. 5.23) can be reused
- In case of a direct solver, only one matrix factorization is required
- The computational cost for additional constraints is negligible

A complete breakdown of the computational cost of the approximate versus the consistent method of calculating eigenmode sensitivities in one design iteration is presented in Table 5.1.

5

5.5 Numerical examples

5.5.1 Optimization formulation

The formulation used for integrated controller-structure optimization throughout the numerical examples is given as

$$\begin{aligned}
 \min_{\mathbf{x}, \mathbf{x}_\omega} \quad & 100 \left(c_1 \frac{f_\omega^{(0)}}{f_\omega(\mathbf{x}_\omega)} + (1 - c_1) \frac{f_\Omega^{(0)}}{f_\Omega(\mathbf{x})} \right) + c_2 f_V(\mathbf{x}), \\
 \text{s.t.} \quad & 10 \left(\frac{V(\mathbf{x})}{v_f V_{\max}} - 1 \right) \leq 0, \\
 & g_{\text{rob},kp}(\mathbf{x}, \mathbf{x}_\omega) \leq 0 \quad \forall \begin{cases} k = 1, \dots, N \\ p = 1, \dots, N_{\text{pos}} \end{cases}, \\
 & g_{\text{stab},p}(\mathbf{x}, \mathbf{x}_\omega) \leq 0 \quad \forall p = 1, \dots, N_{\text{pos}}, \\
 & 0 \leq \mathbf{x} \leq 1, \\
 & 0 \leq \mathbf{x}_\omega \leq 1.
 \end{aligned} \tag{5.53}$$

Here, a number of different relative sensor positions (N_{pos}) may be used to incorporate position-dependent dynamics into the optimization. The superscript (0) indicates the function value in the initial iteration, which is used for normalization. The bandwidths ω_b are exponentially scaled within their bounds (ω_{\min} and ω_{\max}) as

$$\omega_{b,i}(x_{\omega,i}) = \omega_{\min} \left(\frac{\omega_{\max}}{\omega_{\min}} \right)^{x_{\omega,i}}. \tag{5.54}$$

The volume $V(\mathbf{x})$ is constrained by an upper limit, which is composed of a fraction v_f of the maximum available volume V_{\max} . For the numerical examples presented, this volume constraint is active.

The objective function in the problem formulation (Eq. 5.53) is composed of multiple sub-objectives concerning the maximization of bandwidths f_ω , maximization of eigenfrequencies f_Ω , and penalization of low-density areas f_v . The eigenfrequency objective f_Ω is added to prevent eigenfrequencies from becoming excessively low. To control the weights between the different objectives parameters c_1 and c_2 can be chosen by the user. The objective with respect to bandwidths ω_b is defined as

$$f_\omega(\mathbf{x}_\omega) = \sum_{i=0}^{N_c} \frac{1}{\omega_{b,i}(x_{\omega,i})^2} \quad (5.55)$$

and the objective responsible for maximization the eigenfrequencies Ω_i as

$$f_\Omega(\mathbf{x}) = \sum_{i=0}^3 \frac{1}{\Omega_i(\mathbf{x})^2}. \quad (5.56)$$

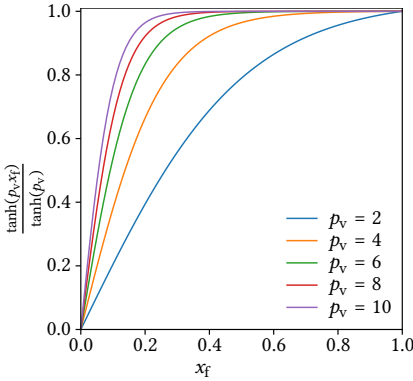


Figure 5.4: The function used in low density penalization (Eq. 5.57). Increasing p_v results in a steeper slope at 0.

The penalty f_v is to aid in removing low densities that otherwise might cause localized eigenmodes in low density areas and is defined as

$$f_v = \sum_{i \in \mathcal{E}} \frac{\tanh(p_v x_{f,i})}{\tanh(p_v) V_{\max}}. \quad (5.57)$$

Here, \mathcal{E} denotes the entire design domain (e.g. Fig. 5.5) and \mathbf{x}_f represents the filtered density field. The behavior of this function is illustrated in Fig. 5.4. It ensures a steep gradient towards zero, which effectively attracts elements with low densities towards zero. At higher density values, the function flattens and the effect is decreased. This ensures the removal of remaining low-density areas when they are not effective for performance, and thus aids in preventing the appearance of localized eigenmodes. Additionally, any disconnected or loosely connected parts are removed through a flood fill algorithm (e.g., Bruns and Tortorelli, 2003). Elements that are connected to the non-design domains through densities lower than 0.2 are recursively clipped to the maximum of their neighbors. This measure also helps to prevent localized modes and additional rigid body modes that hamper convergence. The flood fill process introduces a non-differentiable step, however the

effect of this was found to be far less detrimental to the convergence than the disruptions caused by localized modes.

For robustness against disturbances, the constraints $g_{\text{rob},kp}$ provide limitation of the local approximated \mathcal{L}_∞ norms (Eq. 5.22) for mode k and relative stage position p as

$$g_{\text{rob},kp}(\mathbf{x}, \mathbf{x}_\omega) = 10 \left(\mu \alpha_{kp} \gamma_{kp}(\mathbf{x}, \mathbf{x}_\omega) - 1 \right). \quad (5.58)$$

Additional constraints are required to ensure closed-loop stability (Van der Veen *et al.*, 2017), and are defined as

$$g_{\text{stab},p}(\mathbf{x}, \mathbf{x}_\omega) = \frac{1}{p_{\text{KS}}} \log \left(\sum_i \exp \left(p_{\text{KS}} \frac{\text{Re}(\xi_{ip})}{2\zeta} \right) \right). \quad (5.59)$$

This is the KS function (Kreisselmeier and Steinhauser, 1980), approximating the maximum of the real parts of *all* closed-loop poles ξ_{ip} at position p . The maximum must remain below zero to ensure closed-loop stability. Furthermore, the poles are normalized with the modal damping ratio ζ . Note that this constraint is generally not active, as the \mathcal{L}_∞ norm constraints ensure a margin for stability.

Prior to the integrated optimization, the controller is first tuned to meet the closed-loop requirements for the initial design. This is done using the optimization formulation given as

$$\begin{aligned} \min_{\mathbf{x}_\omega} \quad & 100 \frac{f_\omega^{(0)}}{f_\omega(\mathbf{x}_\omega)}, \\ \text{s.t.} \quad & g_{\text{rob},kp}(\mathbf{x}_\omega) \leq 0 \quad \forall \begin{cases} k = 1, \dots, N \\ p = 1, \dots, N_{\text{pos}} \end{cases}, \\ & g_{\text{stab},p}(\mathbf{x}_\omega) \leq 0 \quad \forall p = 1, \dots, N_{\text{pos}}, \\ & 0 \leq \mathbf{x}_\omega \leq 1. \end{aligned} \quad (5.60)$$

After optimization of this problem, the controller is tuned to the initial structure. The resulting bandwidths are used as initial values for the integrated controller-structure optimization.

For all the numerical examples, the optimization algorithm MMA is used (Svanberg, 1987). The maximum number of iterations is limited to 100, and a maximum step-size for the design variables of 0.05 is used. Further default settings as used in the examples are presented in Table 5.2. The design is forced to be symmetric and a uniform initial design is used with densities v_f . This is not to violate the volume constraint in the initial iterations. Additionally, the design is filtered as is standard topology optimization procedure (Bruns and Tortorelli, 2001; Bendsoe and Sigmund, 2003).

5.5.2 Design case in 2D

First, a 2D design case is presented that will be used to provide insight into the different aspects of the presented methods. The example contains only one relative sensor position ($N_{\text{pos}} = 1$) and is shown in Fig. 5.5. It has one sensor measuring the x-direction (c_x) and two in y-direction ($c_{y,1}$ and $c_{y,2}$). The measurement of the rigid body motion in y-direction is done by combining the two sensors as $c_{y,1}/2 + c_{y,2}/2$, and of the rotation degree of freedom

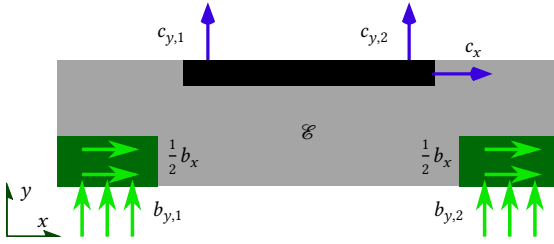


Figure 5.5: The domain used for the 2D optimizations, with one relative sensor position ($N_{\text{pos}} = 1$). The domain has dimensions 400×100 mm, with an in-plane thickness of 400 mm. It is discretized in 192×48 square elements.

as $-c_{y,1}/2 + c_{y,2}/2$. Similarly, this is done for the inputs by combining the actuators b_x , $b_{y,1}$ and $b_{y,2}$. The non-design domains are shown in black and green, for which the green represents magnetic actuators made out of neodymium. The rest of the part is made out of aluminium. The material properties for both of these materials are given in Table 5.2.

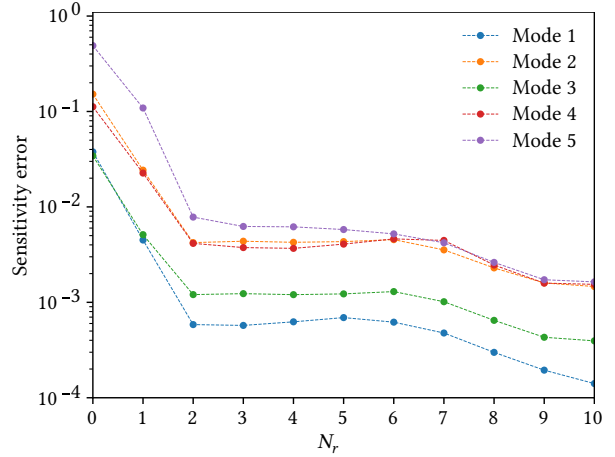
Table 5.2: Default settings as used for the numerical examples.

Symbol	Value	Description
ω_{\min}	0.2 rad/ms	Minimum bandwidth
ω_{\max}	20.0 rad/ms	Maximum bandwidth
μ	0.5	MIMO margin
E_0	65 GPa	Young's modulus (Aluminium)
ρ_0	2.6×10^{-6} kg/mm ³	Material density (Aluminium)
E_{neo}	160 GPa	Young's modulus (Neodymium)
ρ_{neo}	7.5×10^{-6} kg/mm ³	Material density (Neodymium)
x_{\min}	10^{-7}	Minimum design density
ζ	0.01	Damping factor
N	2D: 10, 3D: 20	Number of eigenmodes
v_f	0.3	Volume fraction
	2 elements	Density filter radius
c_1	0.8	Objective weight
c_2	10	Low-density penalty weight
p_v	6.0	Low-density penalty factor
p_{KS}	2.0	Stability aggregation factor
N_r	2	Size of Krylov subspace
ς	2.0 rad/ms	Moment matching shift

5.5.3 Effect of approximate design sensitivities

By adding more Krylov vectors into the reduced-order basis of Eq. 5.52, the accuracy of the design sensitivities is expected to improve. This is studied using the 2D example given in Fig. 5.5. The design sensitivities with respect to the disturbance rejection constraints (Eq. 5.58) are calculated with different sizes of the Krylov subspace N_r , and compared to the consistently calculated eigenmode design vectors as described in Section 5.4.1. For

Figure 5.6: The error in sensitivity (Eq. 5.61) as function of number of Krylov vectors N_r . The errors refers to the first five constraints on the local \mathcal{L}_∞ norm, for the initial design in Fig. 5.5 with tuned controller and uniform design densities at v_f .



5

comparison, a relative error norm is defined as

$$\epsilon_{\text{rob},k} = \frac{\left\| \left(\frac{\partial g_{\text{rob},k}}{\partial \mathbf{x}} \right)_{\text{cons}} - \left(\frac{\partial g_{\text{rob},k}}{\partial \mathbf{x}} \right)_{N_r} \right\|_2}{\left\| \left(\frac{\partial g_{\text{rob},k}}{\partial \mathbf{x}} \right)_{\text{cons}} \right\|_2}. \quad (5.61)$$

Here, the subscript ‘cons’ indicates consistent sensitivities and the sensitivities subscripted with N_r are approximated. Note that the total size of the augmented reduction basis is $N_r \cdot N_{i_0}$. For the current example, the number of unique input and output vectors is $N_{i_0} = 6$ (three inputs and three outputs). In Fig. 5.6, the order of the Krylov subspace is increased from 0 (no augmentation) to 10. It can clearly be seen that adding a few vectors significantly reduces the error, although it reaches a plateau for $N_r = 2, \dots, 7$. Adding further vectors reduces the error, although less significantly than for the initial few vectors. From this data, the ‘optimal’ order of the Krylov subspace for the current application is heuristically chosen as $N_r = 2$, balancing accuracy with computational effort.

For the 2D example with one relative sensor position, the choice of $N_r = 2$ means reduction of computational cost by almost a factor 10 (Table 5.1). Since the 2D case is relatively small, Cholesky factorizations can be used for the solution of the eigenmode sensitivities (Eq. 5.39). In case of consistent sensitivities, 10 factorizations are required (one for each eigenmode, $N = 10$), while for the approximations only one single factorization is required of \mathbf{K}_c (Eq. 5.50).

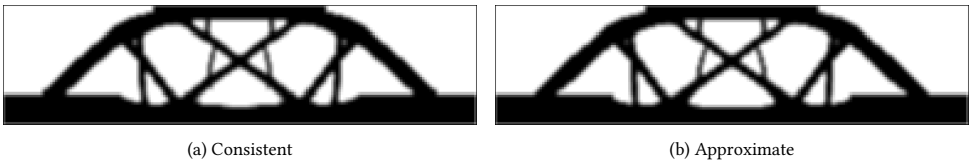


Figure 5.7: Comparison of optimized designs using consistent and approximate eigenmode design sensitivities.

Next, optimizations are performed with both consistent eigenmode design sensitivities and approximated with $N_r = 2$. The resulting designs (Fig. 5.7) are visually very similar. Also their performance is almost identical, with $\omega_b = [0.93 \ 0.49 \ 1.11]$ kHz for the consistently optimized design and $\omega_b = [0.95 \ 0.50 \ 1.13]$ kHz for the design optimized with approximate design sensitivities.

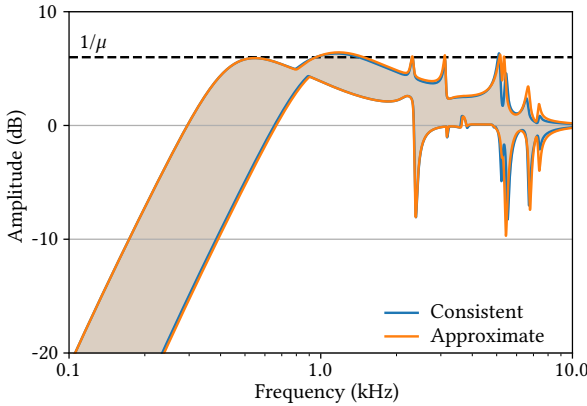


Figure 5.8: Extreme singular value plot for the sensitivity function, showing $\underline{\sigma}(\omega)$ and $\bar{\sigma}(\omega)$ for the designs optimized with consistent and approximated design sensitivities.

The singular value plot of both designs can be seen in Fig. 5.8. It can be seen that the second ‘bump’ violates the $1/\mu$ limit around 1 kHz. These first bumps are caused by the interaction of the rigid body mode and the controller, and could unfortunately not be limited with the proposed method. However, by the choice of control gain (Eq. 5.33), the diagonal entries of the sensitivity function $|S_{ii}|$ satisfy the limit on disturbance rejection. Furthermore, not all constraints are satisfied in a mathematical sense, although they are very close to being feasible. For engineering purposes this is assumed not to be an issue.

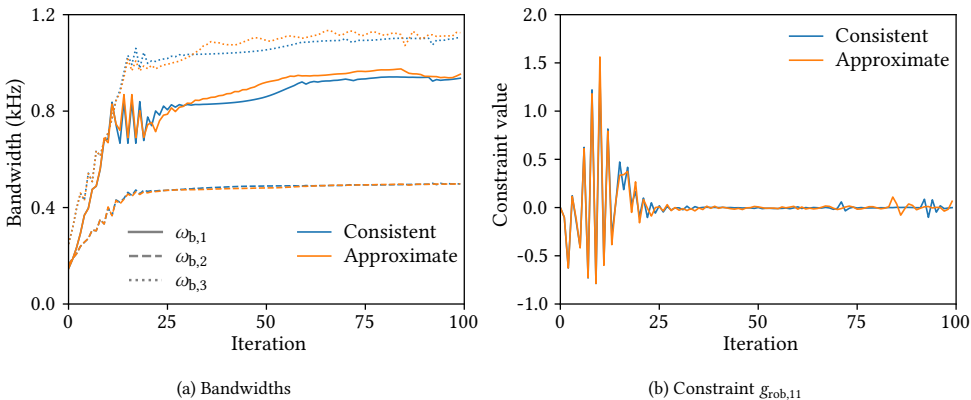


Figure 5.9: Comparisons in convergence behavior for consistent and approximated design sensitivities. a) Convergence history of the three bandwidths ω_b . b) Convergence history of the first robustness constraint $g_{rob,11}$.

The convergence of the bandwidths throughout the iteration history is depicted in Fig. 5.9a, which shows their trajectories are very alike. The convergence behavior is not

very smooth, with quite some oscillations present in the bandwidths. Oscillations are also observed in the convergence of the constraints, as seen in Fig. 5.9b for the first robustness constraint $g_{\text{rob},11}$. As the oscillations are present in both the consistent and approximated design sensitivities, it seems reasonable that they are not caused by incorrect design sensitivities, but rather by the nature of the problem. Despite the oscillations, the optimization converges to a solution that is interpretable and useable.

These results provide confidence that the approximation of eigenmode design sensitivities is suitable for optimization. Additionally, with a limited number of Krylov vectors (12 in the example) the resulting sensitivities are sufficiently accurate to use in optimization. This leads to a significant computational gain for the design sensitivities of almost an order of magnitude in 2D.

5.5.4 Effect of diagonal sensitivity function limitation

The local circular approximations of the sensitivity function (Eq. 5.13) can also be used to constrain individual amplitudes. This approach was employed by Van der Veen *et al.* (2017), who imposed limitations on the diagonal entries of $|S_{ii}(j\omega)|$, although they did not use local circle approximations and design sensitivity approximation. The effect of only constraining diagonal entries is demonstrated by an optimization. The constraints on the approximated \mathcal{L}_∞ norms (g_{rob} in Eq. 5.53) are replaced with new constraints on the diagonals

$$g_{\text{diag},kpi} = 10 \left(\mu(|X_{iik}| + R_{iik})_p - 1 \right) \forall \begin{cases} k = 1, \dots, N \\ p = 1, \dots, N_{\text{pos}} \\ i = 1, \dots, N_c \end{cases} . \quad (5.62)$$

From the subscripts, it can directly be seen that a large number of constraints is required, resulting in additional computation time. For the current example with three controllers, the number of constraints is increased threefold.



Figure 5.10: Design as optimized with only diagonal sensitivity entries.

The resulting design after optimization is shown in Fig. 5.10, which looks significantly different from the design optimized for the \mathcal{H}_∞ norm in Fig. 5.7b. The bandwidths of the diagonally optimized design are also significantly higher, with $\omega_b = [1.15 \ 1.49 \ 2.78]$ kHz. In vertical direction and rotation (second and third control loop), the bandwidth has almost increased threefold. However, this apparent improvement has a clear downside.

In Fig. 5.11a, the diagonal entries of the sensitivity function are presented and compared with the \mathcal{H}_∞ optimized design of Fig. 5.7b. Clearly, the constraints were effective in limiting the maximum value, as many peak values are touching the limit $1/\mu$ for the diagonally optimized design, but none are exceeding the limit. However, when inspecting the extreme singular values shown in Fig. 5.11b, the diagonally optimized design reaches

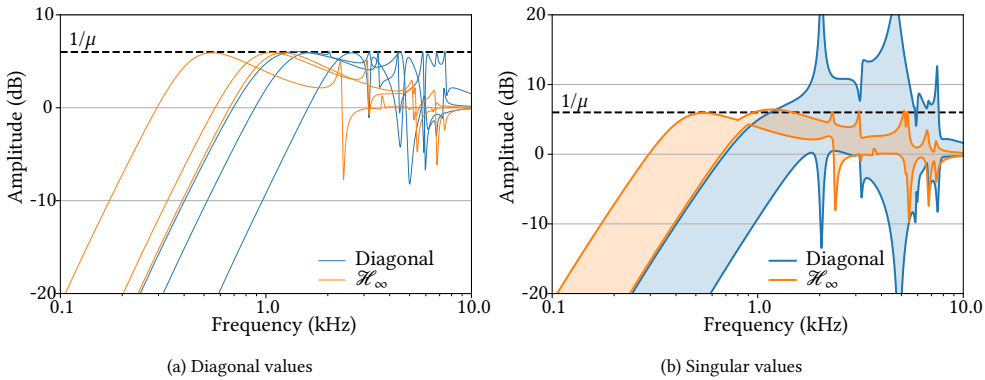


Figure 5.11: Comparing behavior of the sensitivity function between the optimized design considering the diagonal entries to the design optimized for the \mathcal{H}_∞ norm. a) Sensitivity functions corresponding to the diagonal entries. b) Extreme singular value plot for the sensitivity function.

values up to 27 dB, which is well above the allowed limit. This leads to sensitive MIMO behavior when disturbances of one control loop enter the other loops, and illustrates the importance of constraining all entries of the sensitivity function in an integrated optimization.

5

5.5.5 Comparison of performance in 2D

Several variations on the optimization problem are explored to compare performance. Following is a short description on each case variation:

- A. A sequential approach, with separate design of structure and controller. First, the structure is optimized for maximum eigenfrequencies using f_Ω (Eq. 5.56) as an objective, subject to a volume constraint (as is also done in Chapter 4). Second, the controller is tuned using the proposed formulation in Eq. 5.60.
- B. The integrated 2D optimization case, as already presented in Fig. 5.7b.
- C. An integrated optimization, with the bandwidth in all control loops equal to each other.
- D. The integrated optimization as in (B), but with application of the robust method presented in Chapter 4. A larger filter radius of 5 elements is used, the robust offsets (η) are chosen as 0.45, 0.5, 0.55, and the edge contrast parameter (β) is linearly increased from 0.1, ..., 20 throughout iterations 15, ..., 85 (Wang *et al.*, 2011).

All resulting designs are shown in Fig. 5.12 and their corresponding performance values are listed in Table 5.3. All designs converged to a feasible solution, although variation C required more iterations to become feasible (200 instead of 100).

Compared to the sequentially optimized design (A), the integrated optimization (B) results in significantly higher bandwidths in x -direction (+116%) and in rotation (+45%). For the design optimized for maximum eigenfrequencies (A), all eigenfrequencies are higher

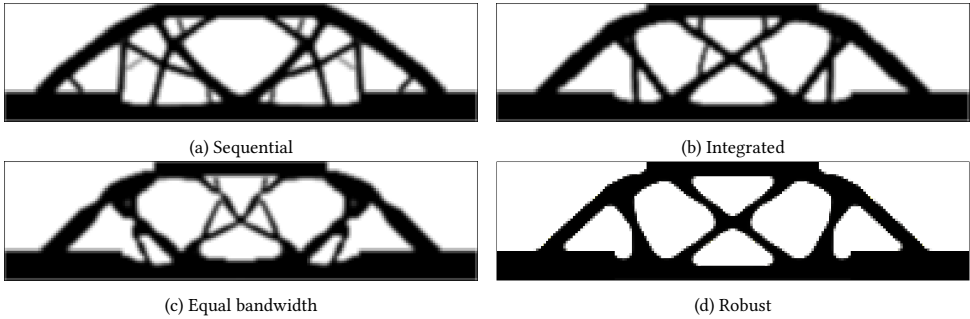


Figure 5.12: Comparison of the designs from different optimization variations.

Table 5.3: Performance overview of the sequential and multiple integrated optimizations.

Units: kHz	Bandwidth			Eigenfrequency		
	$\omega_{b,x}$	$\omega_{b,y}$	$\omega_{b,\theta}$	Ω_1	Ω_2	Ω_3
A. Sequential (max. eigenfrequencies)	0.44	0.50	0.78	2.38	3.49	3.81
B. Integrated	0.95	0.50	1.13	2.38	3.15	3.66
C. Equal bandwidth	0.58	0.58	0.58	2.18	2.73	3.11
D. Robust integrated	0.96	0.51	1.14	2.46	3.30	3.52

than those of the other designs, although the first eigenfrequency is very close to that of design B.

From all bandwidths, the bandwidth in y-direction is lowest. Even when comparing the designs from the integrated optimizations (B and D) to the sequentially optimized design (A), there is little to no increase of bandwidth in y-direction. Only when choosing the bandwidth equal for all control loops (C), the bandwidth in y-direction increases by +16%. This may be explained by the aspect ratio of the design domain and the relatively heavy actuator masses in the corners, which cause the lowest eigenmodes to have relatively large amplitudes in y-direction as compared to the x-direction.

The design optimized with the robust formulation (D) has a more crisp boundary between solid and void than the other designs, as is expected (Wang *et al.*, 2011). It also contains less thin members compared to the other designs, due to the minimum length-scale introduced by the robust formulation (Trillet *et al.*, 2021), while the overall topology is still similar to design B. Surprisingly, the bandwidths of design D surpass those of the integrated design without robust formulation (B) by a small amount. It is difficult to determine the exact reason for this, but the designs might simply be different local minima. Another explanation can be given by the crisp boundaries of design D having less intermediate densities, and thus less penalized material properties.

5.5.6 Optimization in 3D

Also several optimizations are run in 3D, for which the design case as depicted in Fig. 5.13 is used. The case has 6 controllers for positioning in each degree of freedom. The inputs and outputs are combined from different individual actuators and sensors, analogous to

the 2D case (Fig. 5.5).

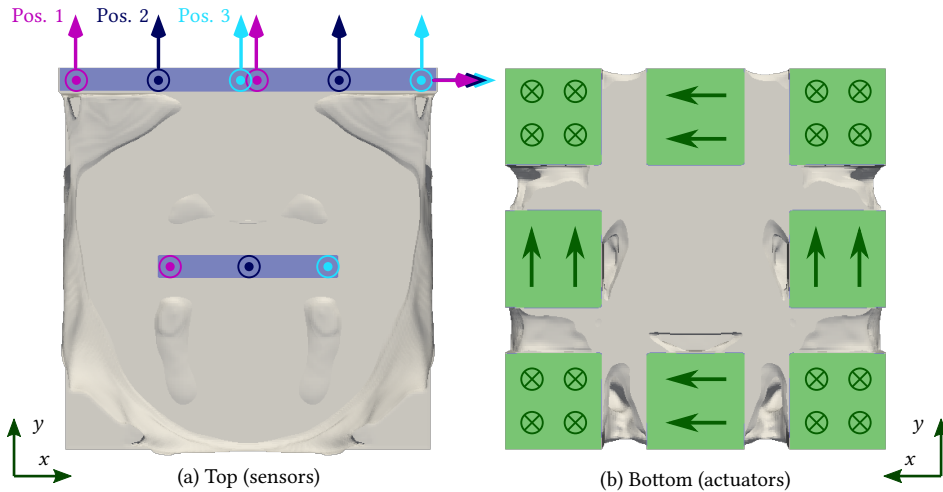


Figure 5.13: The input and output loadcases for the 3D optimization with three relative sensor positions ($N_{\text{pos}} = 3$). As in the 2D case (Fig. 5.5), the loads and measurements are combined over multiple actuators to obtain 6 degrees of freedom for both input and output. The domain measures $400 \times 400 \times 100$ mm and is discretized into $192 \times 192 \times 48$ elements. Areas shaded green represent non-design domains corresponding to actuators, made out of neodymium. Each actuator has dimensions $100 \times 100 \times 25$ mm. The blue-shaded areas are non-design domains for the sensors. The large sensor domain measures $383 \times 25 \times 25$ mm and the small one $183 \times 25 \times 13$ mm.

Again, several variations are tested:

- A. As a baseline for performance, the structure is optimized for maximum eigenfrequencies (f_{Ω} , Eq. 5.56). Subsequently, the controller is tuned using the formulation in Eq. 5.60.
- B. An integrated controller-structure topology optimization is performed for one single relative sensor position $N_{\text{pos}} = 1$. In this case, only the central sensor position is used (Fig. 5.13), and the non-design domains corresponding to the sensors are shortened (to 225 and 25 mm).
- C. Also an integrated controller-structure optimization, but with multiple relative sensor positions $N_{\text{pos}} = 3$.
- D. Using the robust formulation (Chapter 4), the stage is optimized for 3 relative sensor positions. The same settings as in the 2D robust example are used.

The resulting designs are shown in Fig. 5.14 and their performances are visualized in Fig. 5.15, with exception of design B. This design has been optimized for a different number of sensor positions than the other designs and therefore cannot directly be compared. Its bandwidths are $\omega_b = [623 \ 559 \ 470 \ 472 \ 675 \ 685]$ Hz, which is substantially higher than all the designs optimized for $N_{\text{pos}} = 3$.

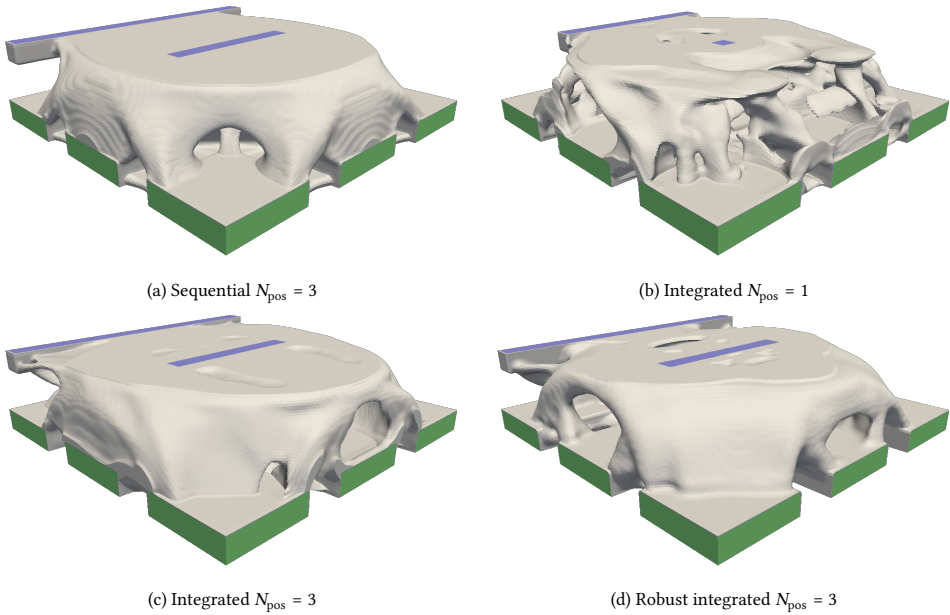


Figure 5.14: Designs for the 3D case variations. The designs are extracted in Paraview (Ahrens *et al.*, 2005) by taking the iso-surfaces of the density field at 0.5 with linear interpolation.

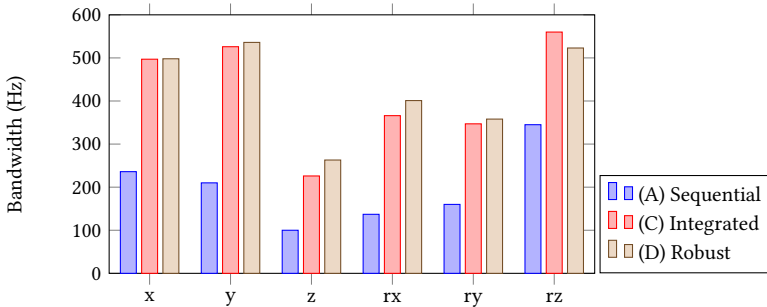


Figure 5.15: Comparison in bandwidth performance for the different designs having $N_{\text{pos}} = 3$. The notation ‘rx’ means rotation around the x-axis.

From the bandwidth comparison in Fig. 5.15 can again be seen that the performance of the sequentially optimized design (A) is significantly lower than the designs from the integrated optimizations (C and D). The improvements of the integrated optimization range from +62% up to +167%, compared to the design optimized for maximum eigenfrequencies. The lowest bandwidth in all the designs is in the z-direction. This can be compared to the situation in the 2D examples (Table 5.3), where the bandwidth for the y-direction was lowest. Here, the aspect ratio is such that the eigenmodes exhibit large deformations in the z-direction.

Like in the 2D results, the performance (Fig. 5.15) of the robustly optimized design

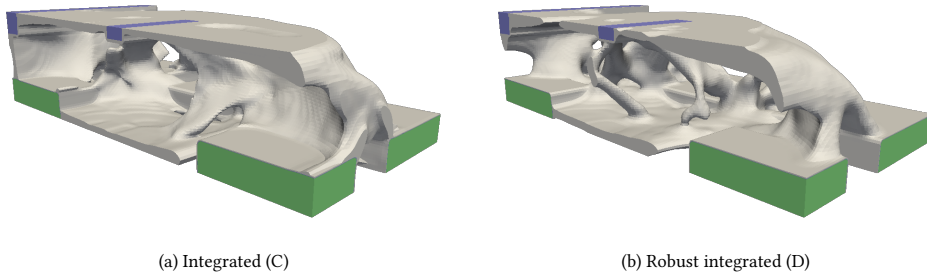


Figure 5.16: The 3D designs after integrated optimization for $N_{\text{pos}} = 3$ with cut-away of the left half, showing the internal structure of the domain.

(D) is mostly similar to that of the design optimized without robust formulation (C). Only bandwidth for the rotation around the z-axis shows a decrease, but the other bandwidths are equal or increased when using the robust formulation. Different than the 2D cases, the structures of the robust (D) and non-robust (C) designs look quite different (Fig. 5.14). Also the internal structure of the two designs is quite different, as can be seen in Fig. 5.16. This indicates the designs converge to different local optima.

The singular values of the sensitivity function are shown in Fig. 5.17. The sequentially optimized design (A) has a lower bandwidth than the others, which is recognized by the poor disturbance rejection properties at low frequencies as compared to the other designs. Another significant difference is that the sequentially optimized design exhibits far less peaks touching the limit of $1/\mu$. In design A, only two of the robustness constraints are active out of a total of 60, while for design C there are 21 active (as counted for constraint values above -10^{-1}).

In Fig. 5.17b can be seen that the design optimized with one relative sensor position (B) is not satisfying all constraints. A peak that is considerably higher the limit of $1/\mu$ can be identified at a high frequency. This is likely caused by mode switching with modes outside of the calculated range. In the 3D examples, $N = 20$ eigenmodes are calculated, so when mode 21 (outside of the spectrum) switches with mode 20 a new peak can arise. Since 20 eigenmodes are considered for these optimizations, the resulting designs do not assure limitation of the peaks for mode 21 and onward.

Comparing the sensitivity functions for the robustly optimized design (D, Fig. 5.17d) with those of the non-robust design (C, Fig. 5.17c), the amplitudes of the high-frequency peaks are noticeably lower. This is because the worst-case value of the eroded, nominal, and dilated designs is optimized. It provides a robustness against geometric deviations, which seems to affect high frequencies more than low frequencies. This is a benefit of the robust method that also inspires greater confidence in the behavior of eigenmodes outside of the calculated spectrum.

The computation time required for these optimizations is significant, even with the reduction in number of constraints and approximate sensitivities. All the linear systems are iteratively solved using the BiCGStab method (Saad, 2003), preconditioned by the generalized algebraic multigrid (GAMG) method, which both are implemented in PETSc (Balay et al., 2019). The cases are all run on 48 cores of a system with Intel Xeon Gold 6240 pro-

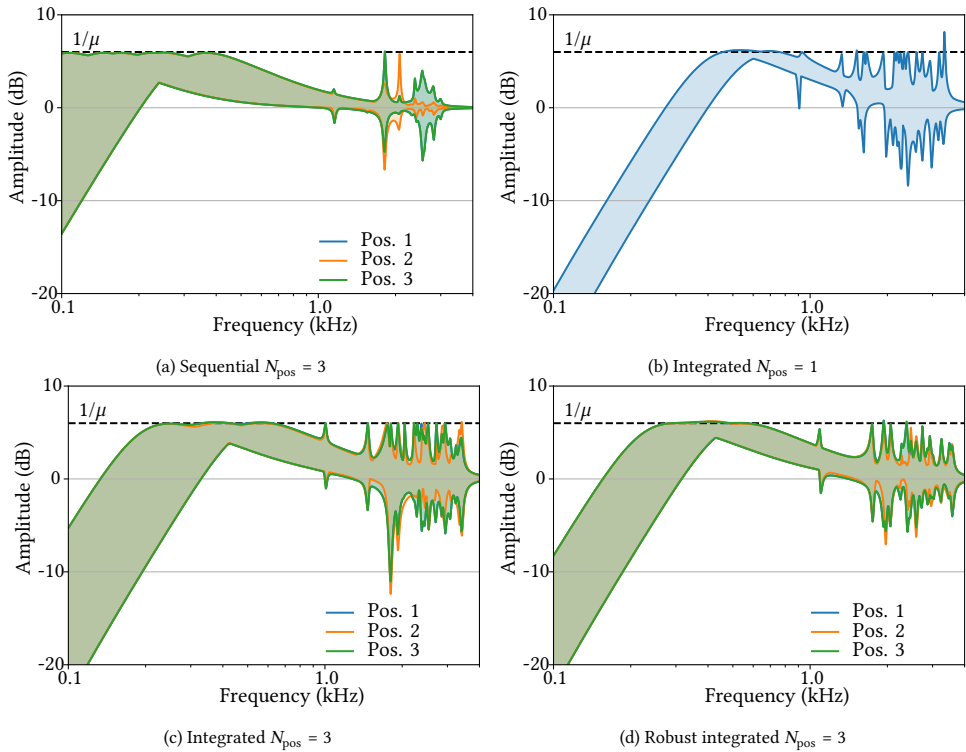


Figure 5.17: Sensitivity plots of the extreme singular values for the different 3D designs.

processors. In Fig. 5.18, a graphical overview of the calculation times is shown, corresponding to different methods presented. The most significant reduction of computational time is caused by the approximation of the design sensitivities. Consistent sensitivities take on average 24.5 min to calculate¹, while the approximated sensitivities only take 5.9 s, which is a difference of several orders of magnitude. Even with the investment of calculating the augmentation basis, which takes about 15 min, a computational gain is already obtained for one constraint. In the considered case (with \mathcal{L}_∞ constraints), there are 66 constraints in total, which results in a computational gain of almost two orders (a factor 77) for calculating all the design sensitivities, including the construction of the augmentation basis.

The local \mathcal{L}_∞ norm constraints further reduce the total computation time required, by limiting the number of constraints. Instead of 360 constraints for robustness when constraining the diagonal entries, only 60 robustness constraints are required for the \mathcal{L}_∞ approach. Combining the two methods, the total time required to perform one design iteration reduces from 8983 min (over 149 h) to 37 min, which is a speedup of a factor 243. These improvements in computation time thus enable the large-scale topology optimization of 3D structures for closed-loop performance, which was infeasible to do before.

¹Only a few of these design sensitivities were calculated as it is deemed infeasible to do a full design iteration.

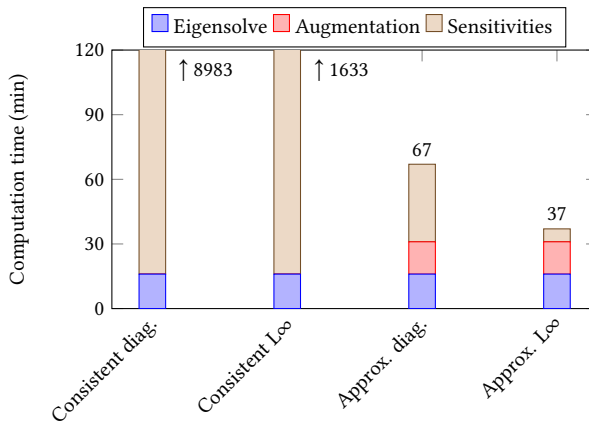


Figure 5.18: Comparison in calculation time for the first design iteration for the 3D case with $N_{\text{pos}} = 3$. As a reference, the optimization maximizing the first three eigenfrequencies takes only 4.5 min per iteration. Approximated and consistent sensitivities are compared, and also the type of constraints is compared (diagonal entries only versus local constraints on the L_∞ norms). The bars of the consistent sensitivities are clipped, but reach 8983 and 1633 min for the diagonal and L_∞ constraints, respectively. Timings are obtained using 48 cores of a system with Intel Xeon Gold 6240 processors.

5.6 Discussion

For the current work, constraints are presented that enable limitation of the \mathcal{H}_∞ norm corresponding to the sensitivity function. However, there are many other performance and robustness measures in control theory that can be incorporated. The presented framework may be extended by, for instance, a weighted sensitivity function or a mixed sensitivity formulation (Skogestad and Postlethwaite, 2001), which incorporates the complementary sensitivity function as well. It is suggested to further study robust control theory and structured singular values (μ -analysis), which incorporate the robustness effect of parametric uncertainties in the system (Zhou *et al.*, 1996). Also the effect of time delay is important for further research, as it may significantly alter the behavior of the system at high frequencies.

The number of different relative sensor positions incorporated into the optimization is small for the numerical examples (up to 3). However, accuracy is usually required over an entire surface for realistic applications. The presented implementation may become difficult to use for a large number of sensor/accuracy positions, as it directly results in more constraints and extra computation time. Therefore, it is suggested to look into different methods (*e.g.* aggregation Kennedy and Hicken, 2015) to incorporate many precision points.

Furthermore, in the present work, a new basis of Krylov vectors is calculated each design iteration. Since a gradient-based optimization is used, the designs will not differ much from iteration to iteration, in particular in the later stage of the optimization process. This means that also the Krylov vectors will be similar to those of the previous iteration. By adaptively updating the augmentation basis or by using reanalysis techniques (Kirsch, 2010), further reduction of computation time can be expected.

Also the optimization algorithm can potentially be further refined. The integrated controller-structure optimization contains two types of variables. The control variables are analytically related to the constraints and only involve reduced-order models, which means higher-order derivatives can be calculated. By combining MMA for the density variables with, for instance, sequential quadratic programming (SQP) for the control variables, a better convergence might be achieved with less oscillations and less design iterations.

5.7 Conclusion

In this work, two new methods are introduced that enable large-scale 3D topology optimization for integrated design of MIMO controllers and structures, with performance requirements on the \mathcal{H}_∞ norm of the sensitivity function. The first method efficiently allows constraints to be placed on the \mathcal{H}_∞ norm of the sensitivity function for gradient-based optimization. Local circle approximations are constructed for the Nyquist curves of the sensitivity function, after which upper bounds of local \mathcal{L}_∞ norms can be calculated. A correction scheme allows all the local \mathcal{L}_∞ norms to be constrained below an exact threshold. This effectively results in limitation of the \mathcal{H}_∞ norm, thus ensuring MIMO disturbance rejection and robustness. The local approximation of the \mathcal{H}_∞ norm prevents convergence problems due to multi-modality and non-differentiability in gradient-based optimization.

The second proposed method addresses a main computational bottleneck in integrated controller-structure optimization: the time required for calculation of the adjoint eigenmode design sensitivities. In typical MIMO problems, many adjoint solution vectors are required, which are costly to compute. Therefore, a reduced-order model, containing eigenmodes augmented with Krylov vectors, is used to approximate the adjoint solution vectors. This requires an investment in calculation of the Krylov vectors once each design iteration, but enables the efficient approximation of many adjoint solution vectors. Using the design sensitivity approximations, the integrated controller-structure topology optimization of large-scale 3D cases is enabled.

The proposed local approximations of the \mathcal{H}_∞ norm are demonstrated using design cases of MIMO motion stages, with three control loops in 2D and six in 3D. The structure and controller are simultaneously optimized for weighted maximum bandwidth and eigenfrequencies subject to closed-loop stability and local \mathcal{L}_∞ norm constraints on the sensitivity function. Compared to designs optimized solely for maximum eigenfrequencies, the system performance is significantly improved, increasing bandwidths in all control loops by 62 – 167% for the demonstrated case in 3D. Also using the robust formulation results in comparable performance improvements, while incorporating geometric uncertainties and imposing a minimum feature size. In the existing work of [Van der Veen et al. \(2017\)](#), only the diagonal entries of the sensitivity function are constrained. Here, it is shown that this results in an optimized controller and structure with poor MIMO disturbance rejection properties, which was the initial motivation to use the \mathcal{H}_∞ norm. Additionally, the (approximated) \mathcal{H}_∞ norm provides a natural aggregation for MIMO systems. This makes the number of constraints independent of the number of inputs or outputs of the system, significantly reducing the number of constraints and thereby also the computational effort.

For the large-scale 3D demonstration case with six control loops, using both proposed

methods, the time to perform a single design iteration for the integrated optimization is 37 min. Without the approximation of the design sensitivities this would take 44 times longer, and without also approximation of the \mathcal{H}_∞ norm even 243 times longer (over 149 h for a single design iteration). This clearly establishes the effectiveness of the approach. It is also demonstrated that adding a few Krylov vectors already results in design sensitivities accurate enough for topology optimization. By adding additional Krylov vectors, the accuracy of the design sensitivities can be improved, thus balancing computation time with accuracy. An adaptive scheme in which accuracy is increased as the optimization process converges could be considered in future work.

The current optimizations are focused on the limitation of the \mathcal{H}_∞ norm corresponding to the sensitivity function. In robust control, the \mathcal{H}_∞ norm is also used to analyze the effect of uncertainties in the system. Possibly, the framework can be extended to perform integrated controller-structure optimization for such cases as well.

6

Conclusions

The main goal of this thesis was the development of methods that enable integrated controller and topology optimization for large-scale and 3D systems with MIMO control, for the application of motion system design. Many different aspects have been explored towards this goal. First of all, practical manufacturing considerations are required to ensure that the optimized results are also producible. Using additive manufacturing, a demonstrator was physically realized and also experimentally validated. Secondly, topology optimization requires a significant amount of computational time. Therefore, efficient methods must be established to enable the optimization to finish within a reasonable amount of time. Finally, specific techniques for integrated controller-structure optimization are presented for both SISO and MIMO systems.

6.1 Manufacturing considerations

The manufacturing of a topology optimized stage is done using a multi-step process, for instance, using additive manufacturing, followed by milling to remove support material and improve surface quality, and finally the assembly of actuators and other components. To prevent manual alterations to the optimized design, and thereby potentially harming its performance, the manufacturing steps must be included into the optimization. In Chapter 2, a systematic process is presented that incorporates the steps of the manufacturing process into the optimization. Several small contributions include the geometric mapping of components into the mesh, ensuring interfaces and connectivity for these components, and limiting the amount of support material required in the design. Furthermore, an overhang filter is used to ensure a maximum overhang angle, allowing the design to be printed. Based on an existing overhang filter, improvements are proposed that enable extended freedom in the choice of print orientation and overhang angle.

A robust formulation is often used in topology optimization to ensure performance levels under manufacturing variations and enable control over the minimum feature size in a design. After evaluation of performance for multiple geometrically perturbed designs (eroded and dilated), the worst-case performance is used to incorporate a measure of robustness into the optimization. This is used in Chapters 2, 4, and 5 to prevent the appearance of very thin and fragile structures in the design. Although the robust for-

mulation imposes restriction on the design, from the MIMO studies in Chapter 5 it can be concluded that this has no negative effect on performance. An explanation is that the considered problem features multiple local optima with similar performance, and the robust formulation helps to focus on variants with favorable manufacturability characteristics. Finally, the topology optimization incorporating manufacturing considerations is demonstrated on an industrial motion stage, optimized for maximum eigenfrequencies. The design, obtained in a fraction (25 hours) of the conventional design time, is almost directly manufacturable without manual adaptations. It is printed by laser powder-bed fusion, after which it is milled, assembled, and experimentally validated. Its measured eigenfrequencies are within 1% of the expected values, and its performance is increased by 15% compared to a conventional design. It can be concluded that topology optimization in combination with additive manufacturing is viable for industrial applications, and can enable unprecedented performance levels.

6.2 Computational effort

Topology optimization is computationally very intensive, especially for problems where modal analyses are needed to describe the system dynamics. Parallel computing is a widely applied method of reducing the time required for optimization. This is considered in Chapter 2, where a uniform voxel-grid is used for an efficient geometric representation of the design. Using a parallel implementation, an eigenfrequency maximization on a very detailed mesh¹ can be performed in only 25 hours with 192 CPU cores. Furthermore, the use of the robust formulation requires additional computational effort. Because multiple perturbed designs have to be analyzed, it typically leads to an increase of computational cost by a factor 3. In Chapter 2, the mass properties of the dilated design and stiffness properties of the eroded design are combined to estimate a worst-case performance with only one analysis instead of three. A further generalization is presented in Chapter 4, where reduced-order models are generated for each of the perturbed designs, based on the eigenmodes of the nominal design. Thus besides requiring only one modal analysis instead of three, these reduced-order models can be used to describe the (approximate) dynamic behavior of the perturbed designs in a more flexible manner.

Next to the modal analysis of the system, an effective topology optimization also requires calculation of design sensitivities. To calculate these for the eigenmodes is computationally extremely costly, as large saddlepoint problems need to be solved for the eigenmodes involved in each constraint. The calculation of the saddlepoint problems is avoided in Chapter 3 by ignoring the design dependence with respect to the model reduction basis (*i.e.*, the eigenmodes). It is shown that the design sensitivities remain accurate when the reduction basis is augmented with quasi-static correction vectors based on the system input and output. This results in a computational gain of almost an order of magnitude in the numerical examples. However, a limitation is that the addition of correction vectors introduces fictitious eigenfrequencies in the reduced-order model that can potentially destabilize a closed-loop system. Therefore, a different method is presented in Chapter 5 to approximate the eigenmode design sensitivities. The expensive saddlepoint problems are approximately solved by a reduced-order model augmented with Krylov vectors, which

¹The mesh consists of almost 9 million elements/voxels.

are based on the system input(s) and output(s). When applied to the 3D topology optimization problems for integrated system performance, speedups up to a factor 44 are achieved. Additionally, the computational effort can be balanced with accuracy by adding a different number of Krylov vectors. Given these significant computational gains, it is concluded that these methods enable the efficient large-scale 3D topology optimization for the integrated system performance.

6.3 Integrated controller-structure optimization

The final challenge is to effectively optimize system performance by integrated controller-structure optimization. A basic method of optimizing for system performance is to limit resonances of the structure, which is presented in Chapter 3, although it does not include a controller. By calculating the resonance frequencies and imposing constraints on the dynamic response amplitudes corresponding to these frequencies, the resonance peaks can effectively be limited below an upper bound. Unfortunately, this approach provides limited insight into closed-loop behavior and is known to be conservative. Peak frequencies cannot be calculated explicitly for closed-loop systems, which prevents using the method of Chapter 3 in integrated controller-structure optimization. Therefore, another approach is explored in Chapter 4, which is focused on integrated controller-structure optimization using the open-loop Nyquist curve. Local approximations are constructed to the characteristic circular shapes in the Nyquist curve, which are caused by flexible eigenmodes. These circular approximations allow for simple geometric constraints in the complex domain, effectively restricting the global shape of the Nyquist curve. In this way, closed-loop stability and disturbance rejection properties (*i.e.* modulus margin) can be enforced for SISO systems. Numerical examples show significantly better performance for designs optimized with this integrated approach, with bandwidths up to 350% higher as compared to structures simply optimized for maximum eigenfrequencies. Therefore, a clear conclusion is that integrated controller-structure optimization based on closed-loop system characteristics can achieve significantly higher performance levels in comparison to the eigenfrequency maximization approach.

The SISO approach based on open-loop Nyquist curves cannot be used for MIMO systems, as it does not incorporate the closed-loop interaction and coupling with the other control loops. Therefore, the method is extended to MIMO systems in Chapter 5. Instead of local circular approximations on the open-loop Nyquist curves, they can also be constructed on closed-loop Nyquist curves. These approximations can directly be used in optimizations with constraints on individual entries of the sensitivity function to ensure disturbance rejection properties. However, it is shown that this approach of constraining a limited number of entries results in designs with very high singular values of the sensitivity function, which characterizes a high sensitivity to simultaneous disturbances on multiple channels. Moreover, the computational cost scales directly with the number of entries constrained. To address these issues, approximate local upper bounds of the \mathcal{H}_∞ norm (*i.e.* the peak maximum singular value) are constructed. Using the local circle approximations, maximum Frobenius norms can be approximated, which provide local upper bounds to the maximum singular values. An adaptive correction factor is used to correct the error and enable limitation to an exact upper limit. Additionally, the Frobenius norm provides a natural way of constraint aggregation, reducing the number of constraints six-fold in 3D,

thus providing additional computational gain. For 3D numerical examples with control in six degrees of freedom, designs are generated with bandwidths up to 150% higher than designs optimized for eigenfrequencies, while satisfying the MIMO disturbance rejection requirements on the \mathcal{H}_∞ norm. It is therefore concluded that using the proposed formulation based on the Frobenius norm is superior both in numerical performance and accuracy. With this final extension, the initial goal of this dissertation is fulfilled and designs can efficiently be obtained in 3D for integrated MIMO system performance.

6.4 Recommendations

Robust control In this dissertation, the focus is on rejecting disturbances entering the control loop. However, in reality there may be many other factors impeding the performance of a system, such as geometric differences causing a shift of mass or stiffness, offsets in loads or sensing position, or time delay. Especially at high frequencies the dynamic properties may be completely different in reality than as modeled due to such aspects. It is suggested to incorporate the effect of such uncertainties into the optimization to ensure more robust designs. The presented method using the \mathcal{H}_∞ norm in Chapter 5 may be seen as an initial step towards the more general methods that are found in the field of robust control Zhou *et al.* (1996).

Accuracy at many positions Many applications require accuracy over entire surfaces instead of only at a small number of positions. In the methods presented in this dissertation, addition of more locations for accuracy results in a growing amount of constraints. Therefore, ensuring accuracy over an entire surface by discrete locations becomes impractical, as it results in a very large number of constraints. To incorporate the effect of spatial accuracy in an efficient manner, further research is required.

Adaptive updating of reduced-order model While large computational gains are presented in this dissertation, the integrated controller-structure topology optimization still requires more than 8 times the computational effort as compared to an eigenfrequency maximization. Faster solution times enable optimizations with finer design resolution or with more constraints (*e.g.* more sensor positions). Gradient-based optimizations are characterized by relatively small design differences between iterations. This means that, for instance, eigenvectors and Krylov vectors will be similar to those in the previous iteration, especially in the later stage of the optimization where design changes usually becomes smaller. Significant computational gains might be achieved by adaptively updating reduced-order models or by correcting the eigenvectors from iteration to iteration.

Widening range of applications Given the gains that were demonstrated in motion system design, it is of clear interest to explore further design problems that require an integrated approach. Next to problems involving structural dynamics, also *e.g.* the thermomechanical behavior of a system is often subject to stringent requirements that could be included. In a way, this dissertation only forms the beginning of a wide area of applications to explore, with the combination of the design freedom offered by both topology optimization and additive manufacturing potentially allowing significant benefits.

A

Appendix

A.1 Robust formulation for eigenfrequencies

The design sensitivities of eigenfrequency Ω_i (Eq. 2.14) with respect to the Young's modulus E_j and mass density ρ_j are (from, e.g., Haftka, 1990)

$$\begin{aligned}\frac{\partial \Omega_i}{\partial E_j} &= \frac{1}{2\Omega_i} \boldsymbol{\phi}_i^T \frac{\partial \mathbf{K}}{\partial E_j} \boldsymbol{\phi}_i, \\ \frac{\partial \Omega_i}{\partial \rho_j} &= -\frac{\Omega_i}{2} \boldsymbol{\phi}_i^T \frac{\partial \mathbf{M}}{\partial \rho_j} \boldsymbol{\phi}_i.\end{aligned}\tag{A.1}$$

The sensitivities of the stiffness and mass matrix (Eq. 2.13) relate to the unit element matrices \mathbf{K}_0 and \mathbf{M}_0 through the assembly operation, which are positive semi-definite and positive definite, respectively. This implies that the sensitivities of the assembled system matrices $\frac{\partial \mathbf{K}}{\partial E_j}$ and $\frac{\partial \mathbf{M}}{\partial \rho_j}$ are positive semi-definite.

$$\begin{aligned}\boldsymbol{\phi}_i^T \frac{\partial \mathbf{K}}{\partial E_j} \boldsymbol{\phi}_i &\geq 0 \quad \forall \quad \boldsymbol{\phi}_i \neq \mathbf{0}, \\ \boldsymbol{\phi}_i^T \frac{\partial \mathbf{M}}{\partial \rho_j} \boldsymbol{\phi}_i &\geq 0 \quad \forall \quad \boldsymbol{\phi}_i \neq \mathbf{0}.\end{aligned}\tag{A.2}$$

Generally, these quadratic forms are positive, as they are only equal to zero in specific cases of element deformation, such as no deformation or a rigid body deformation of element j . Additionally, the eigenfrequency Ω_i is positive, which means the following relations hold

$$\frac{\partial \Omega_i}{\partial E_j} \geq 0 \quad \text{and} \quad \frac{\partial \Omega_i}{\partial \rho_j} \leq 0.\tag{A.3}$$

From these it is evident that increasing the Young's modulus will generally result in higher eigenfrequencies and increasing the mass generally results in lower eigenfrequencies.

A

A.2 Circle in the complex domain

Below, the proof of the relations in Eq. 4.5 is provided. It additionally proves that the single first-order mode approximation of Eq. 4.3 describes an exact circle in the complex domain. A generalized circle is defined by the parametric equation

$$Aw\bar{w} + \bar{\gamma}w + \gamma\bar{w} + D = 0, \quad (\text{A.4})$$

with variable $w \in \mathbb{C}$, parameters $A, D \in \mathbb{R}$, $\gamma \in \mathbb{C}$, and $\bar{\cdot}$ denoting the complex conjugate. Depending on the values of the parameters, the parametric equation either describes a circle or a line (Schwerdtfeger, 1979). In case of a circle, its midpoint and radius are defined by respectively

$$w_0 = -\frac{\gamma}{A} \quad \text{and} \quad R^2 = \frac{|\gamma|^2}{A^2} - \frac{D}{A}. \quad (\text{A.5})$$

The Nyquist curve is evaluated over a line in the direction of the imaginary axis as $s = j\omega$. This line can be described using the generalized circle equation (with $A = 0$, $\gamma = 1 + 0i$, and $D = 0$) and using the complex variable s as

$$s = j\omega \iff s + \bar{s} = 0. \quad (\text{A.6})$$

The approximated transfer function $\tilde{L}_i(s)$ of Eq. 4.3 is a Möbius transformation (Schwerdtfeger, 1979), which maps the line from the s -domain to a circle in the $L(s)$ -domain. The parametric equation for the transformed circle can be found using the inverse mapping, with the constant offset \check{L}_i removed, as

$$w = \tilde{L}_i(s) - \check{L}_i = \frac{p_i}{s - \lambda_i} \iff s = \frac{p_i + \lambda_i w}{w}, \quad (\text{A.7})$$

with the mapped variable $w \in \mathbb{C}$. Substituting this into Eq. A.6 and rewriting, yields the parametric equation of the mapped curve as

$$\frac{p_i + \lambda_i w}{w} + \frac{\bar{p}_i + \bar{\lambda}_i \bar{w}}{\bar{w}} = 0, \quad (\text{A.8})$$

which can be rearranged to another generalized circle equation as

$$(\lambda_i + \bar{\lambda}_i)w\bar{w} + p_i\bar{w} + \bar{p}_i w = 0. \quad (\text{A.9})$$

Using Eq. A.5, the midpoint relative to the offset \check{L}_i and the radius respectively become

$$w_{0,i} = -\frac{p_i}{2\text{Re}(\lambda_i)} \quad \text{and} \quad R_i = \frac{|p_i|}{2|\text{Re}(\lambda_i)|}. \quad (\text{A.10})$$

Again adding the constant offset \check{L}_i that was removed in Eq. A.7, the midpoint of the Nyquist curve $\tilde{L}_i(j\omega)$ is obtained as

$$X_i = \check{L}_i - \frac{p_i}{2\text{Re}(\lambda_i)}. \quad (\text{A.11})$$

Bibliography

References

- Aage N, Andreassen E, Lazarov BS, Sigmund O (2017). Giga-voxel computational morphogenesis for structural design. *Nature*, 550:84–86, doi:[10.1038/nature23911](https://doi.org/10.1038/nature23911)
- Abramovitch DY, Andersson SB, Pao LY, Schitter G (2007). A tutorial on the mechanisms, dynamics, and control of atomic force microscopes. In: *Proceedings of the American Control Conference*, New York, USA, pp 3488–3502, doi:[10.1109/ACC.2007.4282300](https://doi.org/10.1109/ACC.2007.4282300)
- Additive Industries (2021). *MetalFAB1 industrial 3D printer*. URL <https://www.additiveindustries.com/systems/metalfab1>, accessed: October 28, 2021
- Ahrens J, Geveci B, Law C (2005). Paraview: An end-user tool for large-data visualization. In: *Visualization Handbook*, Elsevier, chap 36, pp 717–731
- Albers A, Otnad J (2010). Integrated structural and controller optimization in dynamic mechatronic systems. *Journal of Mechanical Design*, 132(4):041008, doi:[10.1115/1.4001380](https://doi.org/10.1115/1.4001380)
- Allison JT, Herber DR (2014). Multidisciplinary design optimization of dynamic engineering systems. *AIAA Journal*, 52(4):691–710, doi:[10.2514/1.J052182](https://doi.org/10.2514/1.J052182)
- Anderson BO, Moore JB (1989). *Optimal control: linear quadratic methods*. Prentice-Hall International, Inc.
- Antoulas AC (2004). Approximation of large-scale dynamical systems: An overview. In: *IFAC Proceedings Volumes*, Osaka, Japan, vol 37, pp 19–28, doi:[10.1016/S1474-6670\(17\)31584-7](https://doi.org/10.1016/S1474-6670(17)31584-7)
- Åström KJ, Murray RM (2008). *Feedback Systems: An Introduction for Scientists and Engineers*, 2nd edn. Princeton University Press
- Balay S, Abhyankar S, Adams MF, Brown J, Brune P, Buschelman K, Dalcin L, Dener A, Eijkhout V, Gropp WD, Karpeyev D, Kaushik D, Knepley MG, May DA, McInnes LC, Mills RT, Munson T, Rupp K, Sanan P, Smith BF, Zampini S, Zhang H, Zhang H (2019). *PETSc web page*. URL <https://www.mcs.anl.gov/petsc>
- Bendsøe MP, Kikuchi N (1988). Generating optimal topologies in structural design using a homogenization method. *Computer Methods in Applied Mechanics and Engineering*, 71(2):197–224, doi:[10.1016/0045-7825\(88\)90086-2](https://doi.org/10.1016/0045-7825(88)90086-2)
- Bendsøe MP, Sigmund O (2003). *Topology optimization: Theory, methods and applications*, 1st edn. Springer-Verlag, Berlin, Heidelberg

- Benzi M, Golubt GH, Liesen J (2005). Numerical solution of saddle point problems. *Acta Numerica*, 14:1–137, doi:[10.1017/S0962492904000212](https://doi.org/10.1017/S0962492904000212)
- Besselink B, Tabak U, Lutowska A, van de Wouw N, Nijmeijer H, Rixen DJ, Hochstenbach ME, Schilders WHA (2013). A comparison of model reduction techniques from structural dynamics, numerical mathematics and systems and control. *Journal of Sound and Vibration*, 332(19):4403–4422, doi:[10.1016/j.jsv.2013.03.025](https://doi.org/10.1016/j.jsv.2013.03.025)
- Bruinsma NA, Steinbuch M (1990). A fast algorithm to compute the \mathcal{H}_∞ -norm of a transfer function matrix. *Systems & Control Letters*, 14(4):287–293, doi:[10.1016/0167-6911\(90\)90049-Z](https://doi.org/10.1016/0167-6911(90)90049-Z)
- Bruns TE, Tortorelli DA (2001). Topology optimization of non-linear elastic structures and compliant mechanisms. *Computer Methods in Applied Mechanics and Engineering*, 190(26-27):3443–3459, doi:[10.1016/S0045-7825\(00\)00278-4](https://doi.org/10.1016/S0045-7825(00)00278-4)
- Bruns TE, Tortorelli DA (2003). An element removal and reintroduction strategy for the topology optimization of structures and compliant mechanisms. *International Journal for Numerical Methods in Engineering*, 57(10):1413–1430, doi:[10.1002/nme.783](https://doi.org/10.1002/nme.783)
- Budynas R, Nisbett K (2006). *Shigley's Mechanical Engineering Design*, 8th edn. McGraw-Hill
- Christensen PW, Klarbring A (2009). *An introduction to structural optimization*. Springer
- Craig RR, Kurdila AJ (2006). *Fundamentals of structural dynamics*, 2nd edn. John Wiley & Sons, Hoboken, New Jersey
- Delissen AATM, van Keulen F, Langelaar M (2020). Efficient limitation of resonant peaks by topology optimization including modal truncation augmentation. *Structural and Multidisciplinary Optimization*, 61:2557–2575, doi:[10.1007/s00158-019-02471-9](https://doi.org/10.1007/s00158-019-02471-9)
- Delissen AATM, Boots E, Laro D, Kleijnen H, van Keulen F, Langelaar M (2022). Realization and assessment of metal additive manufacturing and topology optimization for high-precision motion systems. *Additive Manufacturing*, 58:103012, doi:[10.1016/j.addma.2022.103012](https://doi.org/10.1016/j.addma.2022.103012)
- Díaz AR, Kikuchi N (1992). Solutions to shape and topology eigenvalue optimization problems using a homogenization method. *International Journal for Numerical Methods in Engineering*, 35(7):1487–1502, doi:[10.1002/nme.1620350707](https://doi.org/10.1002/nme.1620350707)
- Dickens JM, Nakagawa JM, Wittbrodt MJ (1997). A critique of mode acceleration and modal truncation augmentation methods for modal response analysis. *Computers and Structures*, 62(6):985–998, doi:[10.1016/S0045-7949\(96\)00315-X](https://doi.org/10.1016/S0045-7949(96)00315-X)
- Doyle JC (1978). Guaranteed margins for LQG regulators. *IEEE Transactions on Automatic Control*, 23(4):756–757, doi:[10.1109/TAC.1978.1101812](https://doi.org/10.1109/TAC.1978.1101812)
- Doyle JC, Glover K, Khargonekar PP, Francis BA (1989). State-space solutions to standard \mathcal{H}_2 and \mathcal{H}_∞ control problems. *IEEE Transactions on Automatic Control*, 34(8):831–847, doi:[10.1109/9.29425](https://doi.org/10.1109/9.29425)

- Du J, Olhoff N (2007a). Minimization of sound radiation from vibrating bi-material structures using topology optimization. *Structural and Multidisciplinary Optimization*, 33:305–321, doi:[10.1007/s00158-006-0088-9](https://doi.org/10.1007/s00158-006-0088-9)
- Du J, Olhoff N (2007b). Topological design of freely vibrating continuum structures for maximum values of simple and multiple eigenfrequencies and frequency gaps. *Structural and Multidisciplinary Optimization*, 34:91–110, doi:[10.1007/s00158-007-0101-y](https://doi.org/10.1007/s00158-007-0101-y)
- Fathy HK, Reyer JA, Papalambros PY, Ulsoy AG (2001). On the coupling between the plant and controller optimization problems. In: *Proceedings of the American Control Conference*, Arlington, USA, pp 1864–1869, doi:[10.1109/ACC.2001.946008](https://doi.org/10.1109/ACC.2001.946008)
- Fesina MI, Krasnov AV, Gorina LN (2017). The effectiveness of the suppression of low frequency acoustic resonances with porous sound absorbing structures of multifunctional upholstery materials of car body interior. *Procedia Engineering*, 176:159–168, doi:[10.1016/j.proeng.2017.02.284](https://doi.org/10.1016/j.proeng.2017.02.284)
- Foley JD, van Dam A, Feiner SK, Hughes JF, Phillips RL (1993). *Introduction to Computer Graphics*. Addison-Wesley Professional
- Garcia-Sanz M (2019). Control co-design: An engineering game changer. *Advanced Control for Applications: Engineering and Industrial Systems*, 1(1):e18, doi:[10.1002/adc2.18](https://doi.org/10.1002/adc2.18)
- Gawronski WK (2004). *Advanced Structural Dynamics and Active Control of Structures*. Springer-Verlag, New York, New York, USA
- Gaynor AT, Guest JK (2014). Topology optimization for additive manufacturing: Considering maximum overhang constraint. In: *15th AIAA/ISSMO Multidisciplinary Analysis and Optimization Conference*, Atlanta, USA, pp 1–8, doi:[10.2514/6.2014-2036](https://doi.org/10.2514/6.2014-2036)
- Gaynor AT, Johnson TE (2020). Eliminating occluded voids in additive manufacturing design via a projection-based topology optimization scheme. *Additive Manufacturing*, 33:101149, doi:[10.1016/j.addma.2020.101149](https://doi.org/10.1016/j.addma.2020.101149)
- Geradin M, Rixen DJ (2015). *Mechanical Vibrations: Theory and Application to Structural Dynamics*, 3rd edn. John Wiley & Sons, Ltd
- Giesy DP, Lim KB (1993). \mathcal{H}_∞ norm sensitivity formula with control system design applications. *Journal of Guidance, Control, and Dynamics*, 16(6):1138–1145, doi:[10.2514/3.21138](https://doi.org/10.2514/3.21138)
- Golub GH, van Loan CF (1996). *Matrix computations*, 3rd edn. Johns Hopkins University Press
- Grimme EJ (1997). *Krylov projection methods for model reduction*. PhD thesis, University of Illinois
- Guest JK, Zhu M (2012). Casting and milling restrictions in topology optimization via projection-based algorithms. In: *Proceedings of the ASME 2012 IDETC/CIE*, Chicago, USA, pp 913–920, doi:[10.1115/DETC2012-71507](https://doi.org/10.1115/DETC2012-71507)

- Haftka RT (1990). Integrated structure-control optimization of space structures. *In: Dynamics Specialists Conference*, Long Beach, USA, pp 1–9, doi:[10.2514/6.1990-1190](https://doi.org/10.2514/6.1990-1190)
- Haftka RT, Gürdal Z (1992). *Elements of structural optimization*. Springer, Dordrecht, doi:[10.1007/978-94-011-2550-5](https://doi.org/10.1007/978-94-011-2550-5)
- Han JS (2012). Efficient frequency response and its direct sensitivity analyses for large-size finite element models using krylov subspace-based model order reduction. *Journal of Mechanical Science and Technology*, 26:1115–1126, doi:[10.1007/s12206-012-0227-8](https://doi.org/10.1007/s12206-012-0227-8)
- Hernandez V, Roman JE, Vidal V (2005). SLEPc: A scalable and flexible toolkit for the solution of eigenvalue problems. *ACM Trans. Math. Software*, 31(3):351–362, doi:[10.1145/1089014.1089019](https://doi.org/10.1145/1089014.1089019)
- Hoffarth M, Gerzen N, Pedersen CBW (2017). ALM overhang constraint in topology optimization for industrial applications. *In: Proceedings of the 12th world congress on structural and multidisciplinary optimisation*, Braunschweig, Germany, pp 1–11
- Hooijkamp EC, van Keulen F (2018). Topology optimization for linear thermo-mechanical transient problems: Modal reduction and adjoint sensitivities. *International Journal for Numerical Methods in Engineering*, 113(8):1230–1257, doi:[10.1002/nme.5635](https://doi.org/10.1002/nme.5635)
- Jensen JS, Pedersen NL (2006). On maximal eigenfrequency separation in two-material structures: The 1D and 2D scalar cases. *Journal of Sound and Vibration*, 289(4-5):967–986, doi:[10.1016/J.JSV.2005.03.028](https://doi.org/10.1016/J.JSV.2005.03.028)
- Jog CS (2002). Topology design of structures subjected to periodic loading. *Journal of Sound and Vibration*, 253(3):687–709, doi:[10.1006/jsvi.2001.4075](https://doi.org/10.1006/jsvi.2001.4075)
- Karimi A, Galdos G (2010). Fixed-order \mathcal{H}_∞ controller design for non-parametric models by convex optimization. *Automatica*, 46(8):1388–1394, doi:[10.1016/j.automatica.2010.05.019](https://doi.org/10.1016/j.automatica.2010.05.019)
- Kennedy CC, Pancu CDP (1947). Use of vectors in vibration measurement and analysis. *Journal of the Aeronautical Sciences*, 14(11):603–625, doi:[10.2514/8.1474](https://doi.org/10.2514/8.1474)
- Kennedy GJ, Hicken JE (2015). Improved constraint-aggregation methods. *Computer Methods in Applied Mechanics and Engineering*, 289:332–354, doi:[10.1016/j.cma.2015.02.017](https://doi.org/10.1016/j.cma.2015.02.017)
- Kim TS, Kim YY (2000). MAC-based mode-tracking in structural topology optimization. *Computers and Structures*, 74(3):375–383, doi:[10.1016/S0045-7949\(99\)00056-5](https://doi.org/10.1016/S0045-7949(99)00056-5)
- Kirsch U (2010). Reanalysis and sensitivity reanalysis by combined approximations. *Structural and Multidisciplinary Optimization*, 40(1):1–15, doi:[10.1007/s00158-009-0369-1](https://doi.org/10.1007/s00158-009-0369-1)
- de Klerk D, Rixen DJ, Voormeeren SN (2008). General framework for dynamic substructuring: History, review and classification of techniques. *AIAA Journal*, 46(5):1169–1181, doi:[10.2514/1.33274](https://doi.org/10.2514/1.33274)

- Koh HS, Kim JH, Yoon GH (2020). Efficient topology optimization of multicomponent structure using substructuring-based model order reduction method. *Computers & Structures*, 228:106146, doi:[10.1016/j.compstruc.2019.106146](https://doi.org/10.1016/j.compstruc.2019.106146)
- van der Kolk M, van der Veen GJ, de Vreugd J, Langelaar M (2017). Multi-material topology optimization of viscoelastically damped structures using a parametric level set method. *Journal of Vibration and Control*, 23(15):2430–2443, doi:[10.1177/1077546315617333](https://doi.org/10.1177/1077546315617333)
- Kreisselmeier G, Steinhauser R (1980). Systematic control design by optimizing a vector performance index. In: *Proceedings of the IFAC symposium*, Zürich, Switzerland, pp 113–117, doi:[10.1016/b978-0-08-024488-4.50022-x](https://doi.org/10.1016/b978-0-08-024488-4.50022-x)
- Langelaar M (2016). Topology optimization of 3D self-supporting structures for additive manufacturing. *Additive Manufacturing*, 12:60–70, doi:[10.1016/j.addma.2016.06.010](https://doi.org/10.1016/j.addma.2016.06.010)
- Langelaar M (2018a). Combined optimization of part topology, support structure layout and build orientation for additive manufacturing. *Structural and Multidisciplinary Optimization*, 57:1985–2004, doi:[10.1007/s00158-017-1877-z](https://doi.org/10.1007/s00158-017-1877-z)
- Langelaar M (2018b). Integrated component-support topology optimization for additive manufacturing with post-machining. *Rapid Prototyping Journal*, 25(2):255–265, doi:[10.1108/RPJ-12-2017-0246](https://doi.org/10.1108/RPJ-12-2017-0246)
- Langelaar M (2019). Topology optimization for multi-axis machining. *Computer Methods in Applied Mechanics and Engineering*, 351:226–252, doi:[10.1016/j.cma.2019.03.037](https://doi.org/10.1016/j.cma.2019.03.037)
- Laro D, Boots E, van Eijk J, Sanders L (2013). Design and control of a through wall 450 mm vacuum compatible wafer stage. In: *Proceedings of the 13th EUSPEN International Conference*, Berlin, Germany, pp 334–337
- Le C, Norato J, Bruns T, Ha C, Tortorelli D (2010). Stress-based topology optimization for continua. *Structural and Multidisciplinary Optimization*, 41:605–620, doi:[10.1007/s00158-009-0440-y](https://doi.org/10.1007/s00158-009-0440-y)
- Lee TH (1999). An adjoint variable method for structural design sensitivity analysis of a distinct eigenvalue problem. *KSME International Journal*, 13:470–476, doi:[10.1007/bf02947716](https://doi.org/10.1007/bf02947716)
- Lee TH (2007). Adjoint method for design sensitivity analysis of multiple eigenvalues and associated eigenvectors. *AIAA Journal*, 45(8):1998–2004, doi:[10.2514/1.25347](https://doi.org/10.2514/1.25347)
- Li Q, Chen W, Liu S, Tong L (2016). Structural topology optimization considering connectivity constraint. *Structural and Multidisciplinary Optimization*, 54:971–984, doi:[10.1007/s00158-016-1459-5](https://doi.org/10.1007/s00158-016-1459-5)
- Lin RM, Mottershead JE, Ng TY (2020). A state-of-the-art review on theory and engineering applications of eigenvalue and eigenvector derivatives. *Mechanical Systems and Signal Processing*, 138:106536, doi:[10.1016/j.ymssp.2019.106536](https://doi.org/10.1016/j.ymssp.2019.106536)

- Liu H, Zhang W, Gao T (2015). A comparative study of dynamic analysis methods for structural topology optimization under harmonic force excitations. *Structural and Multidisciplinary Optimization*, 51:1321–1333, doi:[10.1007/s00158-014-1218-4](https://doi.org/10.1007/s00158-014-1218-4)
- Liu J, Gaynor AT, Chen S, Kang Z, Suresh K, Takezawa A, Li L, Kato J, Tang J, Wang CCL, Cheng L, Liang X, To AC (2018). Current and future trends in topology optimization for additive manufacturing. *Structural and Multidisciplinary Optimization*, 57:2457–2483, doi:[10.1007/s00158-018-1994-3](https://doi.org/10.1007/s00158-018-1994-3)
- Lynch ME, Mordasky M, Cheng L, To A (2018). Design, testing, and mechanical behavior of additively manufactured casing with optimized lattice structure. *Additive Manufacturing*, 22:462–471, doi:[10.1016/j.addma.2018.05.021](https://doi.org/10.1016/j.addma.2018.05.021)
- Ma ZD, Kikuchi N, Hagiwara I (1993). Structural topology and shape optimization for a frequency response problem. *Computational Mechanics*, 13:157–174, doi:[10.1007/BF00370133](https://doi.org/10.1007/BF00370133)
- Ma ZD, Cheng HC, Kikuchi N (1994). Structural design for obtaining desired eigenfrequencies by using the topology and shape optimization method. *Computing Systems in Engineering*, 5(1):77–89, doi:[10.1016/0956-0521\(94\)90039-6](https://doi.org/10.1016/0956-0521(94)90039-6)
- Ma ZD, Kikuchi N, Cheng HC (1995). Topological design for vibrating structures. *Computer Methods in Applied Mechanics and Engineering*, 121:259–280, doi:[10.1016/0045-7825\(94\)00714-X](https://doi.org/10.1016/0045-7825(94)00714-X)
- Martinez VM, Edgar TF (2006). Control of lithography in semiconductor manufacturing. *IEEE Control Systems*, 26(6):46–55, doi:[10.1109/MCS.2006.252811](https://doi.org/10.1109/MCS.2006.252811)
- Miller CW (1978). *Determination of modal parameters from experimental frequency response data*. PhD thesis, University of Texas at Austin
- Miller DF, Shim J (1987). Gradient-based combined structural and control optimization. *Journal of Guidance, Control, and Dynamics*, 10(3):291–298, doi:[10.2514/3.20216](https://doi.org/10.2514/3.20216)
- Misiun G, van de Ven E, Langelaar M, Geijselaers H, van Keulen F, van den Boogaard T, Ayas C (2021). Topology optimization for additive manufacturing with distortion constraints. *Computer Methods in Applied Mechanics and Engineering*, 386:114095, doi:[10.1016/j.cma.2021.114095](https://doi.org/10.1016/j.cma.2021.114095)
- Molter A, Da Silveira OAA, Bottega V, Fonseca JSO (2013). Integrated topology optimization and optimal control for vibration suppression in structural design. *Structural and Multidisciplinary Optimization*, 47:389–397, doi:[10.1007/s00158-012-0829-x](https://doi.org/10.1007/s00158-012-0829-x)
- Munnig Schmidt R, Schitter G, van Eijk J (2011). *The design of high performance mechatronics*. Delft University Press, Delft
- Niu B, He X, Shan Y, Yang R (2018). On objective functions of minimizing the vibration response of continuum structures subjected to external harmonic excitation. *Structural and Multidisciplinary Optimization*, 57:2291–2307, doi:[10.1007/s00158-017-1859-1](https://doi.org/10.1007/s00158-017-1859-1)

- Olhoff N, Du J (2005). Topological design of continuum structures subjected to forced vibration. In: *Proceedings of 6th WCSMO*, Rio de Janeiro, Brazil
- Oomen T (2018). Advanced motion control for precision mechatronics: Control, identification, and learning of complex systems. *IEEE Journal of Industry Applications*, 7(2):127–140, doi:[10.1541/ieejia.7.127](https://doi.org/10.1541/ieejia.7.127)
- Ou JS, Kikuchi N (1996a). Integrated optimal structural and vibration control design. *Structural Optimization*, 12:209–216, doi:[10.1007/BF01197358](https://doi.org/10.1007/BF01197358)
- Ou JS, Kikuchi N (1996b). Optimal design of controlled structures. *Structural Optimization*, 11:19–28, doi:[10.1007/BF01279651](https://doi.org/10.1007/BF01279651)
- Paige CC, Saunders MA (1975). Solution of sparse indefinite systems of linear equations. *SIAM Journal on Numerical Analysis*, 12(4):617–629
- Papalambros PY, Wilde DJ (2000). *Principles of Optimal Design*. Cambridge University Press, doi:[10.1017/cbo9780511626418](https://doi.org/10.1017/cbo9780511626418)
- Pedersen NL (2000). Maximization of eigenvalues using topology optimization. *Structural and Multidisciplinary Optimization*, 20:2–11, doi:[10.1007/s001580050130](https://doi.org/10.1007/s001580050130)
- Pellens J, Lombaert G, Lazarov B, Schevenels M (2019). Combined length scale and overhang angle control in minimum compliance topology optimization for additive manufacturing. *Structural and Multidisciplinary Optimization*, 59:2005–2022, doi:[10.1007/s00158-018-2168-z](https://doi.org/10.1007/s00158-018-2168-z)
- Qian X (2017). Undercut and overhang angle control in topology optimization: A density gradient based integral approach. *International Journal for Numerical Methods in Engineering*, 111(3):247–272, doi:[10.1002/nme.5461](https://doi.org/10.1002/nme.5461)
- Rayleigh JWS (1945). *The theory of sound*, 1st American edn. Dover Publications, New York
- Ruhe A (1979). Implementation aspects of band lanczos algorithms for computation of eigenvalues of large sparse symmetric matrices. *Mathematics of Computation*, 33(146):680–687, doi:[10.2307/2006302](https://doi.org/10.2307/2006302)
- Saad Y (2003). *Iterative Methods for Sparse Linear Systems*, 2nd edn. SIAM
- Schwerdtfeger H (1979). *Geometry of Complex Numbers*. Dover Publications, New York
- Shu L, Wang MY, Fang Z, Ma Z, Wei P (2011). Level set based structural topology optimization for minimizing frequency response. *Journal of Sound and Vibration*, 330(24):5820–5834, doi:[10.1016/j.jsv.2011.07.026](https://doi.org/10.1016/j.jsv.2011.07.026)
- Sigmund O (2009). Manufacturing tolerant topology optimization. *Acta Mechanica Sinica*, 25:227–239, doi:[10.1007/s10409-009-0240-z](https://doi.org/10.1007/s10409-009-0240-z)
- Sigmund O, Maute K (2013). Topology optimization approaches: A comparative review. *Structural and Multidisciplinary Optimization*, 48:1031–1055, doi:[10.1007/s00158-013-0978-6](https://doi.org/10.1007/s00158-013-0978-6)

- Silva OM, Neves MM, Lenzi A (2020). On the use of active and reactive input power in topology optimization of one-material structures considering steady-state forced vibration problems. *Journal of Sound and Vibration*, 464:114989, doi:[10.1016/j.jsv.2019.114989](https://doi.org/10.1016/j.jsv.2019.114989)
- da Silveira OAA, Fonseca JSO (2010). Simultaneous design of structural topology and control for vibration reduction using piezoelectric. In: *Mecánica Computacional*, Buenos Aires, Argentina, pp 8375–8389
- Skogestad S, Postlethwaite I (2001). *Multivariable feedback control: analysis and design*, 2nd edn. John Wiley & Sons, New York
- van Solingen E, van Wingerden JW, Oomen T (2018). Frequency-domain optimization of fixed-structure controllers. *International Journal of Robust and Nonlinear Control*, 28(12):3784–3805, doi:[10.1002/rnc.3699](https://doi.org/10.1002/rnc.3699)
- Svanberg K (1987). The method of moving asymptotes - a new method for structural optimization. *International Journal for Numerical Methods in Engineering*, 24(2):359–373, doi:[10.1002/nme.1620240207](https://doi.org/10.1002/nme.1620240207)
- Tacx P, Oomen T (2021). Accurate \mathcal{H}_∞ -norm estimation via finite-frequency norms of local parametric models. In: *Proceedings of the American Control Conference*, New Orleans, USA, pp 322–327, doi:[10.23919/ACC50511.2021.9483366](https://doi.org/10.23919/ACC50511.2021.9483366)
- Torii AJ, de Faria JR (2017). Structural optimization considering smallest magnitude eigenvalues: a smooth approximation. *Journal of the Brazilian Society of Mechanical Sciences and Engineering*, 39:1745–1754, doi:[10.1007/s40430-016-0583-x](https://doi.org/10.1007/s40430-016-0583-x)
- Trillet D, Duysinx P, Fernández E (2021). Analytical relationships for imposing minimum length scale in the robust topology optimization formulation. *Structural and Multidisciplinary Optimization*, 64:2429–2448, doi:[10.1007/s00158-021-02998-w](https://doi.org/10.1007/s00158-021-02998-w)
- Tsai HC, Lin GC (1994). Explicit formulae for optimum absorber parameters for force-excited and viscously damped systems. *Journal of Sound and Vibration*, 176(5):585–596, doi:[10.1006/jsvi.1994.1400](https://doi.org/10.1006/jsvi.1994.1400)
- van der Veen G, Langelaar M, van Keulen F, van Keulen F (2015). Integrated topology and controller optimization of motion systems in the frequency domain. *Structural and Multidisciplinary Optimization*, 51:673–685, doi:[10.1007/s00158-014-1161-4](https://doi.org/10.1007/s00158-014-1161-4)
- van der Veen G, Langelaar M, van der Meulen S, Laro D, Aangenent W, van Keulen F (2017). Integrating topology optimization in precision motion system design for optimal closed-loop control performance. *Mechatronics*, 47:1–13, doi:[10.1016/j.mechatronics.2017.06.003](https://doi.org/10.1016/j.mechatronics.2017.06.003)
- van de Ven E, Ayas C, Langelaar M, Maas R, van Keulen F (2020a). Accessibility of support structures in topology optimization for additive manufacturing. *International Journal for Numerical Methods in Engineering*, 122:2038–2056, doi:[10.1002/nme.6611](https://doi.org/10.1002/nme.6611)

- van de Ven E, Maas R, Ayas C, Langelaar M, van Keulen F (2020b). Overhang control based on front propagation in 3D topology optimization for additive manufacturing. *Computer Methods in Applied Mechanics and Engineering*, 369:113169, doi:[10.1016/j.cma.2020.113169](https://doi.org/10.1016/j.cma.2020.113169)
- Venini P (2019). Topology optimization of dynamic systems under uncertain loads: An \mathcal{H}_∞ -norm-based approach. *Journal of Computational and Nonlinear Dynamics*, 14(2):021007, doi:[10.1115/1.4042140](https://doi.org/10.1115/1.4042140)
- Venini P, Pingaro M (2017). A new approach to optimization of viscoelastic beams: minimization of the input/output transfer function \mathcal{H}_∞ -norm. *Structural and Multidisciplinary Optimization*, 55:1559–1573, doi:[10.1007/s00158-016-1600-5](https://doi.org/10.1007/s00158-016-1600-5)
- Wang BP (1990). Improved approximate methods for computing eigenvector derivatives in structural dynamics. *AIAA Journal*, 29(6):1018–1020, doi:[10.2514/3.59945](https://doi.org/10.2514/3.59945)
- Wang F, Lazarov BS, Sigmund O (2011). On projection methods, convergence and robust formulations in topology optimization. *Structural and Multidisciplinary Optimization*, 43:767–784, doi:[10.1007/s00158-010-0602-y](https://doi.org/10.1007/s00158-010-0602-y)
- Xia Q, Zhou T, Wang MY, Shi T (2014). Shape and topology optimization for tailoring the ratio between two flexural eigenfrequencies of atomic force microscopy cantilever probe. *Frontiers of Mechanical Engineering*, 9:50–57, doi:[10.1007/s11465-014-0286-x](https://doi.org/10.1007/s11465-014-0286-x)
- Yang RJ, Chen CJ (1996). Stress-based topology optimization. *Structural Optimization*, 12:98–105, doi:[10.1007/BF01196941](https://doi.org/10.1007/BF01196941)
- Yoder S, Morgan S, Kinzy C, Barnes E, Kirka M, Paquit V, Nandwana P, Plotkowski A, Dehoff RR, Babu SS (2018). Characterization of topology optimized Ti-6Al-4V components using electron beam powder bed fusion. *Additive Manufacturing*, 19:184–196, doi:[10.1016/j.addma.2017.12.001](https://doi.org/10.1016/j.addma.2017.12.001)
- Yoon GH (2010). Structural topology optimization for frequency response problem using model reduction schemes. *Computer Methods in Applied Mechanics and Engineering*, 199(25-28):1744–1763, doi:[10.1016/j.cma.2010.02.002](https://doi.org/10.1016/j.cma.2010.02.002)
- Zargham S, Ward TA, Ramli R, Badruddin IA (2016). Topology optimization: a review for structural designs under vibration problems. *Structural and Multidisciplinary Optimization*, 53:1157–1177, doi:[10.1007/s00158-015-1370-5](https://doi.org/10.1007/s00158-015-1370-5)
- Zhou K, Doyle JC, Glover K (1996). *Robust and Optimal Control*. Prentice Hall
- Zhu J, Zhang W, Beckers P (2009). Integrated layout design of multi-component system. *International Journal for Numerical Methods in Engineering*, 78(6):631–651, doi:[10.1002/nme.2499](https://doi.org/10.1002/nme.2499)
- Zhu Y, Qiu J, Du H, Tani J (2002). Simultaneous optimal design of structural topology, actuator locations and control parameters for a plate structure. *Computational Mechanics*, 29:89–97, doi:[10.1007/s00466-002-0316-0](https://doi.org/10.1007/s00466-002-0316-0)

- Zhu Y, Qiu J, Du H, Tani J (2003). Simultaneous structural-control optimization of a coupled structural-acoustic enclosure. *Journal of Intelligent Material Systems and Structures*, 14(4-5):287–296, doi:[10.1177/1045389X03034685](https://doi.org/10.1177/1045389X03034685)

Acknowledgments

Getting this dissertation together has not been an easy task. After all, being in lockdown due to the COVID pandemic does not provide for much inspiration to write. Luckily many people have supported me in getting the job done, while making a lot of happy memories along the way.

First of all I would like to thank my promotors dr. ir. Matthijs Langelaar and prof. dr. ir. Fred van Keulen for our discussions and their critical feedback, which has been invaluable for the quality of the work. Also special thanks to prof. dr. ir. Martin van Gijzen and dr. Reinaldo Astudillo for advising and guiding me in the world of Krylov and Arnoldi algorithms.

Without the financial contributions of NWO and the consortium of companies, MI-Partners, Additive Industries, ASML, Nexperia, and Infinite Simulation Systems, this project would not have been possible. Their practical view, experience, and help have been a great asset to the project. Also the confirmation that this research is not purely of academic interest has been a big motivation for me.

Thankfully, ample time was left for coffee breaks with fellow colleagues at the university (and a few beers). In the beginning with Max van der Kolk, Sanne van den Boom, Dirk Munro, and Emiel van de Ven, who were always there to get me started with topology optimization and programming. A bit later Stijn Koppen joined at the opposing desk, with whom I have had discussions on countless topics at all times, both highly theoretical and complete nonsense. Also a lot of coffee and discussions were shared with Vibhas Mishra, Reinier Giele, and many others. Thanks should further go to Ran Xue, and Giannis Pappas, who have helped me in the project with various tasks, such as implementation of software interfaces and optimization algorithms. I would also like to thank all other colleagues of PME and the SOM group I have not mentioned for their input over the years.

Furthermore, I am grateful for all my friends, in particular the Protijgers, with whom I have experienced many fun moments, but also endured some difficult times. Also my family, who I thank for their unconditional support and their efforts in trying to keep up with my work. Finally, I could not have finished my PhD without Régie, for her love and support, especially during the lockdown days and whenever I felt like the PhD was never going to be finished. At the times when my mood was quite bad due to my code not working, thanks for helping me understand it would not be the end of the world and thanks for cheering me back up with coffee and snacks.

*Arnoud
The Hague, August 2022*

Curriculum Vitæ

Arnoud Delissen

5 Feb 1991	Born in Elsendorp, the Netherlands
2003 – 2009	High school VWO Commanderij college, Gemert
2009 – 2013	BSc Mechanical engineering Delft University of Technology
2009 – 2016	MSc Precision and microsystems engineering Delft University of Technology
May – Oct 2015	Visiting graduate researcher University of California, Los Angeles
2016 – 2017	Engineer Brabant Engineering, Best
2017 – 2022	PhD Integrated controller-topology optimization Delft University of Technology
2022 – current	Postdoc Giga-scale GPU topology optimization Delft University of Technology

List of Publications

Journal publications

5. **AATM Delissen**, G Radaelli, JL Herder (2017). Design and optimization of a general planar zero free length spring. *Mechanism and Machine Theory*, 117: 56–77, doi: [10.1016/j.mechmachtheory.2017.07.002](https://doi.org/10.1016/j.mechmachtheory.2017.07.002)
4. **AATM Delissen**, G Radaelli, LA Shaw, JB Hopkins, JL Herder (2017). Design of an Isotropic Metamaterial With Constant Stiffness and Zero Poisson's Ratio Over Large Deformations. *Journal of Mechanical Design*, 140(11): 111405, doi: [10.1115/1.4041170](https://doi.org/10.1115/1.4041170)
3. **AATM Delissen**, F van Keulen, M Langelaar (2020). Efficient limitation of resonant peaks by topology optimization including modal truncation augmentation. *Structural and Multidisciplinary Optimization*, 61: 2557–2575, doi: [10.1007/s00158-019-02471-9](https://doi.org/10.1007/s00158-019-02471-9)
2. **AATM Delissen**, E Boots, D Laro, H Kleijnen, F van Keulen, M Langelaar (2022). Realization and assessment of metal additive manufacturing and topology optimization for high-precision motion systems. *Additive Manufacturing*, 58: 103012, doi: [10.1016/j.addma.2022.103012](https://doi.org/10.1016/j.addma.2022.103012)
1. **AATM Delissen**, F van Keulen, M Langelaar (submitted). Integrated topology and controller optimization using the Nyquist curve. *Structural and Multidisciplinary Optimization*

Conference proceedings

2. **AATM Delissen**, D Laro, H Kleijnen, F van Keulen, M Langelaar (2020). High-precision motion system design by topology optimization considering additive manufacturing. *Proceedings of the 20th International Conference of the European Society for Precision Engineering and Nanotechnology, EUSPEN*, 20: 257–258
1. **AATM Delissen**, F van Keulen, M Langelaar (2022). Integrated controller-topology optimization for motion systems. *EUSPEN Special Interest Group: Precision Motion Systems & Control*